

Study for the Hull Shape of a Wave Energy Converter-Point Absorber

Design Optimization & Modeling Improvement

Filippos Kalofotias

A thesis presented for the degree of
Master of Science
Water Engineering & Management
University of Twente
The Netherlands
June 2016

UNIVERSITY OF TWENTE.



Graduation Committee:

Dr. Ir. J.S. Ribberink (chairman)

Dr. Ir. P.C. Roos

Dr. Ir. P.R. Wellens

Abstract

Global warming and the subsequent climate change have led governments to the pursuit of *clean* sources of energy. This kind of energy sources are the so-called *renewable energy* sources which are naturally replenished in human timescale. Wave energy, i.e. energy transported through sea masses via wind waves, can be a sustainable source of energy in the future. Wave energy can be harnessed by devices called *Wave Energy Converters*. Many types of *Wave Energy Converters* exist. *Point Absorbers* are one of these types and according to the author's opinion the most promising one. Nevertheless, wave energy conversion is still in *R&D* phase and far from being commercially applied as many challenges have to be overcome. In this context, the report studies the *Design Optimization* and *Modeling Improvement* of a *Point Absorber*.

In terms of *Design Optimization*, the *shape* and *dimensions* of the hull of the *Point Absorber* are considered. Three different shapes are evaluated, namely the Cylinder, the Bullet and the Cone. Each of the three shapes is dimensioned for deriving the highest *Efficiency* in power extraction. Specific restrictions regarding maximum dimensions of the hull were applied. The dimensioning of the three shapes is conducted by building a model deriving the average power extraction of each design in the Frequency Domain. Hydrodynamic input to the model is provided by a *Boundary Element Method* (BEM) model using *3D-Diffraction Theory*, namely NEMOH. Once dimensions for the three different shapes are derived, the three final designs are compared in terms of *Efficiency*. For the comparison, a model is built which derives the average power extraction of the *Point Absorber* in the Time Domain. NEMOH is used again for hydrodynamic input. Additionally, the *Computational Fluid Dynamics* (CFD) code, ComFLOW3 is employed for assessing the nonlinear effect of *viscous* damping. A CFD model and a methodology are produced for deriving drag coefficients for any studied design. The methodology makes use of the raw data derived by ComFLOW3 without adopting linear, non-viscous assumptions. Furthermore, an alternative approach for estimating the resulting, from viscous damping, drag force is presented and implemented in the Time Domain model. The Bullet design was selected as the most efficient. Results showed that the most efficient Bullet shape design proved to produce less viscous damping for fast oscillations where viscous damping is more important. Additionally, the Cylinder shape of the hull was found to produce much larger viscous damping than the other shapes and reasonably it should be avoided. In any case, it can be argued that the design optimization of the hull of the *Point Absorber* is a coupled problem in terms of shape and dimensions. Additional size restrictions can have significant influence and they can be a determinant factor.

Regarding *Modeling Improvement*, two additions are made to the Time Do-

main model as this was derived by Wellens (2004) and Kao (2014). Final Model 1 is derived for including viscous (drag) force more accurately. Drag force is estimated by adjusting the drag coefficient in a time-step manner. The adjustment is made by deriving the flow conditions at every time step using the dimensionless *Reynolds* and *Keulegan-Carpenter* numbers. A set of *Forced Oscillation Tests* is conducted for parameterizing the behavior of the drag coefficient in different flow regimes around the body. It was found that the inclusion of drag force in the Time Domain model can decrease the predicted extracted power significantly. Additionally, the inclusion of viscous damping shifts the position of the optimum configuration of the *Power Take Off* (PTO) device as this was derived by Wellens (2004). In general, it can be argued that viscous damping should be included both in the design optimization phase and in any control strategy applied such the one produced by Kao (2014). Then, Final Model 2 was produced so as to assess the influence of the changing position in the force exerted on the hull by waves, i.e. the excitation force. In both studies of Wellens (2004) and Kao (2014), the excitation force was estimated always at equilibrium position, i.e. the position at which the hull rests in calm water. The excitation force was divided to two components, namely the *Froude-Krylov* force and the *Diffraction*. The *Froude-Krylov* force is estimated by integrating the pressure around the hull without taking into account the wave/hull interaction. The *Diffraction* force is estimated by NEMOH runs in various positions and interpolation at every time step. The influence of the varying positions of the hull due was proved to be computationally expensive without adding significant information to the model. It was concluded that the assumption of estimating wave forces with the hull always at equilibrium position is valid at least for relatively large bodies. Finally, validation of the used models for estimation of forces provided good agreement with forces derived by CFD simulations.

Contents

Abstract	ii
1 Introduction	1
1.1 Background	1
1.1.1 Wave Energy	1
1.1.2 Point Absorber	2
1.2 Problem Definition	3
1.3 Research Objectives	4
1.4 Research Approach and Tools	5
1.4.1 Design Optimization	5
1.4.2 Modeling Improvement	6
1.4.3 Tools	8
1.5 Outline	9
2 Basic Theory and Models	10
2.1 Navier-Stokes Equations	11
2.2 Linear Wave Theory	12
2.3 Wave Energy	13
2.3.1 Energy Transfer under Regular Waves	14
2.3.2 Energy Transfer under Irregular Waves	14
2.4 Linear Mass-Spring-Damper System Model	16
2.5 Frequency Domain Model	19
2.5.1 Coefficient and Wave Force Determination	20
2.5.2 Frequency Characteristic Amplitude and Phase Shift	21
2.5.3 Power Extraction	22
2.6 Time Domain Model	23
2.6.1 Time Series	23
2.6.2 Hydrodynamic Coefficients and Retardation Function	24
2.6.3 Calculation of Response and Power Absorption	25
2.7 Boundary Element Method Model	26
2.8 Computational Fluid Dynamics Model	27
2.8.1 Computational Grid	28
2.8.2 Free Surface	28
2.8.3 Boundary Conditions	29
2.8.4 Turbulence Modeling	29
2.9 Overview and Comparison of the Models	30
2.9.1 Frequency vs Time Domain Model	30
2.9.2 BEM vs CFD Model	30

2.10 Dimensionless Parameters	31
3 Design Optimization	33
3.1 Dimensioning	33
3.1.1 Methodology	33
3.1.2 Results	35
3.2 Shape Evaluation	47
3.2.1 Methodology	47
3.2.2 Results	54
3.3 Summary	60
4 Modeling Improvement	61
4.1 Inclusion of Viscous Forces - Final Model 1	61
4.1.1 Methodology	61
4.1.2 Results	62
4.2 Inclusion of varying position of the buoy for wave force estimation - Final Model 2	66
4.2.1 Methodology	67
4.2.2 Results	67
4.3 Summary	69
5 Model Validation	70
5.1 Time Domain Model vs Frequency Domain Model	70
5.2 Final Model 1	72
5.3 Summary	74
6 Discussion	75
6.1 Methodology	75
6.2 Design Optimization	76
6.3 Modeling Improvement	80
7 Conclusions and Recommendations	83
7.1 Conclusions	83
7.2 Recommendations	86
8 Bibliography	87
Appendix A	90
Appendix B	93
Appendix C	95

Chapter 1

Introduction

This MSc thesis report is about the design and modeling of a *Wave Energy Converter-Point Absorber*. The research has been conducted by the author, upon completion of the MSc program of Water Engineering and Management of the University of Twente. The place of research was at Deltares Inc., Delft, the Netherlands and the time period extended between September, 2015 and May, 2016. Next, the *Background*, the *Problem Definition*, the *Research Objectives and Approach* and the *Outline* of the research are presented.

1.1 Background

1.1.1 Wave Energy

Wave energy is a form of renewable energy. Renewable energy is defined as energy collected by resources which are naturally replenished on a human timescale (Wikipedia, 2016a). Other examples of renewable energy are solar, tidal and wind energy. Wave energy is produced by the interaction of the wind and of the free surface of sea water masses. Energy by the wind is transferred to water through applied shear stress and it is transported in the direction of the generated wave. These wind generated waves are also called *short waves* in contrast to *long waves* such as tidal waves. Analogously, wave energy is referring to energy coming from *short waves* and not from tides. Consequently, it can be argued that wave energy and tidal energy are not only renewable but also endless.

Research, regarding the harnessing of wave energy, is not something new. The first official patent for wave energy conversion dates back in 1799, in Paris by Girard and his son (Wikipedia, 2016b). Later and in the next two centuries, hundreds of different patents were filed especially in the United Kingdom (U.K.). Increased interest in developing new technologies for wave energy conversion was usually linked with global energy crises such the oil crisis in 1978. In modern days, the establishment of the first marine energy test facility, namely *European Marine Energy Centre* (EMEC), in Orkney, Scotland, U.K., can be considered as a milestone. What seems to motivate the extended research for wave energy conversion in the present, is the worldwide pursuit for *cleaner* energy on behalf of the governments. The scenarios of a severe and eminent climatic change as a result of increased CO_2 emissions has led governments to adopting policies

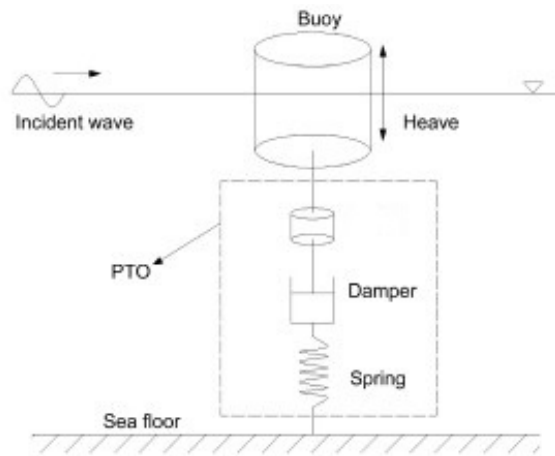


Figure 1.1: Basic Design of a *Point Absorber* (Cheng et al., 2014)

favoring renewable energy resources, also beyond the already widely applied ones such as solar and wind energy. Such a form of renewable energy is wave energy.

Harnessing of wave energy today is far from being commercially applied. One of the most serious challenges that wave energy conversion has to overcome is that wave energy can mainly be harnessed offshore which generally increases the cost of power transfer to the grid and maintenance. On the other hand, the huge potential that wave energy presents is a strong motive for continued research. As offshore harnessing is something almost unavoidable, researchers have to focus on studying and producing more efficient ways of energy extraction from waves. Wave energy extraction is achieved by the use of special devices called *Wave Energy Converters* (WEC). Optimization of WECs can lead to more affordable wave energy conversion in the future. This report focuses on the design optimization and modeling of an offshore WEC-*Point Absorber*. General information about WECs and their designs can be found in Appendix A.

1.1.2 Point Absorber

The basic design and functional principles of a *Point Absorber* are depicted in Fig.1.1. A rigid floating body (buoy) is attached to the sea bed via a cable or a pillar. A so-called Power Take Off device (PTO) is placed somewhere between the sea bed and the floater. Sometimes the PTO device is placed inside the hull of the floater. Its aim is to capture the wave-induced motion of the floater and through a mechanical generator (damper), to transform it to electrical power. Additionally, the PTO device carries a mechanical spring so as to hold the whole system in-line. It is obvious that the functional direction of the mechanical generator also determines the direction of the floater's motion which is crucial for power production. For *Point Absorbers*, this is the vertical motion of the floater, called *heave*.

According to the author's opinion, *Point Absorbers* have specific advantages comparing to other types of WECs. These advantages can be summarized as:

- *Point Absorbers* can absorb wave energy coming from all directions. Con-

sequently, they remain functional for the majority of the time unless extreme wave conditions occur.

- *Point Absorbers* have simple design, relatively small size and simple functional principles. As a result, they can be more cost effective in terms of manufacturing, installation and maintenance.

Nevertheless, as promising as the prospect of *Point Absorbers* might be, their technology and application are still in *R&D* phase. Efficient design, operation and reliable modeling are still a challenge for *Point Absorber* developers.

Research, regarding the optimization of a *Point Absorber*, involves mainly four topics:

1. *Design*, focusing mainly on the shape of the buoy, set-up issues like anchoring or PTO position, size of the buoy and of the PTO generator. Such studies have been conducted by Backer (2009) and Blanco et al. (2012).
2. *Modeling*, focusing mainly on deriving physically meaningful models for making reliable predictions of the power outcome of a *Point Absorber*, in accordance with its design and the wave climate. Such studies have been produced by Bhinder et al. (2011) and Thilleul (2013). Modeling is essential for the planning of a project and investment.
3. *Control Strategy*, focusing on the study of ways to maximize power extraction through forced resonance and mechanical control of the system. Relevant studies have been written by Falnes (1997) and Kao (2014).
4. *Power Extraction*, focusing mainly on studying the efficiency of different PTO devices, evaluating their performance and energy losses. Cargo (2012) has published a quite extensive research on PTO generators for wave energy conversion.

It should be noted here that these topics, as summarized here, are not independent. A *Point Absorber* is an integrated system and its optimization depends on the coordinated function of its components. This should be kept in mind during the research phase of each component and it is mentioned in every applying case in this report. Nevertheless, intention of the author is the presented results to be useful also to other researchers studying relevant topics.

1.2 Problem Definition

This research focuses on the topics of *Design* and *Modeling* in terms of a hydrodynamic assessment of the buoy's response and of the produced power. It is conducted in continuation to the studies conducted by Wellens (2004) and Kao (2014). Wellens (2004) studied the optimization of wave energy extraction under irregular wave conditions. He derived an optimum configuration for the mechanical parts (damper and spring) of the *Point Absorber* per sea state. Kao (2014) developed a control strategy for maximizing wave energy extraction by adjusting the configuration of the mechanical parts of the *Point Absorber* within discrete time intervals during a sea state. Both studies did not include in optimization and modeling of the *Point Absorber* the following topics:

Influence of shape and optimum dimensions of the buoy

Wellens (2004) and Kao (2014) studied only the case of a vertical cylinder. A different shape might produce better power extraction. Furthermore, they did not search for the optimum dimensions leading to maximum efficiency for power extraction with respect to the studied wave climate.

Influence of viscous effects to power extraction

Both studies modeled the dynamic response of the buoy to waves without taking into account viscous effects. During the oscillation of the buoy through the water surface, viscous effects will introduce extra damping to the buoy's motion.

Influence of varying position of the buoy for wave force estimation

Both studies assumed that the amplitude of the buoy's motion is relatively small and so the force induced by waves was always estimated at equilibrium position of the buoy, i.e. the position at which buoyancy equals gravity. This approach may introduce inaccurate power extraction predictions especially for large amplitude oscillations.

1.3 Research Objectives

Relevant to the *Problem Definition* presented in the previous section, the objectives of this study can be summarized as:

1. Derivation of an efficient design for the hull of the *Point Absorber's* buoy in terms of shape and dimensions and with respect to the studied wave climate.
2. Derivation of a simplified model for the *Point Absorber* including viscous forces and the influence of the dynamic response of the buoy to the wave force estimation.

The related research questions, to which this report attempts to give answers, are :

1. What is the most efficient design?
 - 1.1. How does the shape of the buoy influence power production efficiency?
 - 1.2. How do the dimensions of the buoy influence power production efficiency?
 - 1.3. In what way should different designs be evaluated so as the most efficient to be chosen?
2. How to improve the *Point Absorber's* modeling?
 - 2.1. How viscous effects can be estimated and included in the model?
 - 2.2. How wave force can be estimated more accurately and included in the model?
 - 2.3. What is the significance of the additions implemented to the model and how do they influence power production?

9.5	0	0	0	1	1	0	0	0
8.5	0	0	0	1	1	1	0	0
7.5	0	0	1	2	2	1	1	0
6.5	0	0	2	4	4	2	1	0
5.5	0	1	4	9	7	4	1	0
4.5	0	2	11	19	14	6	2	1
3.5	0	6	27	39	26	10	3	1
2.5	1	17	63	73	40	13	3	1
1.5	3	49	121	99	40	10	2	0
0.5	19	86	94	41	10	2	0	0
$H_s [m]$ / $T_z [s]$	3.5	4.5	5.5	6.5	7.5	8.5	9.5	10.5

Table 1.1: Scatter diagram of the sea states in the North Sea

1.4 Research Approach and Tools

The research is conducted under specific conditions both for the *Point Absorber* and the study area. The buoy of the *Point Absorber* is restricted to a single degree of freedom, in *heave* (displacement in z -direction), as this is the beneficial motion for wave energy conversion. Restrictions regarding the PTO generator have not been taken into account and potentially different control strategies have not been included in the design or the modeling phase. The presented assessment is site specific, referring to the *Netherlands Continental Shelf* (NCS). A water depth of $25m$ is considered as representative of the study area. Moreover, the wave climate is determined by the scatter diagram as this was derived by Global Wave Statistics (GWS) for the North Sea and it is presented in Table 1.1. H_s stands for the significant wave height, i.e. the average of the highest $1/3$ of the waves during a specific sea state. T_z stands for the zero up-crossing period of the waves, i.e. the average time that takes for the surface elevation to cross zero level by upward motion twice. Additionally, the frequency of occurrence of every sea state is given (white cells). The total sum of white cells is 1005. That means that the rate of occurrence of sea state with $H_s = 3.5m$ and $T_z = 6.5s$ is equal to $39/1005$. For the function of the *Point Absorber*, only sea states with significant wave height lower than or equal to $4.5m$ will be considered. These sea states represent the 95% of the annual wave climate. Sea states of higher significant wave height are considered as non-operational. Furthermore, design restrictions are applied so as to avoid over-dimensioning. The maximum radius of the *Point Absorber* is set to $10m$. Accordingly to the water depth considered, the maximum depth that the buoy can reach at equilibrium position is set to $15m$. The maximum total length, TD of $15m$ for the buoy of the *Point Absorber* guarantees that the buoy will not hit the sea bottom during large oscillations. Then, in accordance to the research objectives, the research approach is divided to two main topics: a) *Design Optimization* and b) *Modeling Improvement*.

1.4.1 Design Optimization

Three different shapes for the *Point Absorber's* buoy will be evaluated and they are shown in Figure 1.3. Hence these shapes will be named as: a) Cylinder (Cyl), b) Bullet (Bul) and c) Cone (Con). The geometrical description for the Cylinder,

the Bullet and the Cone is given in Figure 1.2. The *Design Optimization* consists of two parts: a) Dimensioning and b) Shape Evaluation. Then, the procedure for deriving the most efficient design can be described as:

a) Dimensioning

The procedure can be summarized as:

Creation of three different sets of designs

For every shape, a set of designs of different dimensions is created by varying the radius, R and the cylindrical length, CL .

Derivation of the most efficient design within each set

A Frequency Domain model is built so as to derive efficiency estimations for each design. Hydrodynamic input for the Frequency Domain model is produced by a *Boundary Element Method* (BEM) model using *3D-Diffraction Theory*. Then, the most efficient Cylinder, Bullet and Cone constitute the three final designs.

b) Shape Evaluation

The procedure can be summarized as:

Assessment of viscous effects for the three final designs

A *Computational Fluid Dynamics* (CFD) code is employed for creating a numerical tank. Each of the three final designs is forced to oscillate in otherwise calm water in the numerical tank. This procedure is the so-called *Forced Oscillation Test*. A method is developed for estimating viscous forces and deriving drag coefficients by *Forced Oscillation Tests*. The method calculates the total damping which is partly due to radiation of waves and partly due to viscous effects. Finally, it estimates the viscous part and derives the drag coefficients of the viscous (drag) force.

Derivation of an expression for viscous forces

A mathematical expression for the viscous force, also known as drag force, has to be derived for the case of an oscillating buoy in the presence of waves.

Comparison of the efficiency of the three final designs

A Time Domain model is developed for assessing the efficiency of the three final designs including the forces produced by viscous effects. The most efficient design is qualified.

1.4.2 Modeling Improvement

The *Modeling Improvement* study of the research is composed of two parts: a) The inclusion of viscous forces in a simplified model and b) The inclusion of the varying position of the buoy in the wave force estimation. Two models will be produced respectively, namely Final Model 1 and Final Model 2.

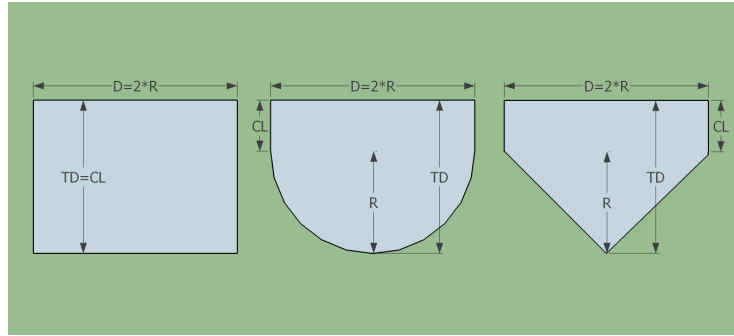


Figure 1.2: 2D sketch of the under water part of the studied geometries, where: CL = the length of the cylindrical part, D = the diameter of the cylinder, R = the radius of the cylinder and TD = the total draft of the buoy.

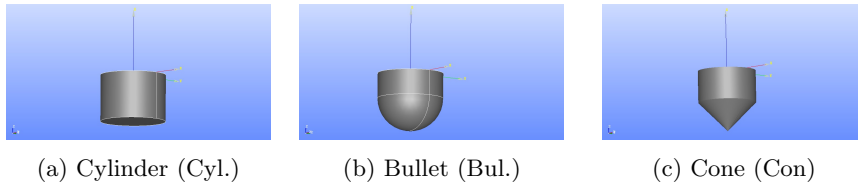


Figure 1.3: Design shapes for evaluation

a) Inclusion of Viscous Forces - Final Model 1

The procedure can be summarized as:

Forced Oscillation Test simulations for the final design

A number of different *Forced Oscillation Tests* will be conducted for the final design as this was derived by the *Design Optimization* part. A drag coefficient is derived by every simulation.

Drag coefficient parameterization

Based on the results derived by the *Forced Oscillation Tests*, the drag coefficient will be parameterized with the aid of the dimensionless *Reynolds* and *Keulegan-Carpenter* numbers.

Implementation of the parameterized drag coefficient in the model

The drag coefficients, as derived by the *Forced Oscillation Tests* and parameterization, will be implemented in the Time Domain model for assessing the drag force more accurately. Efficiency estimations in the presence of drag force are made and the influence of drag forces is derived.

b) Inclusion of varying position of the buoy for wave force estimation - Final Model 2

The procedure can be summarized as:

Analysis of the total wave force to components

The total wave force will be divided to two components: a) the *Froude-*

Krylov force and b) the *Diffraction* force. The *Froude-Krylov* force is derived by the integration of the hydrodynamic part of pressure under waves around the surface of the buoy. It is calculated as if the body does not interfere with waves. The *Diffraction* force is calculated by *3D-Diffraction Theory* and BEM code for assessing the force resulting by the interference between buoy and waves.

Froude-Krylov force

The Time Domain model will be adjusted for calculating the *Froude-Krylov* part of the wave force at every time step.

BEM simulations for estimating the *Diffraction* force

The *Diffraction* force is estimated by NEMOH simulations at various positions of the buoy. The final *Diffraction* force is calculated by interpolation.

Efficiency estimations

Finally, the model returns efficiency estimations, including the influence of varying position of the buoy. The influence of the wave force addition to the model is derived.

1.4.3 Tools

The tools used throughout the report are presented.

Frequency Domain model

Based on the mathematical description of the so-called *Linear Mass-Spring-Damper System*, the Frequency Domain model returns rather fast estimations of the efficiency in power extraction of a design in just a few seconds. The solution is derived in the frequency domain by superposition of the dynamic response of the buoy for every frequency component. It is rather useful when a large number of designs has to be assessed but it completely neglects viscous effects. The Frequency Domain model is built in MATLAB.

Time Domain model

The Time Domain is the time-dependent counterpart of the Frequency Domain model. The solution is derived in the time domain. The Time Domain is employed as it allows for the inclusion of nonlinear forces as long as these can be expressed mathematically in a time-dependent manner. In the absence of nonlinear forces the Time Domain model solution should match exactly the Frequency Domain solution. The Time Domain model is built in MATLAB.

Boundary Element Method and 3D-Diffraction Theory

The BEM code, NEMOH is employed for providing hydrodynamic input for the Frequency and Time Domain models. NEMOH is based on linear *3D-Diffraction Theory*. It completely neglects viscous effects as, for *3D-Diffraction Theory*, water is considered as an ideal fluid. Additionally, all the interactions between the buoy and surrounding water are assumed to be totally linear. As a result of the model's linearity, the time needed for every run does not exceed fifteen minutes.

Computational Fluid Dynamics

The CFD code, ComFLOW3 is used for assessing viscous effects produced during the oscillation of the buoy. ComFLOW3 returns a fully viscous solution of the *Navier-Stokes Equations*. No linear assumptions are adopted by ComFLOW3 regarding the interactions of the buoy with its surrounding water. The main drawback of this model is the rather large time (a few days) for a simulation of a few seconds.

1.5 Outline

The outline of this report is presented. In chapter 2, the *Basic Theory and Models* used are presented and explained. In chapter 3 the study for *Design Optimization* is presented both for methodology and derived results. In chapter 4 the study for *Modeling Improvement* is presented both for methodology and results. In chapter 5, *Validation* of the models used is provided. In chapter 6, further discussion on the derived results is made so as to assist to drawing final conclusions. Finally, in chapter 7 *Conclusions* regarding the research questions are drawn and *Recommendations* for further research are made.

Chapter 2

Basic Theory and Models

In this chapter the basic theory and the models used throughout the report are presented. Detailed derivation of mathematical formulas is beyond the scope of the report. Whenever it is considered useful, relevant literature is suggested. The topics which build the theoretical background can be summarized as:

Navier-Stokes Equations

The *Navier-Stokes Equations* (NSE) are considered to be the mathematical description of the dynamics of all fluid motions. NSE are the base for deriving the simplified equations of *Linear Wave Theory* as for NSE no analytical solution exists.

Linear Wave Theory

Linear Wave Theory (LWT) is a simplified description of the dynamics of fluid motion. It is quite useful as it allows for analytical solutions for the velocity and pressure field of fluid dynamics.

Wave Energy

It is important to quantify the energy transport under waves for assessing the power extraction of the *Point Absorber*. LWT allows for quantification of wave energy transport with analytical relations.

Linear Mass-Spring-Damper System

The *Linear Mass-Spring-Damper System* serves as the mathematical description of the dynamic response of the buoy of the *Point Absorber* both for the Frequency Domain and the Time Domain models.

Frequency Domain Model

The Frequency Domain model solves for the dynamic response of the buoy in the frequency domain. It is a fast model and valuable for deriving statistics for power extraction.

Time Domain Model

The Time Domain model solves for the dynamic response of the buoy in the time domain. It is valuable for including time-dependent nonlinear forces.

Boundary Element Method Model

Boundary Element Method (BEM) model is a linear model used for hydrodynamic input to the Frequency Domain and the Time Domain models.

Computational Fluid Dynamics Model

Computational Fluid Dynamics (CFD) model returns fully viscous numerical solution for the *Navier-Stokes Equations*. It assists in determining nonlinear effects for the wave/buoy interactions.

Dimensionless Parameters

Dimensionless parameters such as *Reynolds* (Re) and *Keulegan-Carpenter* numbers are used for the parameterization of the drag coefficients.

2.1 Navier-Stokes Equations

The *Navier-Stokes Equations* (NSE) are considered to fully describe the dynamics of fluid motion. For an incompressible fluid ($\frac{\partial \rho}{\partial t} = 0$), which is the case usually for water and by adopting the Eulerian approach (continuum hypothesis) the NSE are composed of:

Conservation of Mass

$$\vec{\nabla} \cdot \vec{u} = 0 \quad (2.1)$$

Conservation of Momentum

$$\frac{\partial \vec{u}}{\partial t} + (\vec{u} \cdot \vec{\nabla}) \vec{u} = -\frac{1}{\rho} \vec{\nabla} p + \nu \vec{\nabla}^2 \vec{u} + F_b \quad (2.2)$$

Where:

- \vec{u} = the water particles' velocity vector equal to (u, v, w) [m/s]
- u, v, w = the components of the velocity vector in $x-, y-, z-$ direction respectively [m/s]
- ρ = the water density [kg/m^3]
- p = the point pressure [N/m^2]
- ν = kinematic viscosity of water [m^2/s]
- F_b = the gravity vector equal to $(0, 0, -g)$ [m/s^2]
- g = the acceleration of gravity [m/s^2]

The *Conservation of Mass* equation for the incompressible case, determines that the mass and volume of the fluid remain constant. The *Conservation of Momentum* equation is simply the representation of Newton's 2nd law. The first term on the left hand side is the acceleration of water particles and comes directly from the Newton's 2nd law. The second term is the convective part of the NSE and represents the forces acting normally on the surface of the fluid element. On the right hand side, the first term represents the pressure forces acting on the fluid element, exerted by its surrounding fluid conditions. The second term is the diffusive part of the NSE and physically represents the shear forces acting on the fluid element. Finally the third term represents the external forces on the fluid element such as gravity. Solving for the velocity vector components and point pressure allows for detailed description of the

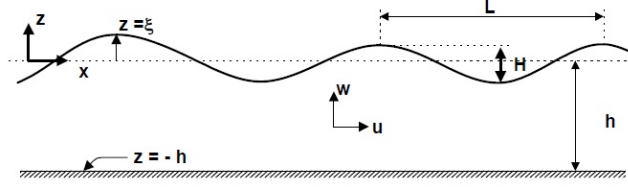


Figure 2.1: Sinusoidal wave form

dynamics of the fluid field. Unfortunately, up to date, no analytical solution of the full NSE has been derived. For that reason, a number of assumptions and appropriate boundary conditions need to be adopted so as an analytical solution to be derived. *Linear Wave Theory* (LWT) is such a case, widely applied and with significant practical application. For further information on the NSE the reader can refer to Kundu et al. (2012) and Anderson (1995).

2.2 Linear Wave Theory

Linear Wave Theory (LWT), also known as *Potential Theory*, is a simplified version of the NSE. According to LWT, the fluid is considered as ideal and the diffusive part of Eq. (2.2) is simply neglected. The reasoning for this assumption is that the kinematic viscosity of water is rather small ($\mathcal{O}10^{-6}$). Then, the water particles are assumed to be free of rotation (vorticity, $\Omega = \nabla \times \vec{u} = 0[s^{-1}]$) which allows for the introduction of the velocity potential, $\phi[m^2/s]$ according to:

$$\frac{\partial \phi}{\partial x} = u, \quad \frac{\partial \phi}{\partial y} = v, \quad \frac{\partial \phi}{\partial z} = w \quad (2.3)$$

Additionally, LWT allows only for sinusoidal wave solutions of the free surface. For any other shape of the free surface, LWT is not applicable. For a 2D case ($\frac{\partial}{\partial y} = 0$) in the xz -plane (Figure 2.1), the sinusoidal wave form reads:

$$\zeta(x, t) = \zeta_a \cdot \cos(kx - \omega t) \quad (2.4)$$

Where:

- $\zeta(x, t)$ = the free surface elevation with respect to $z = 0$ [m]
- ζ_a = the free surface elevation amplitude [m]
- k = the wave number [rad/m]
- ω = the free surface oscillation angular frequency [rad/s]

Then, another assumption for LWT to be valid, is that the wave height, $H = 2\zeta_a$ is much smaller compared to the wavelength L and water depth h . This assumption is needed for the linearization of the Bernoulli equation to be valid and for the gradients of the diffusive part of Eq.(2.2) to be small so as this part to be neglected. By substituting Eq. (2.3) into Eq. (2.1), (2.2) and by applying appropriate boundary conditions and assumptions, analytical solutions of the velocity components, pressure and the characteristic *dispersion relationship* are

derived. For the 2D case in the xz -plane and a given water depth h , the analytical formulas read:

$$u(x, z, t) = \frac{\partial \phi}{\partial x} = \omega \zeta_a \frac{\cosh k(h+z)}{\sinh kh} \cos(kx - \omega t) \quad (2.5)$$

$$w(x, z, t) = \frac{\partial \phi}{\partial z} = \omega \zeta_a \frac{\sinh k(h+z)}{\sinh kh} \sin(kx - \omega t) \quad (2.6)$$

$$p(x, z, t) = -\rho g z + \rho g \zeta_a \frac{\cosh k(h+z)}{\cosh kh} \cos(kx - \omega t) \quad (2.7)$$

$$\omega^2 = gk \tanh kh \quad (2.8)$$

Detailed derivation of the expressions of LWT can be found in chapter 5 of Journée and Massie (2001). Focus now shifts to discussing the limitations of LWT in wave applications.

The application limits of LWT originate from the adopted assumptions and they can be summarized as follows:

- LWT is valid only for relatively small waves compared to the wavelength and water depth. For wave energy conversion, waves with higher amplitudes are of major importance as they carry more energy.
- LWT is based on the consideration of water as an ideal fluid. For lower waves this is valid. For higher waves and in the presence of a moving body, vortices and flow separation may occur which are totally neglected by linear wave theory.
- In offshore environment, waves usually are not sinusoidal, and LWT can be inaccurate.

Nevertheless, LWT possesses certain, important advantages and this is why it is so widely applied in wave applications. These advantages can be summarized as:

- LWT is capable of providing results in rather short time.
- During the first phases of the designing of offshore structures, LWT can provide reliable rough estimations for comparing different designs.
- During calm wave conditions LWT is usually quite accurate.

2.3 Wave Energy

A wave, in general, is an oscillation accompanied by energy transfer through space or mass. For sea waves, the energy transfer oscillates the water particles and this is how wave energy is transmitted. For wave energy conversion, it is important to capture as much wave energy transfer as possible and turn it to electrical power. *Linear Wave Theory* (LWT) allows for quantifying the amount of energy transfer under sea waves. Two cases are identified. Energy transfer under regular (sinusoidal) waves and energy transfer under irregular waves as those observed in reality offshore. The basic energy and energy transfer relations are presented. Detailed derivation of these relations can be found in chapter 5 of Journée and Massie (2001).

2.3.1 Energy Transfer under Regular Waves

As regular waves, sinusoidal waves of the form of Eq. (2.4) are implied. Based on LWT, an expression for the total energy (kinetic and potential) per unit surface area inside the water column (from $-h$ to 0), averaged over one wave cycle is derived:

$$E_{tot} = E_k + E_p = \frac{1}{4}\rho g \zeta_a^2 + \frac{1}{4}\rho g \zeta_a^2 = \frac{1}{2}\rho g \zeta_a^2 = \frac{1}{8}\rho g H^2 \quad (2.9)$$

Where:

- E_{tot} = the total energy per unit wave surface area [J/m^2]
- E_k = the kinetic energy of the water particles per unit surface area [J/m^2]
- E_p = the potential energy of the water particles per unit surface area [J/m^2]

From the dispersion relation (Eq. 2.8), for any given wave frequency, ω and water depth, h , a wave number, k , is calculated which allows for calculating the wave propagation speed according to:

$$c = \frac{L}{T} = \frac{\omega}{k}, \quad L = \frac{2\pi}{k}, \quad T = \frac{2\pi}{\omega} \quad (2.10)$$

Where:

- c = the wave propagation speed [m/s]
- L = the wave length [m]
- T = the wave period [s]

This is the propagation speed of an individual wave. In general it is larger than the speed of energy propagation except in shallow water conditions. The energy, propagates with the so-called *group speed*, c_g given by:

$$c_g = c \cdot n \quad (2.11)$$

$$n = \frac{1}{2} \left(1 + \frac{2kh}{\cosh 2kh} \right) \quad (2.12)$$

Finally, the average energy transfer over one wave cycle per unit wave crest, hence called *Power*, is calculated by:

$$\bar{P}_w = E_{tot} \cdot c_g \quad (2.13)$$

Where:

- \bar{P}_w = the average energy transfer over one wave cycle per unit wave crest [$J/s/m$] or [W/m]

2.3.2 Energy Transfer under Irregular Waves

In reality, in open sea, all the frequencies exist and monochromatic waves of the form of Eq. (2.4) are almost never observed. The need for estimating the energy transfer during sea states composed of a number of wave frequencies led to the creation of the so-called *Wave Energy Spectra*. Offshore measurements of the surface elevation at a certain location were made. By applying a *Discrete Fourier Transformation* of the derived elevation signal, it is possible to match to every discrete frequency of the frequency range, a specific energy contribution

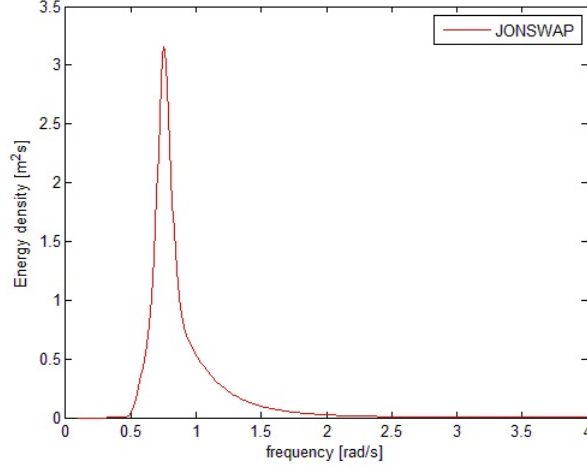


Figure 2.2: Wave Energy Spectrum (JONSWAP)

to the total energy. What is important, is to describe the statistical and not the instantaneous elevation or energy transfer properties of the sea state. Then by superposition principle, the total energy and average energy transfer can be calculated. LWT allows for this approach.

The statistical properties of the irregular sea state are described by the frequency-dependent energy density relation, $S_{\zeta}(\omega)$. Figure 2.2 depicts the energy density spectrum for a given sea state, $S_{\zeta}(\omega)$ (red line) plotted against the range of frequencies according to:

$$S_{\zeta}(\omega_n) \cdot \Delta\omega = \frac{1}{2}\zeta_{a_n}^2 \quad (2.14)$$

Where:

- $S_{\zeta}(\omega_n)$ = the energy density value corresponding to frequency ω_n [m^2s]
- $\Delta\omega$ = the frequency interval [rad/s]
- ζ_{a_n} = the wave amplitude corresponding to frequency ω_n for the respective energy contribution [m]

The total energy per unit surface area of the irregular sea state is the area under the red line in the graph multiplied by ρg .

$$E_{tot} = \rho \cdot g \int_0^{\infty} S_{\zeta}(\omega) d\omega \quad (2.15)$$

Where:

- E_{tot} = the average over one wave cycle energy per unit sea surface area [J/m^2]

The average power of the sea state is simply the superposition of the average power of every of the N frequency components:

$$\bar{P}_w = \sum_{n=1}^N E_{tot_n} \cdot c_{g_n} \quad (2.16)$$

Where:

$P_w =$ the average over one wave cycle energy transfer per unit wave crest
[W/m]

It should be noted that the chosen frequency resolution plays an important role in the previous calculations. A frequency resolution for which the total energy and power are not converging any more should be adopted. More information on wave energy spectra can be found in chapter 5 of Journée and Massie (2001).

A number of different *Wave Energy Spectra* has been used in offshore engineering practice. In this report the so-called JONSWAP spectrum is adopted. In 1967, the Joint North Sea Wave Project (JONSWAP) was launched in order to conduct extensive wave measurements in the North Sea. Six years after, Hasselmann et al. (1973) reported that the wave spectrum in the North Sea is never fully developed. It continues to develop through non-linear, wave-wave interactions even for very long times and distances. Since then, the derived JONSWAP spectrum is widely used and adopted as the characteristic wave energy spectrum for the North Sea but also for other fetch-limited seas around the world. The formula of the JONSWAP spectrum is given by:

$$S_{\zeta}(\omega) = 320 \frac{H_s^2}{T_p^4} \omega^{-5} \exp\left(\frac{-1950}{T_p^4} \omega^{-4}\right) \gamma^A \quad (2.17)$$

$$A = \exp\left(-\left(\frac{\omega}{\omega_p} - 1\right)^2\right) \quad (2.18)$$

Where:

$H_s =$ the significant wave height i.e. the average of the highest 1/3 of the wave height record [m]

$T_p =$ the peak period corresponding to the frequency ω_p with the highest energy density [s]

$\gamma =$ 3.3 (peakedness factor) [-]

$\sigma =$ a step function of ω : if $\omega \leq \omega_p$ then: $\sigma = 0.07$

a step function of ω : if $\omega > \omega_p$ then: $\sigma = 0.09$

$\omega_p =$ the peak frequency corresponding to the highest energy density value of the spectrum [rad/s]

In Figure 2.2, the JONSWAP energy spectrum for $H_s = 3.5m$ and $T_p = 8.3s$ is plotted.

2.4 Linear Mass-Spring-Damper System Model

In offshore and naval engineering, the response of a floating object to waves is important to be predicted by a model especially during the design phase. The most widely applied model for the description of motion of floating objects is the so-called *Mass-Spring-Damper System* (MSDS). The derivation of MSDS model is based on the analysis of the forces or moments acting on the floating object and on certain assumptions to be adopted.

A floating object has potentially six degrees of freedom in total, three translational and three rotational with respect to x -, y -, z -axis. For clarity, the

MSDS model will be derived for a single degree of freedom, namely *heave* (translational motion in z -direction) but it can be extended up to all six degrees of freedom. As for wave power extraction by a *Point Absorber* only *heave* is important, the motion of the floater will be restrained to an only up and down motion. The derivation starts with the analysis of forces (moments do not exist in restrained *heave* motion). The forces acting on the floating body can be described as:

Radiation Force, F_{rad}

Radiation force is exerted on the floating object as a result of its oscillatory motion through the water surface. This motion results in the creation of waves radiating from the buoy. The amount of energy of the radiated waves equals the amount of the energy loss (damping) of the floating object. As a consequence, a damping force is acting on the body, in z -direction for the *heave* case, opposing to the body's motion. This force is called the radiation force and hence in this report will be denoted as F_{rad} .

Added Mass Force, F_{add}

As the oscillatory motion of the buoy drives part of its volume in and out of the water mass, the water particles accelerate around its solid surface. As a result of this acceleration a net force is exerted on the buoy. This force is called the added mass force and hence in this report will be denoted as F_{add} .

Restoring Force, F_{res}

As the the buoy oscillates through the water surface according to Archimedes law it experiences also a buoyancy force proportionate to the water volume displaced by the buoy. As it can be expected this force is also oscillatory as the displaced volume increases or decreases relevant to the buoy's motion. This force tends to restore the buoy to its equilibrium position where buoyancy equals gravity. This is why it is called restoring force. Hence in this report the restoring force will be denoted as F_{res} .

Wave Excitation Force, F_{exc}

As waves approach the buoy, they create disturbance in the pressure field around the solid surface and pressure deviates from its hydrostatic state. According to *Linear Wave Theory* (LWT) and for undisturbed waves this disturbance is represented by the non-hydrostatic part (second term) of the right hand side of Eq. (2.7), presented in § 2.2. The hydrostatic part (first term) has already been accounted in the restoring force, F_{res} . The integration of the non-hydrostatic part of the pressure field leads to the so-called *Froude-Krylov* force. Additionally, as a result of the buoy's presence, the pressure field is disturbed. The result of this disturbance is the so-called *Diffraction* force. The sum of *Froude-Krylov* and *Diffraction* forces constitutes the excitation force, denoted by F_{exc} .

PTO Damping Force, F_{pto}

As shown in Figure 1.1, the buoy of the *Point Absorber* is connected to the damper of the PTO device so as to capture the wave induced motion and turn it to electrical power. This damper exerts a force on the buoy, counteracting its velocity, hence called in this report, F_{pto} .

Mechanical Spring Force, F_{spring}

As shown in Figure 1.1, a mechanical spring is also connected to the buoy and the PTO device so as to keep the whole system in-line. This mechanical spring exerts a force similar to the restoring force, F_{res} and hence it will be called F_{spring} .

Now that the forces acting on the floating body have been analyzed, certain assumptions have to be adopted in order to derive the MSDS model. The assumptions are mainly two:

1. *A linear interrelation between body's response, wave amplitude and induced forces is valid.* Doubling the wave amplitude, doubles the wave force and accordingly doubles the buoy's response and the forces connected to its motion.
2. *Superposition of forces and responses is valid.* This assumption allows for the superposition of the forces discussed previously and the superposition of responses derived by regular frequency components of an irregular sea state.

Then Newton's 2nd law is considered for a floating body restrained in heave motion only. According to it, the sum of the forces, F_{net} acting on the body equals its mass times its translational acceleration (moments are not discussed here but they obey the same principle):

$$F_{net} = m \cdot \ddot{z}_b = F_{exc} + F_{add} + F_{rad} + F_{res} + F_{spring} + F_{pto} \quad (2.19)$$

Where:

- F_{net} = the sum of the forces acting on the buoy [N]
- m = the mass of the buoy [kg]
- \ddot{z}_b = the net vertical acceleration of the buoy [m/s^2]

What is left now is to derive expressions for the force components F_{rad} , F_{add} , F_{res} , F_{spring} , F_{pto} and F_{exc} of the total force, F_{net} so as to be substituted in the left hand side of Eq. (2.19). The radiation force, F_{rad} as it was already stated, subtracts energy from the system. For that reason F_{rad} is behaving as a damper and so it is proportionate to the velocity of the floater according to:

$$F_{rad} = -b \cdot \dot{z}_b \quad (2.20)$$

Where:

- b = a radiation damping coefficient [kg/s]
- \dot{z}_b = the first time derivative of the vertical displacement of the buoy, i.e. the velocity [m/s]

The added mass force, F_{add} , as implied by its name, acts additionally to the buoy's absolute mass and so it is taken proportional to the acceleration of the floater according to:

$$F_{add} = -a \cdot \ddot{z}_b \quad (2.21)$$

Where:

- a = an added mass coefficient [kg]
- \ddot{z}_b = the second time derivative of the buoy's vertical displacement $z(t)$, i.e. the acceleration [m/s^2]

The restoring force, F_{res} according to Archimedes law of buoyancy, is taken proportional to the vertical displacement of the buoy according to:

$$F_{res} = -c \cdot z_b \quad (2.22)$$

Where:

$$\begin{aligned} c &= \text{a restoring coefficient [kg/s}^2\text{]} \\ z_b &= \text{the vertical displacement of the buoy [m]} \end{aligned}$$

Similarly to the restoring force, F_{res} and the radiation force, F_{rad} the mechanical spring force, F_{spring} and the PTO damping force, F_{pto} will be given by:

$$F_{spring} = -k_{sp} \cdot z_b \quad (2.23)$$

$$F_{pto} = -\beta \cdot \dot{z}_b \quad (2.24)$$

Where:

$$\begin{aligned} k_{sp} &= \text{a mechanical spring coefficient [kg/s}^2\text{]} \\ \beta &= \text{the PTO damping coefficient [kg/s]} \end{aligned}$$

Substituting Eqs. (2.20) - (2.24) in the left hand side of Eq. (2.19) and after some rearrangement, results into the MSDS model for a floating object in waves as:

$$\boxed{(m + a)\ddot{z}_b + (b + \beta)\dot{z}_b + (c + k_{sp})z_b = F_{exc}} \quad (2.25)$$

Eq. (2.25) can be solved for the displacement, $z(t)$ of the floating object either in the time domain or the frequency domain as a result of the superposition principle. For the solution derivation, it is needed that the three coefficients a, b and c are known along with the wave excitation force, F_{exc} . The linear MSDS model has been found to approximate well the response of any floating body as long as the response amplitude is relatively small (Journée and Massie, 2001). It neglects viscous drag exerted either by skin friction or by deformations of the velocity field of water around the moving object's surface. When the oscillation becomes larger, which is usually combined with increased response velocities, these viscous effects become more important and the MSDS model solutions deviate from what happens in reality.

2.5 Frequency Domain Model

As already mentioned, Eq. (2.25) can be solved for the floater's response in the frequency domain. Detailed derivations for the mathematical relations presented here can be found in chapter 6 of Journée and Massie (2001). The steps for deriving the frequency domain solution of Eq. (2.25) for a given sea state of known *Wave Energy Spectrum* can be summarized as:

1. Derivation of the coefficients and the excitation force appearing in Eq. (2.25)
2. Derivation of the frequency characteristic amplitudes and phase shifts
3. Calculation of the power absorption

2.5.1 Coefficient and Wave Force Determination

The frequency-dependent coefficients $a(\omega)$ and $b(\omega)$, in this thesis, are calculated using the *Boundary Element Method* (BEM) code NEMOH, developed by Ecole Centrale du Nantes (Ecole Centrale du Nantes, 2016). More information on NEMOH code can be found in § 2.7. For a given geometry the results for the two frequency dependent coefficients are presented in Figure 2.3 and 2.4. Next, based on Archimedes principle and the balance between weight and buoyancy, the restoring coefficient is calculated according to:

$$c = \rho g A_{wl} \quad (2.26)$$

Where:

A_{wl} = the cross-section of the buoy cut by the free surface water line [m^2]

These coefficients, as presented here, are valid only for the heave motion of the floating body. Additionally, the coefficients a , b and c depend uniquely on the specific geometry studied in every case. Next, attention is drawn to the determination of the mechanical spring, k_{sp} and PTO damping, β coefficients. These coefficients will be assumed adjustable and steady per sea state without adopting any specific control strategy, as applied by Kao (2014). Based on the study of Wellens (2004), for an irregular sea state of a given *Wave Energy Spectrum* the optimum values of k_{sp} and β are calculated as:

$$k_{sp} = \omega_p^2 [m + a(\omega_p)] - c \quad (2.27)$$

$$\beta = \sqrt{b(\omega_p)^2 + \frac{1}{\omega_p^2} (-(m + a(\omega_p))\omega_p^2 + c + k_{sp})^2} \quad (2.28)$$

The above equations when satisfied, guarantee the maximum energy absorption for the peak frequency, ω_p of a sea state for a specific geometry of the buoy. Different geometries will reach a different maximum power absorption for the same sea state, even if all of them satisfy the above equations. Finally, NEMOH also produces the frequency-dependent wave excitation force amplitude, $F_{exc,a}(\omega)$ per unit wave amplitude for the range of frequencies (Figure 2.5)

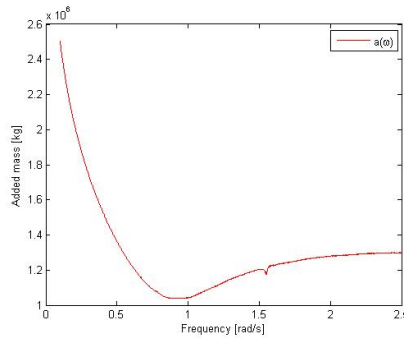


Figure 2.3: Added mass coefficient, $a(\omega)$

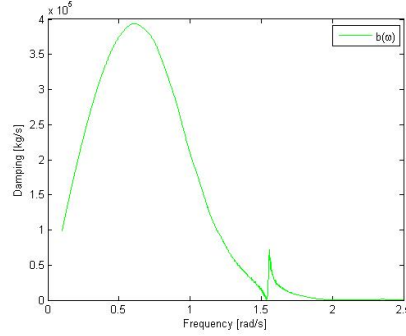


Figure 2.4: Damping coefficient, $b(\omega)$

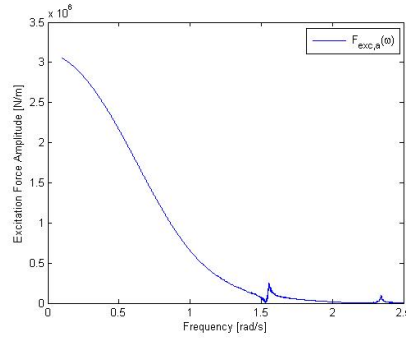


Figure 2.5: Excitation force amplitudes, $F_{exc,a}(\omega)$

2.5.2 Frequency Characteristic Amplitude and Phase Shift

The solution of the MSDS model in the frequency domain provides the frequency-dependent ratio of the floater's response over the incoming wave amplitude, hence in this report called *Response Amplitude Operator* (RAO) (Figure 2.6a). The mathematical description for the n -th frequency component of RAO reads:

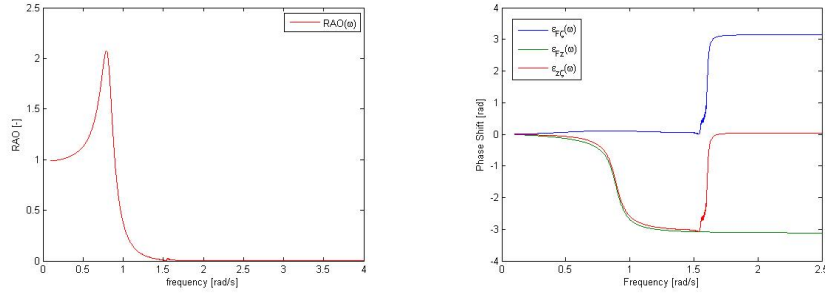
$$RAO = \frac{z_{b,a_n}(\omega_n)}{\zeta_{a_n}} = \frac{F_{exc,a_n}(\omega_n)}{\sqrt{[c + k_{sp} - [m + a(\omega_n)] \cdot \omega_n^2]^2 + [b(\omega_n) + \beta]^2 \omega_n^2}} \quad (2.29)$$

Equally important is the calculation of the frequency-dependent phase shifts between excitation force, response and incoming wave elevation (Fig.2.6b). These phase shifts will be used for building the solution of the MSDS model in the time domain. These phase shifts for the n -th frequency component read:

$$\epsilon_{F\zeta}(\omega_n) = \arctan\left(\frac{b(\omega_n) \cdot \omega_n}{c - a(\omega_n) \cdot \omega_n^2}\right) \quad (2.30)$$

$$\epsilon_{Fz}(\omega_n) = \arctan\left(\frac{-[b(\omega_n) + \beta] \cdot \omega_n}{c + k_{sp} - [m + a(\omega_n)] \cdot \omega_n^2}\right) \quad (2.31)$$

$$\epsilon_{z\zeta}(\omega_n) = \epsilon_{F\zeta}(\omega_n) - \epsilon_{Fz}(\omega_n) \quad (2.32)$$



(a) Response Amplitude Operator (RAO)

(b) Phase shifts

Figure 2.6: Frequency characteristic response amplitude and phase shifts

Where:

- $\epsilon_{F\zeta}(\omega)$ = the frequency-dependent phase shift between wave elevation and wave excitation force [rad]
- $\epsilon_{Fz}(\omega)$ = the frequency-dependent phase shift between response and wave excitation force [rad]
- $\epsilon_{z\zeta}(\omega)$ = the frequency-dependent phase shift between wave elevation and response [rad]

Combining Eq. (2.29) - (2.32) with Eq. (2.4) allows for deriving time-dependent equations for the n -th component of the excitation force, F_{exc} and the buoy's response, z_b as:

$$F_{exc}(t) = F_{exc,a_n}(\omega_n)\zeta_{a_n} \cos(k_n x - \omega_n t + \epsilon_{F\zeta}(\omega_n)) \quad (2.33)$$

$$z_b(t) = RAO(\omega_n)\zeta_{a_n} \cos(k_n x - \omega_n t + \epsilon_{z\zeta}(\omega_n)) \quad (2.34)$$

2.5.3 Power Extraction

For the average power absorption of a given geometry and sea state, use will be made of the derived relations of the previous sections. From physics, Power equals Force times Velocity. In our case, the force generating electrical power is the PTO damping force, F_{pto} . The needed velocity is simply the buoy's velocity, leading to the expression for the instantaneous power absorption:

$$P(t) = F_{pto} \cdot \dot{z}(t) \quad (2.35)$$

Integrating Eq. (2.35) over a wave cycle using Eq. (2.24) for the force, results in the expression for the average power absorption for a given geometry and sea state:

$$\bar{P} = \sum_{n=1}^N \frac{1}{2} \cdot \beta(\omega_n) \cdot \omega_n^2 \cdot RAO(\omega_n) \cdot \zeta_{a_n}^2 \quad (2.36)$$

The average extracted power, \bar{P} is simply the superposition of the average power of every of the N regular wave components of the irregular sea state. The number of the frequency components, N depends on the frequency grid resolution and the range of frequencies accounted.

2.6 Time Domain Model

Another possibility is to derive the buoy's response in the time domain as a time-dependent displacement. The most widely adopted time domain model is the Cummins equation model. For *Point Absorbers*, it is useful in case of the presence of an adjustable mechanical spring and an adjustable PTO damper as parts of an efficient control strategy under irregular sea states (Kao, 2014). Because of the adjustable spring and PTO damping coefficients the frequency domain approach cannot be used. Additionally, the Cummins Equation model allows for the inclusion in the model of non-linear effects as long as these can be expressed in a time-dependent manner.

The main idea behind the Cummins Equation (Cummins, 1962) is that a harmonic displacement, such as the wave induced heave motion of the buoy, occurring during a time interval Δt , influences the surrounding fluid not only during this interval but also for some time after. The system has a form of *memory*. Consequently, radiation force, F_{rad} and added mass force, F_{add} cannot then be calculated instantly but only by integrating over a certain time interval in the past. Note that the notation of hydrodynamic, PTO damping and mechanical spring coefficients changes to capital letters comparing to Eq. (2.25). This is done so as not to be confused with their frequency dependent counterparts. The Cummins equation for a heaving *Point Absorber* reads:

$$(M + A)\ddot{z}_b(t) + B_{PTO}\dot{z}_b(t) + \int_0^{\infty} B(\tau)\dot{z}_b(t - \tau)d\tau + (C + K)z_b(t) = F_{exc}(t) \quad (2.37)$$

Where:

- A = infinite added mass coefficient [kg]
- B = retardation function [kg/s]
- C = restoring coefficient [kg/s^2]
- B_{PTO} = PTO damping coefficient [kg/s]
- K = mechanical spring coefficient [kg/s^2]
- M = the solid mass [kg]
- $F_{exc}(t)$ = the time-dependent excitation force [N]
- $z_b(t)$ = time-dependent heave displacement [m]

The steps for deriving the power output of the *Point Absorber* by using Cummins Equation in the time domain, can be summarized as:

1. Generation of time series for the sea surface elevation, $\zeta(t)$ and the excitation force, $F_{exc}(t)$
2. Determination of the hydrodynamic coefficients and the retardation function
3. Numerical solution for the buoy's response and power absorption

2.6.1 Time Series

For every sea state, two time series have to be produced for excitation force and surface elevation. The time dependent sea surface elevation is derived by using

the amplitudes of the N regular components of the spectrum as in Eq. (2.14). The time-dependent sea surface elevation for a given sea state reads:

$$\zeta(t) = \sum_{n=1}^N \zeta_{a_n} \cdot \cos(\omega_n t + \epsilon_n) \quad (2.38)$$

Where:

$\epsilon_n =$ a random phase shift picked from a uniform distribution on $[0, 2\pi]$ [rad]

Next, by using the phase shift between wave force and wave elevation calculated in Eq. (2.30), the time-dependent excitation force reads:

$$F_{exc}(t) = \sum_{n=1}^N \left(\frac{F_{exc,a_n}}{\zeta_{a_n}} \right) \zeta_{a_n} \cos(\omega_n t + \epsilon_n + \epsilon_{F\zeta}) \quad (2.39)$$

The excitation force amplitude components in this study are calculated by NEMOH as also in the frequency domain model. The aim of the time domain solution is to regenerate the statistical properties of the frequency domain. The simulation time and subsequently the time series length should thus be long enough for that purpose. A consequence of building an irregular sea state by regular wave components is this. The produced wave signal will repeat itself after a period of $\frac{2\pi}{\Delta\omega}$ (Journée and Massie, 2001). So as to simulate a full sea state, this is the minimum amount of time of simulation.

2.6.2 Hydrodynamic Coefficients and Retardation Function

Ogilvie (1964), by using frequency dependent added mass, $a(\omega)$ and radiation damping, $b(\omega)$ coefficients such as the ones calculated by NEMOH, derived the following expressions:

$$B(t) = \frac{2}{\pi} \int_0^{\infty} b(\omega) \cos(\omega t) d\omega \quad (2.40)$$

$$A = a(\omega) + \frac{1}{\omega} \int_0^{\infty} B(\tau) \sin(\omega\tau) d\tau \quad (2.41)$$

$$C = c = \rho_w g A_{WL} \quad (2.42)$$

Retardation function, $B(t)$, (Eq. 2.40), also known as *Impulse Response Function* (IRF), is plotted against time in Figure 2.7. It denotes the significance of the past motions to the radiation force, F_{rad} estimation. Usually the duration of influence is of the order of some seconds, roundabout 10s in Figure 2.7 until $B(t)$ reaches almost zero. Eq. (2.41) is valid for every ω and so for $\omega = \infty$ resulting in:

$$A = \lim_{\omega \rightarrow \infty} a(\omega) \quad (2.43)$$

Added mass, A is therefore also called infinite added mass. Both, infinite added mass and IRF are computed using the BEM code NEMOH in this report.

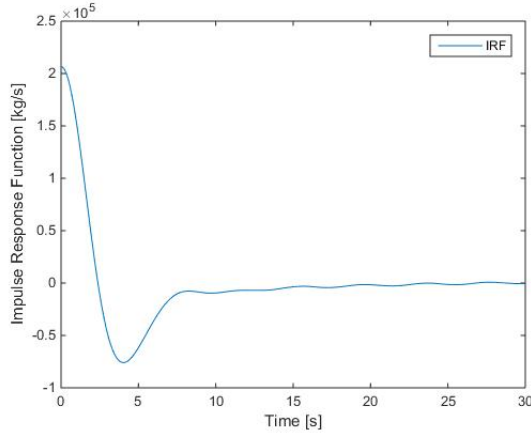


Figure 2.7: *Impulse Resonse Function (IRF), $B(t)$*

2.6.3 Calculation of Response and Power Absorption

Next, with known coefficients and wave load, $F_{exc}(t)$, Eq. (2.37) can be discretized in time, so as to derive a numerical solution of the time-dependent vertical displacement, $z_b(t)$ and velocity, $\dot{z}_b(t)$ of the buoy. Two initial conditions are needed, i.e. $\dot{z}_b(t_0)$ and $z_b(t_0)$. It is proposed that an advanced time discretization technique such as *Improved Euler* (Kao, 2014) or *Runge-Kutta* (Backer, 2009), is chosen. The final decision to be made, is the time interval for which the integro-differential, third term of Eq. (2.37) will be evaluated. This decision has to be made based on the produced IRF. For the IRF in Figure 2.7, it seems that a time interval of 30s is a safe choice for IRF to converge to zero.

As already mentioned in § 2.6, the Cummins Equation model allows for the inclusion of nonlinear forces as long as these can be determined in a time-dependent manner. This way a more realistic estimation for the buoy's response is possible. In this report two specific additions will be implemented. A velocity dependent drag force opposing to the buoy's motion is implemented. As already argued, on the contrary to *Linear Wave Theory* assumption, water does not behave as an ideal fluid. The drag force, F_{drag} addition will assess the influence of viscous effects on the predicted power absorption. The drag part of the, so-called, *Morison Equation* (Journée and Massie, 2001), for an oscillating cylinder in waves, is usually used in literature as a mathematical expression for the drag force which reads:

$$F_{drag}(t) = -\frac{1}{2}\rho C_d D \int_0^{L_b} |\dot{z}_b(t) - w(t)|(\dot{z}_b(t) - w(t)) ds \quad (2.44)$$

Where:

- C_d = a drag coefficient [-]
- w = the vertical water particles' velocity [m/s]
- D = the diameter of the cylinder [m]
- L_b = the vertical length of the cylinder [m]
- ds = the elementary vertical length of the cylinder [m]

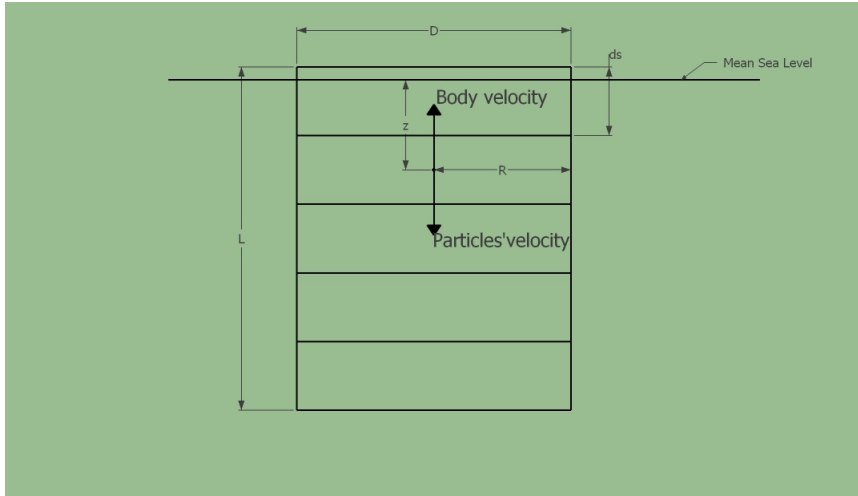


Figure 2.8: 2D cross-section of Cylinder divided into strips for drag force calculation

So as the above equation to return the total drag force, the vertical cross-section of the cylinder has to be divided in horizontal strips of known diameter and center. A representation of a Cylinder divided into strips is shown in Figure 2.8. The water particle's velocity, $w(t)$ is estimated at the center of each strip and the velocity of the body, $z(t)$ is found by the step by step solution of the Time Domain Model. Finally, integration of the drag forces calculated results to the total drag force, $F_{drag}(t)$. Furthermore, the drag coefficient, C_d has to be determined. The determination of a physically representative drag coefficient constitutes an important part of this research. More information about the application of the *Morison Equation* can be found in chapter 12 of Journée and Massie (2001). Another addition which can be added to the Time Domain Model is a time-dependent estimation of the excitation force, F_{exc} by taking into account the actual position of the buoy at every time step.

Finally, with the velocity of the buoy calculated by the numerical solution of the Cummins Equation and with known PTO damping coefficient, as calculated by Eq. (2.28), the instantaneous power output is given by Eq. (2.35). The average power output is simply calculated by:

$$\bar{P} = \frac{1}{T_{tot}} \sum_{t=0}^{T_{tot}} P(t) \cdot dt \quad (2.45)$$

Where:

T_{tot} = the total simulation time [s]

2.7 Boundary Element Method Model

The *Boundary Element Method* (BEM) model used throughout this report is NEMOH (Ecole Centrale du Nantes, 2016). NEMOH is the first open source

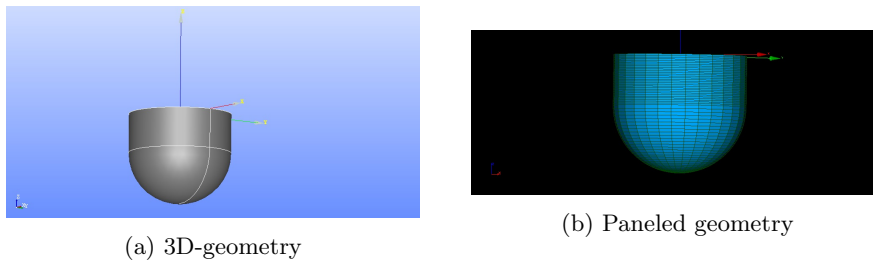


Figure 2.9: SALOME 7 design and paneled output for a random geometry

BEM code and it is available to users since January 2014. NEMOH is based on linear *3D-Diffraction Theory*. For detailed description of 3D-Diffraction theory, the reader can refer to chapter 7 of Journée and Massie (2001). In general, NEMOH, by taking advantage of *Linear Wave Theory* (LWT), solves two problems for every frequency of the chosen frequency grid: a radiation problem and a diffraction problem.

For the radiation problem, the 3D geometry is assumed to oscillate in still water. This way the frequency-dependent added mass and radiation damping coefficients per frequency of the geometry are derived. For the diffraction problem the, restrained, at equilibrium position, geometry is exposed to waves. Assuming linear diffraction as a result of wave/body interaction the diffracted wave field is produced and the wave excitation force amplitude per frequency is derived. What is important for NEMOH so as to produce these results is a 3D description of the coordinates of the geometry's surface.

For providing a detailed geometric description of the different geometries studied in this report, the 3D-CAD and meshing open source code SALOME 7 (SALOME, 2016) is used. SALOME 7 is only available for Linux operating systems. In Figure 2.9, the 3D design of a geometry and its meshed surface are shown. In Figure 2.9b, the surface of the geometry is divided into panels. The center of every panel has known coordinates which are used as input to NEMOH. For every panel, the radiation and diffraction problems are solved for the total range of discrete frequencies. Integration of the pressures calculated for every panel results to the estimation of coefficients and wave excitation force. This is why BEM is also called *panel method*. Finally it should be stated that the number of panels, as a result of pressure integration, should be large enough for better accuracy, regarding also the size of the geometry.

2.8 Computational Fluid Dynamics Model

The CFD code used throughout this report is ComFLOW3. It solves for u , v , w and p using the full Navier-Stokes Equations presented in Eq. (2.1), (2.2). Additionally, in the presence of a body, ComFLOW3 solves for the dynamic response of the body by calculating forces by pressure integration. A detailed description of the mathematical model of ComFLOW3 is beyond the scope of this report. For further information the reader can refer to (Wellens, 2012). Focus now, is turned to present the basic characteristics of ComFLOW3 as these are important in the model setup and results interpretation.

E	E	F	E	S	E	E	E	E
E	E	S	S	F	S	E	E	E
S	S	F	F	F	F	S	S	S
F	F	F	F	F	F	B	F	F
F	F	F	F	F	B	B	B	F

Figure 2.10: Cell labeling system in ComFLOW (Wellens, 2012). *E* for empty cells, *F* for fluid cells, *S* for free surface cells and *B* for body cells.

2.8.1 Computational Grid

ComFLOW3 is a finite volume CFD code, i.e. the computational domain is divided into control volumes of cell shape. For every volume the pressure is calculated at the center of the volume while at every cell face three velocity components are derived. ComFLOW3 uses a structured grid which remains steady but not necessarily uniform. Stretching of the cell size or coarsening of the grid at low interest territories of the domain is possible. ComFLOW3 is using a labeling system for the computational cells as depicted in Figure 2.10. For every time step, the cells are labeled as Fluid (F) Cells, Surface (S) Cells, Empty (E) Cells and Body (B) Cells. Whenever a body intersects a cell, the new apertures of the cell are computed and this is done for every time step.

2.8.2 Free Surface

In CFD wave simulations, the capture of the free surface (S-cells) is of major importance. In ComFLOW3, an improved *Volume of Fluid* (VOF) method is used, comparing to the original as this was derived by Hirt and Nichols (1981). The two VOF approaches are shown in Figure 2.11. The original method (Figure 2.11a) calculates the water fill ratio of the total cell volume based on the net mass flux through the faces of every cell. This way, there is the probability of total water volume loss or gain as a result of over-draining or over-filling cells. With the improved VOF method used in ComFLOW3, the free surface is reconstructed by using the gradient of adjacent S-cells calculated by a height function as depicted in Figure 2.11b.

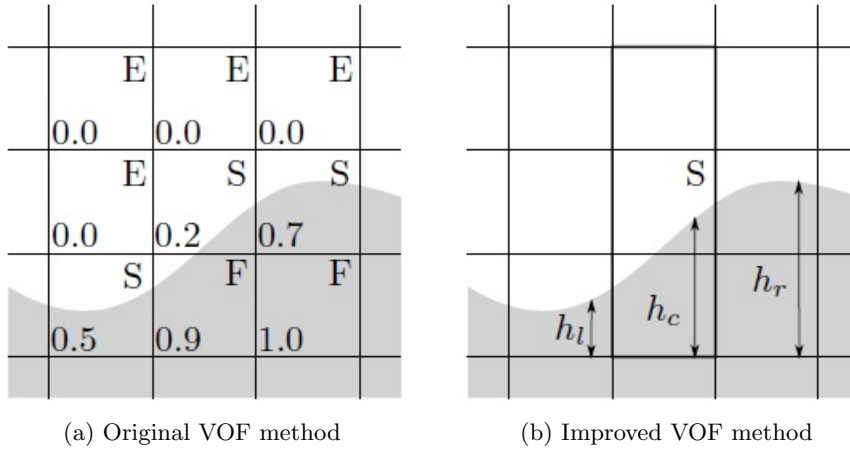


Figure 2.11: Original and improved *Volume of Fluid* methods (Wellens, 2012)

2.8.3 Boundary Conditions

At first, the impermeability of the bottom of the domain is reassured by imposing $\vec{u} \cdot \vec{n} = 0$, where \vec{n} is the unit vector perpendicular to the bottom. At the free surface, the pressure is imposed as $p = p_0$. As the position of the free surface deviates from the position of the cell center where pressure is calculated by the code, the pressure for S-cells is calculated by interpolation relatively to the position of the free surface. The boundary conditions at the lateral sides of the computational domain can be open or closed. Open boundary conditions which allow for both energy dissipation and flow through the boundaries are rather valuable in wave simulations. In ComFLOW3, this kind of boundaries is implemented as *Generating Absorbing Boundary Conditions* (GABC). The goal of GABC is to return as little wave reflection from the boundaries as possible without the need for using large domains or a numerical beach for wave energy dissipation. Simultaneously, GABC allow for wave generation at the boundaries. GABC are set according to the range of frequencies for which wave energy dissipation should be optimum. The setup involves the determination of three coefficients, namely a_0 , a_1 and b_1 . ComFLOW3 is equipped with a MATLAB function which for a given range of frequencies returns the optimum combination of these coefficients. In case that only one wave frequency exists in the computational domain, then a_1 and b_1 can be set to zero and a_0 is given by:

$$a_0 = \sqrt{\frac{\tanh kh}{kh}} \quad (2.46)$$

The latter configuration corresponds to the so-called *Sommerfeld* boundary conditions. Detailed mathematical derivation and presentation of the ComFLOW3 boundary conditions are given in chapter 6 of Wellens (2012).

2.8.4 Turbulence Modeling

The turbulence modeling is an important part in every CFD simulation. The need for turbulence modeling arises from the fact that turbulent phenomena in

wave simulations occur in a range of scales from rather small (a few mm) to rather large (meters). For the small scale turbulent phenomena to be captured by direct solution of the NSE, the grid size resolution has to decrease that much that only super computers can return results in a sensible amount of time. For that reason in all CFD codes, extra equation(s) of the water particles' kinetic energy are introduced so as to model turbulence in scales smaller than the grid size resolution. ComFLOW3 uses a *Large Eddy Simulation* (LES) turbulence model. With LES model, the turbulence in large scales is predicted by direct numerical solution of the NSE and only in small scale the LES equations predict the turbulence kinetic energy. For more information on the various turbulence models and specifically on the LES model, the reader can refer to Nichols (2001).

2.9 Overview and Comparison of the Models

Four models were presented in the previous sections, namely:

- Frequency Domain Model
- Time Domain Model
- BEM Model
- CFD Model

The first two are used for deriving the power prediction outcomes. The latter two are used for providing input for the first two. An overview and comparison between Frequency and Time Domain models and BEM and CFD models is presented.

2.9.1 Frequency vs Time Domain Model

The Frequency and the Time Domain models are quite similar. The Time Domain model, without including any non-linear terms, is just a time-dependent representation of the Frequency Domain model. Both models are depending on BEM input and so the linear wave/body interaction is restricting for both models. The main advantage of the Time Domain model is the possibility for including nonlinear effects such as viscous damping and adjustable spring and PTO damping coefficients. This way, part of the BEM and LWT physical restrictions can be tackled. The advantage of Frequency Domain model is that it is computationally cheap. A Frequency Domain simulation takes a few seconds so as to be made. As for the Time Domain model to provide representative results, long time series are needed and so the simulation time is longer. A typical Time domain simulation of 6000-9000 seconds takes about two to three minutes. If a large number of designs needs to be tested the difference is significant. A comparison overview is provided in Table 2.1.

2.9.2 BEM vs CFD Model

BEM and CFD models are tools that assist in the modeling of *Point Absorbers*. Every output of the BEM code can be reproduced by CFD simulations. The difference in the output between the two models will be derived by the fact

Model	Viscous Effects	Wave-Body Interaction	Accuracy	Simulation Time
Frequency Domain	No	Linear radiation and diffraction (BEM)	Better for calm sea states- Questionable around resonance	A few seconds
Time Domain	Can be included	Linear radiation and diffraction (BEM)	Better accuracy when nonlinearities are estimated- Validation needed	A few minutes

Table 2.1: Frequency vs Time domain model

Model	Viscous Effects	Wave-Body Interaction	Simulation Time
BEM	No	Linear radiation and diffraction (BEM)	A few minutes
CFD	Fully viscous solution	Fully non-linear	A few days

Table 2.2: BEM vs CFD model

that CFD produces a fully viscous solution. On the contrary, BEM considers water as an ideal fluid. For calm sea states, LWT and BEM have proven to work quite accurately. The problem for predicting wave energy extraction, is that higher sea states are of major interest as they carry more energy. In these conditions power prediction based solely on BEM input has doubtful accuracy. On the other hand, using CFD model extensively is quite difficult because of the large time needed for a simulation. A BEM simulation with rather fine frequency resolution does not last more than fifteen minutes. Some of the CFD simulations presented in this report lasted more than a week. So a combination of the two models is needed. A comparison overview is provided in Table 2.2.

2.10 Dimensionless Parameters

In offshore engineering, the use of dimensionless quantities for parameterizing the numerous different conditions of wave/body interactions is common. Throughout this report the following dimensionless quantities are used:

Keulegan-Carpenter Number (KC)

The KC number describes the relative importance of the drag forces over the inertia forces in an oscillatory flow around a still or a floating body. For large KC numbers the drag forces are dominant while for small KC numbers the inertia forces are dominant. The KC number can be calculated according to:

$$KC = \frac{V_m \cdot T}{D} \quad (2.47)$$

Where V_m is the maximum velocity of the oscillation, T is the period of oscillation and D is a characteristic length of the structure, in our case will be the diameter of the buoy.

Reynolds Number (Re)

The Re number describes the relative importance of inertia forces to viscous forces. For low Re the viscous forces are dominant and the fluid motion is smooth and constant. For high Re , the inertia forces are dominant and eddies, vortices and flow instabilities occur. The Re number is calculated according to:

$$Re = \frac{V_m \cdot D}{\nu} \quad (2.48)$$

Where V_m is the maximum velocity of the oscillation, D is a characteristic length of the structure, the diameter in our case and ν is the kinematic viscosity of water.

Chapter 3

Design Optimization

3.1 Dimensioning

The methodology for estimating the optimum dimensions of the three shapes, namely the Cylinder, the Bullet and the Cone, is presented. The criterion of *Efficiency*, based on which the different designs are evaluated, is introduced. Finally, the results of the proposed methodology are given with comments whenever this is considered important.

3.1.1 Methodology

For deriving the optimum dimensions for every design, these designs is needed to be geometrically described. The geometrical description for the Cylinder, the Bullet and the Cone is given in Figure 1.2. The Bullet and the Cone are composed of an upper cylindrical part. The length of this cylindrical part is denoted by CL . The Bullet has a hemispherical lower part while the Cone has a conical lower part pointing downwards. The hemisphere's radius, the cone's upper radius and the cone's height are equal to the cylinder's radius, R . The total length (draft) of every design is denoted by TD . For the Cylinder the total length, TD coincides with the cylinder length, CL .

Based on the previous geometrical description, for every shape, three sets of designs of variable dimensions are produced. Every set of designs is produced by varying the radius, R and the cylinder length, CL . As already mentioned in § 1.2, the maximum radius, R should not exceed $10m$ and the total length, TD should not exceed $15m$. Taking these restrictions into account the sets of designs to be tested are presented in Tables 3.1, 3.2 and 3.3. A code and a number are assigned to every different design, namely *Bul*, *Con*, *Cyl* for the Bullet, the Cone and the Cylinder respectively plus an assigned number.

$R[m]$ \ $CL[m]$	5	7.5	10
5	Bul1	Bul2	Bul3
7.5	Bul4	Bul5	
10	Bul6		

Table 3.1: Bullet set of designs to be tested

$R[m]$ \ $CL[m]$	5	7.5	10
5	Con1	Con2	Con3
7.5	Con4	Con5	
10	Con6		

Table 3.2: Cone set of designs to be tested

$R[m]$ \ $CL[m]$	5	10	15
5	Cyl1	Cyl2	Con3
7.5	Cyl4	Cyl5	Cyl6
10	Con7	Cyl8	Cyl9

Table 3.3: Cylinder set of designs to be tested

As it can be noticed in Table 3.1 and 3.2, some combinations of radius, R and cylinder length, CL are excluded. The reason for this exclusion is that as mentioned in § 1.2 the total length, TD of the buoy cannot exceed 15m. For the Bullet and Cone cases, the total draft is calculated as: $R + CL = TD$. For the excluded combinations the total draft, TD exceeds 15m.

Next, attention is drawn to the criteria of the design evaluation. Designs of different radii need to be compared. As explained in § 2.3.2, the wave energy transfer (power) occurs in the direction of wave propagation and it is calculated per meter wave crest. It is reasonable then, that buoys of larger radii will have access to larger amounts of wave energy. This way it would be always right to pursue for the larger radius in several designs. On the other hand, overdimensioning the buoy will unavoidably increase its mass. Increase in mass can subsequently lead to increasing the buoy's inertia forces and eventually decreasing buoy's velocity and absorbed wave energy. This way, a larger design although it absorbs more wave energy, compared to a smaller one, it is not as efficient as the smaller one because it absorbs smaller proportion of the available wave energy. For that reason, the dimensionless quantity of *Efficiency* is used as evaluation criterion for comparing different designs in this report. *Efficiency* stands for the ratio of the average absorbed wave energy by the buoy, as calculated by Eq. (2.36) (2.45), over the average available power per sea state. The latter is calculated by multiplying Eq. (2.16) with the diameter of the buoy.

The dimensionless *Efficiency* (Eff) is then calculated by:

$$Eff = \frac{\bar{P}}{\bar{P}_w D} = \frac{\bar{P}}{\bar{P}_{avail}} \quad (3.1)$$

Where:

\bar{P}_{avail} = the average available wave power over one wave cycle [W]

With the different designs and the evaluation criterion specified, it is left for a methodology, allowing for *Efficiency* calculations, to be defined. At this phase of design dimensioning, a large number of designs needs to be evaluated. For that reason a fast model providing rough estimations of the *Efficiency* of every design will be chosen for comparisons to be made. The Frequency Domain Model (see § 2.5) aided by NEMOH model (see § 2.7) can return rather fast estimations of the designs' *Efficiency*. The average absorbed power, \bar{P} and the average available power, \bar{P}_{avail} will be estimated for the whole scatter diagram as this was presented in § 1.2. For every design, a NEMOH simulation, with a rather fine frequency resolution, did not last more than fifteen minutes with the capacity of running multiple simulations simultaneously. Once the input by NEMOH is derived it is a matter of a few seconds for the Frequency Domain Model to return *Efficiency* estimations for every tested design. Finally, from every of the three set of designs (Bul, Cyl, Con) the most efficient is chosen.

3.1.2 Results

The Frequency Domain model and BEM code, NEMOH are employed for comparing the various designs presented in Table 3.1, 3.2 and 3.3. The frequency range was set to $0.1-4.0rad/s$. The frequency interval, $\Delta\omega$ was set to $0.001rad/s$. The frequency interval was chosen based on the validation of the Time Domain model (see chapter 5). Results are presented.

Total Average Available Power, \bar{P}_{avail} [kW]

The total average available power, \bar{P}_{avail} is proportional to the design radius, R and it is derived by assessing all the sea states of the scatter diagram. For the three different radii of the evaluated designs, it is presented in Table 3.4.

$R[m]$	5	7.5	10
$\bar{P}_{avail}[kW]$	202.15	303.23	404.31

Table 3.4: Total average available power, \bar{P}_{avail} per design radius [kW].

Comments

- The total average available power, \bar{P}_{avail} is linearly proportional to the design's radius, R as it was expected.

Total Average Power Extraction, \bar{P} [kW]

The total average power extraction, \bar{P} , assessed for all the sea states, for every design of the Cylinder, the Bullet and the Cone sets is given in Table 3.5, 3.6 and 3.7.

Cylinder				
		$CL[m]$		
$R[m]$		5	10	15
5		46.7	48.3	59.9
7.5		85.5	87.1	90.0
10		124.8	127.5	122.3

Table 3.5: Total average power extraction, \bar{P} results for Cylinder designs [kW]. In green color the design with the highest power extraction.

Bullet				
		$CL[m]$		
$R[m]$		5	7.5	10
5		46.5	47.5	51.8
7.5		85.4	88.2	
10		125.9		

Table 3.6: Total average power extraction, \bar{P} results for Bullet designs [kW]. In green color the design with the highest power extraction.

Cone				
		$CL[m]$		
$R[m]$		5	7.5	10
5		45.5	47.7	48.0
7.5		84.5	84.9	
10		124.1		

Table 3.7: Total average power extraction, \bar{P} results for Cone designs [kW]. In green color the design with the highest power extraction.

Comments

- Cyl8, Bul6 and Con6 are the three designs from every set with the highest total average power extraction, \bar{P} .
- Cyl9, Bul6 and Con6 have the same radius, R .

Total Average Efficiency, Eff [-]

The total average *Efficiency*, (Eff) results for the various designs of the Cylinder, the Bullet and the Cone are presented in Table 3.8, 3.9 and 3.10.

Cylinder				
		$CL[m]$		
$R[m]$		5	10	15
5		0.23	0.24	0.30
7.5		0.28	0.29	0.30
10		0.31	0.32	0.30

Table 3.8: Average *Efficiency* results for Cylinder designs. In green color the design with the highest *Efficiency*

Bullet				
$R[m]$ \ $CL[m]$	5	7.5	10	
5	0.23	0.24	0.26	
7.5	0.28	0.29		
10	0.31			

Table 3.9: Average *Efficiency* results for Bullet designs. In green color the design with the highest *Efficiency*

Cone				
$R[m]$ \ $CL[m]$	5	7.5	10	
5	0.23	0.24	0.24	
7.5	0.28	0.28		
10	0.31			

Table 3.10: Average *Efficiency* results for Cone designs. In green color the design with the highest *Efficiency*

Comments

- Cyl8, Bul6 and Con6 have the highest *Efficiency* among the three sets of designs.
- Cyl8, Bul6 and Con6 are depicted with dimensions in Figure 3.1.

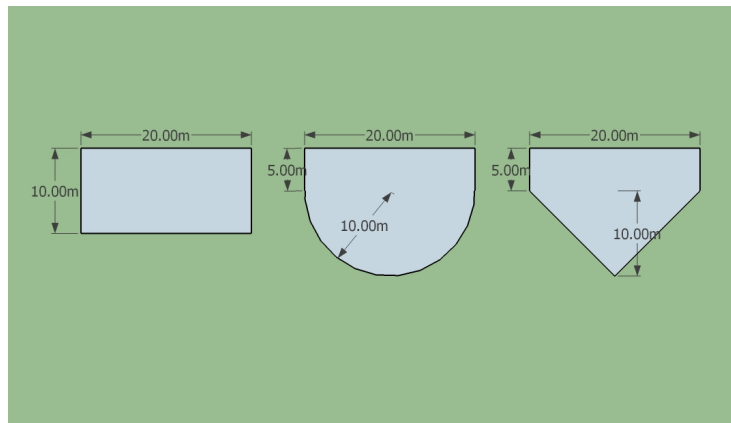


Figure 3.1: The most efficient Cylinder (Cyl8), Bullet (Bul6) and Cone (Con6) with dimensions.

Average Power Extraction, \bar{P} per Sea State [kW]

Cyl8								
4.5	6.9	94.4	352.8	686.1	663.4	642.4	629.3	615.1
3.5	4.2	57.1	213.4	415.0	401.3	388.6	380.7	372.1
2.5	2.1	29.1	108.9	211.8	204.8	198.3	194.2	189.8
1.5	0.8	10.5	39.2	76.2	73.7	71.4	69.9	68.3
0.5	0.1	1.2	4.4	8.5	8.2	7.9	7.8	7.6
$H_s [m]$ / $T_z [s]$	3.5	4.5	5.5	6.5	7.5	8.5	9.5	10.5

Table 3.11: Average extracted power, \bar{P} per sea state for Cyl8 [kW].

Bul6								
4.5	9.5	108.5	364.0	660.3	647.6	631.7	619.8	606.0
3.5	5.8	65.6	220.2	399.5	391.7	382.2	374.9	366.6
2.5	2.9	33.5	112.4	203.8	199.9	195.0	191.3	187.0
1.5	1.1	12.1	40.4	73.4	72.0	70.2	68.9	67.3
0.5	0.1	1.3	4.5	8.2	8.0	7.8	7.7	7.5
$H_s [m]$ / $T_z [s]$	3.5	4.5	5.5	6.5	7.5	8.5	9.5	10.5

Table 3.12: Average extracted power, \bar{P} per sea state for Bul6 [kW].

Con6								
4.5	36.9	205.3	485.2	563.1	588.1	600.7	602.7	596.5
3.5	22.3	124.2	293.5	340.7	355.8	363.4	364.6	360.8
2.5	11.4	63.4	149.7	173.8	181.5	185.4	189.0	184.1
1.5	4.1	22.8	53.9	62.6	65.3	66.7	67.0	66.3
0.5	0.5	2.5	6.0	7.0	7.3	7.4	7.4	7.4
$H_s [m]$ / $T_z [s]$	3.5	4.5	5.5	6.5	7.5	8.5	9.5	10.5

Table 3.13: Average extracted power, \bar{P} per sea state for Con6 [kW].

Average Available Power, \bar{P}_{avail} per Sea State [kW]

The average available power, \bar{P}_{avail} per sea state is given in Table 3.14. Based on the scatter diagram in Table 1.1, the contribution of every sea state to the total available average power presented in Table 3.4, is given in Table 3.15. Cyl8, Bul6 and Con6 have the same radius ($R = 10m$) and so they have access to the same available wave power.

4.5	808.7	1068.9	1376.5	1706.0	2016.7	2289.1	2520.1	2713.5
3.5	489.2	646.6	832.7	1032.0	1220.0	1384.8	1524.5	1641.5
2.5	249.6	329.9	424.9	526.5	622.4	706.5	777.8	837.5
1.5	89.9	118.8	153.0	190.0	224.1	254.3	280.0	301.5
0.5	10.0	13.2	17.0	21.1	24.9	28.3	31.1	33.5
$H_s[m]$ / $T_z[s]$	3.5	4.5	5.5	6.5	7.5	8.5	9.5	10.5

Table 3.14: Average available power, \bar{P}_{avail} per sea state [kW].

4.5	0	2.24	15.86	33.98	29.62	14.38	5.30	2.85
3.5	0	4.06	23.55	42.20	33.27	14.50	4.81	1.73
2.5	0.26	5.88	28.04	40.30	26.12	9.62	2.45	0.88
1.5	0.28	6.10	19.39	19.68	9.40	2.66	0.59	0
0.5	0.20	1.19	1.67	0.90	0.26	0.06	0	0
$H_s[m]$ / $T_z[s]$	3.5	4.5	5.5	6.5	7.5	8.5	9.5	10.5

Table 3.15: Contribution of every sea state to the total average power, \bar{P}_{avail} [kW]. The red area of the Table represents the 80% of the total average available power.

Comments

- 80% of the total average available power, \bar{P}_{avail} is located at sea states with $T_z = 5.5s$, $T_z = 6.5s$ and $T_z = 7.5s$.
- Classifying the sea states by T_z leads to the conclusion that the sea states with $T_z = 6.5s$ are the most energetic ones cumulatively.

Efficiency per Sea State [-]

Cyl8								
4.5	0.01	0.09	0.26	0.40	0.33	0.28	0.25	0.23
3.5	0.01	0.09	0.26	0.40	0.33	0.28	0.25	0.23
2.5	0.01	0.09	0.26	0.40	0.33	0.28	0.25	0.23
1.5	0.01	0.09	0.26	0.40	0.33	0.28	0.25	0.23
0.5	0.01	0.09	0.26	0.40	0.33	0.28	0.25	0.23
$H_s[m]$ / $T_z[s]$	3.5	4.5	5.5	6.5	7.5	8.5	9.5	10.5

Table 3.16: Efficiency per sea state for Cyl8. In red color the sea states with the highest Efficiency.

Bul6								
4.5	0.01	0.10	0.26	0.39	0.32	0.28	0.25	0.22
3.5	0.01	0.10	0.26	0.39	0.32	0.28	0.25	0.22
2.5	0.01	0.10	0.26	0.39	0.32	0.28	0.25	0.22
1.5	0.01	0.10	0.26	0.39	0.32	0.28	0.25	0.22
0.5	0.01	0.10	0.26	0.39	0.32	0.28	0.25	0.22
$H_s[m]$ / $T_z[s]$	3.5	4.5	5.5	6.5	7.5	8.5	9.5	10.5

Table 3.17: *Efficiency* per sea state for Bul6. In red color the sea states with the highest *Efficiency*.

Con6								
4.5	0.05	0.19	0.35	0.33	0.29	0.26	0.24	0.22
3.5	0.05	0.19	0.35	0.33	0.29	0.26	0.24	0.22
2.5	0.05	0.19	0.35	0.33	0.29	0.26	0.24	0.22
1.5	0.05	0.19	0.35	0.33	0.29	0.26	0.24	0.22
0.5	0.05	0.19	0.35	0.33	0.29	0.26	0.24	0.22
$H_s[m]$ / $T_z[s]$	3.5	4.5	5.5	6.5	7.5	8.5	9.5	10.5

Table 3.18: *Efficiency* per sea state for Con6. In red color the sea states with the highest *Efficiency*.

Comments

- Cyl8 and Bul6 achieve their highest *Efficiency* for sea states with $T_z = 6.5s$ which are the most energetic ones. Con6 achieves its highest *Efficiency* for sea states with $T_z = 5.5s$.
- All the three designs have better *Efficiency* for sea states with $T_z \geq 5.5s$ comparing to sea states with $T_z \leq 4.5s$.

Excitation Force Amplitudes, $F_{exc,a}(\omega)$.

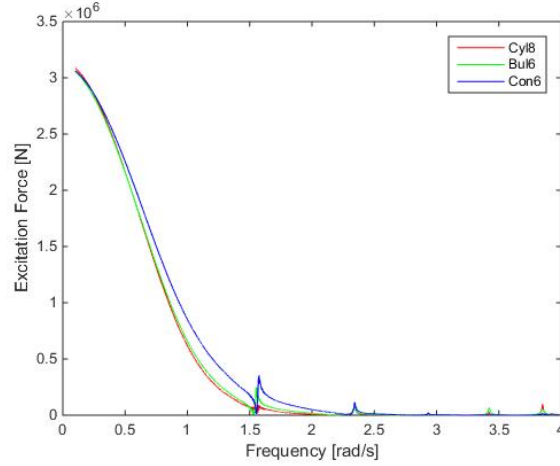


Figure 3.2: Excitation force amplitudes, $F_{exc,a}(\omega)$ per frequency [N].

Comments

- Con6 appears to be exposed to larger excitation force, F_{exc} than Cyl8 and Bul6 especially for relatively high frequencies.
- It is known by literature (Wellens, 2004) that the excitation force, F_{exc} increases with decreasing draft, TD of the buoy. It would be expected that Cyl8 which has smaller draft to be exposed to larger excitation force but this is not validated by the findings.

Mass, m of the Designs [tonnes]

The masses of the evaluated designs are given in Table 3.19, 3.20 and 3.21.

Cylinder		5	10	15
$R[m]$	$CL[m]$			
5		403	805	1208
7.5		906	1811	2717
10		1610	3220	4830

Table 3.19: Mass of Cylinder designs [tonnes]. In green color the Cylinder with the largest *Efficiency* (Cyl8).

Bullet			
$R[m]$ \ / $CL[m]$	5	7.5	10
5	671	872	1073
7.5	1811	2264	
10	3756		

Table 3.20: Mass of Bullet designs [tonnes]. In green color the Bullet with the largest *Efficiency* (Bul6).

Cone			
$R[m]$ \ / $CL[m]$	5	7.5	10
5	537	738	939
7.5	1358	1811	
10	2683		

Table 3.21: Mass of Cone designs [tonnes]. In green color the Cone with the largest *Efficiency* (Con6).

Comments

- The masses presented, correspond to the under water mass of every design at equilibrium position.
- For Bullet and Cone sets, the design with the largest mass was also the design with the largest *Efficiency*.
- Within all the twenty-one designs, the one with the largest mass was Cyl9. Cyl9 had 50% larger mass than Cyl8 which was found to be the most efficient design within the Cylinder set.
- It appears that for every different shape, there is an optimum mass or equivalently volume which maximizes *Efficiency*.
- The dimension restrictions, as presented in § 1.2, play an important role. The maximum *Efficiency* of Bullet and Cone designs may have been larger, if they were allowed to attain larger mass.

Added Mass, $a(\omega)$ [tonnes]

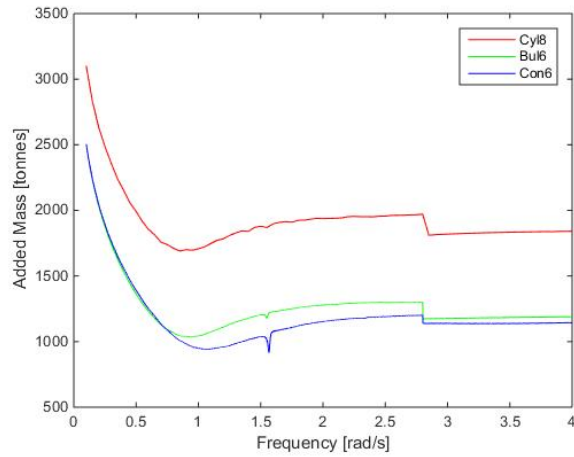


Figure 3.3: The added mass coefficient, $a(\omega)$ for Cyl8, Bul6 and Con6.

Comments

- Cyl8 has much larger added mass coefficients, $a(\omega)$ comparing to Bul6 and Con6.
- Bul6 has larger added mass coefficients, $a(\omega)$ than Con6 for frequencies larger than 0.75rad/s .

Damping Coefficient, $b(\omega)$ [tonnes/s]

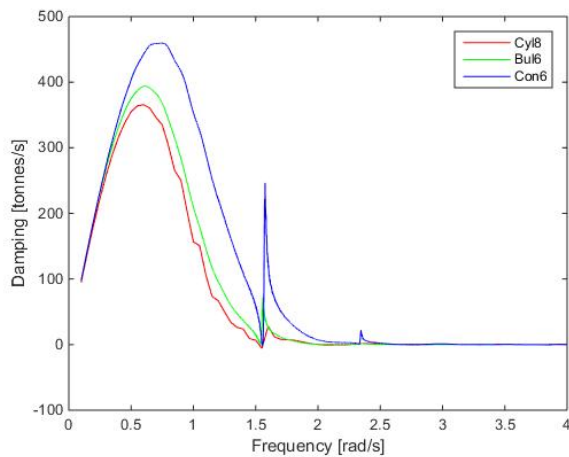


Figure 3.4: The damping coefficient, $b(\omega)$ for Cyl8, Bul6 and Con6.

Comments

- Con6 is a better wave maker than Cyl8 and Bul6. As a result of its larger radiation damping coefficients, $b(\omega)$, Con6 radiates more energy than Cyl8 and Bul6 for the same oscillation. The worst wave maker is Cyl8.
- A numerical instability is observed for a frequency of 1.5rad/s , especially for Con6. This kind of numerical instabilities are quite common for BEM code simulations. In any case the instability occurs at a frequency where rather little energy exists according to the JONSWAP spectrum used and results cannot be influenced significantly.

Restoring Coefficient, c [tonnes/s²]

The restoring coefficient, c for Cyl8, Bul6 and Con6 is the same for all the three designs as they have the same radius and consequently the same water-line area, A_{wl} . Their restoring coefficient, c is calculated as:

$$c = \rho g A_{wl} = 3159 \text{ tonnes/s}^2 \quad (3.2)$$

Spring Stiffness Coefficient, k_{sp} per Sea State [tonnes/s²]

Cyl8									
4.5	6691	2687	717	0	0	0	0	0	0
3.5	6691	2687	717	0	0	0	0	0	0
2.5	6691	2687	717	0	0	0	0	0	0
1.5	6691	2687	717	0	0	0	0	0	0
0.5	6691	2687	717	0	0	0	0	0	0
H_s [m] / T_z [s]	3.5	4.5	5.5	6.5	7.5	8.5	9.5	10.5	

Table 3.22: Spring stiffness coefficients, k_{sp} for Cyl8 per sea state [tonnes/s²]. The red area represents the sea states for which *resonance* at the peak frequency, ω_p was achieved. The green area represents the sea states with the highest *Efficiency*.

Bul6									
4.5	6443	2524	623	0	0	0	0	0	0
3.5	6443	2524	623	0	0	0	0	0	0
2.5	6443	2524	623	0	0	0	0	0	0
1.5	6443	2524	623	0	0	0	0	0	0
0.5	6443	2524	623	0	0	0	0	0	0
H_s [m] / T_z [s]	3.5	4.5	5.5	6.5	7.5	8.5	9.5	10.5	

Table 3.23: Spring stiffness coefficients, k_{sp} for Bul6 per sea state [tonnes/s²]. The red area represents the sea states for which *resonance* at the peak frequency, ω_p was achieved. The green area represents the sea states with the highest *Efficiency*.

Con6								
4.5	4034	1111	0	0	0	0	0	0
3.5	4034	1111	0	0	0	0	0	0
2.5	4034	1111	0	0	0	0	0	0
1.5	4034	1111	0	0	0	0	0	0
0.5	4034	1111	0	0	0	0	0	0
$H_s [m]$ / $T_z [s]$	3.5	4.5	5.5	6.5	7.5	8.5	9.5	10.5

Table 3.24: Spring stiffness coefficients, k_{sp} for Con6 per sea state [tonnes/s²]. The red area represents the sea states for which *resonance* at the peak frequency, ω_p was achieved. The green area represents the sea states with the highest *Efficiency*.

Comments

- The spring stiffness coefficient, k_{sp} per sea state is calculated by Eq. (2.27). The equation is satisfied for sea states whose spring stiffness coefficient, k_{sp} is larger than zero. The spring stiffness coefficient, k_{sp} cannot be negative in physical terms.
- For the sea states which have positive spring stiffness coefficient, k_{sp} the buoy is at *resonance* with the peak frequency, ω_p of the sea state. It means that the so-called *natural frequency* of the buoy coincides with this peak frequency, ω_p .
- Con6 is at *resonance* for less sea states than Cyl8 and Bul6 which are resonating further in the scatter diagram.
- All the three designs achieve their highest *Efficiency* at sea states where *resonance* is not achieved. At $T_z = 6.5s$ for Cyl8 and Bul6 and at $T_z = 5.5s$ for Con6.
- All the three designs achieve their highest *Efficiency* for the sea states immediately after the resonated part of the scatter diagram. This finding is also valid for all the twenty-one designs.
- When the buoy is at *resonance*, its velocities, \dot{z}_b become larger as it would be expected. This is also validated by statistics derived by the Frequency Domain model, regarding the significant relative velocity amplitudes, $V_{sign,rel}$ per sea state.

PTO Damping Coefficient, β per Sea State [tonnes/s]

Cyl8								
4.5	24	118	253	587	1618	2601	3496	4365
3.5	24	118	253	587	1618	2601	3496	4365
2.5	24	118	253	587	1618	2601	3496	4365
1.5	24	118	253	587	1618	2601	3496	4365
0.5	24	118	253	587	1618	2601	3496	4365
$H_s [m]$ / $T_z [s]$	3.5	4.5	5.5	6.5	7.5	8.5	9.5	10.5

Table 3.25: PTO damping coefficients, β for Cyl8 per sea state [tonnes/s].

Bul6								
4.5	37	156	292	672	1688	2653	3545	4402
3.5	37	156	292	672	1688	2653	3545	4402
2.5	37	156	292	672	1688	2653	3545	4402
1.5	37	156	292	672	1688	2653	3545	4402
0.5	37	156	292	672	1688	2653	3545	4402
$H_s [m]$ / $T_z [s]$	3.5	4.5	5.5	6.5	7.5	8.5	9.5	10.5

Table 3.26: PTO damping coefficients, β for Bul6 per sea state [tonnes/s].

Con6								
4.5	110	301	515	1449	2375	3256	4083	4890
3.5	110	301	515	1449	2375	3256	4083	4890
2.5	110	301	515	1449	2375	3256	4083	4890
1.5	110	301	515	1449	2375	3256	4083	4890
0.5	110	301	515	1449	2375	3256	4083	4890
$H_s [m]$ / $T_z [s]$	3.5	4.5	5.5	6.5	7.5	8.5	9.5	10.5

Table 3.27: PTO damping coefficients, β for Con6 per sea state [tonnes/s].

Comments

- The PTO damping coefficient, β is calculated by Eq. (2.28). As no restrictions are applied for the force delivered by the PTO device, F_{pto} the equation is satisfied for all the sea states.
- For the sea states where *resonance* is achieved, the PTO damping coefficient, β coincides with the radiation damping coefficient of the peak frequency, $b(\omega_p)$. Otherwise, $\beta > b(\omega_p)$.
- Within the three final designs, Con6 has the largest PTO damping coefficients, β as it could be expected by the fact that Con6 has also larger radiation damping coefficients, $b(\omega)$.

- Increasing the PTO damping coefficient will subsequently decrease the buoy's oscillation velocities, \dot{z}_b .

3.2 Shape Evaluation

The most efficient dimensions for the Bullet, the Cone and the Cylinder were derived, based on the predetermined sets of designs evaluated. Next, the three final designs (Cyl8, Bul6 and Con6) have to be evaluated again so as the most efficient to be chosen as the final design. Methodology and results are presented.

3.2.1 Methodology

By the Frequency Domain Model a fast estimation of the *Efficiency* of the three final designs is already derived. The main issue of this estimation is that it is completely free of viscous (drag) forces. As shown by Eq. (2.44), this drag force depends on the velocity of the buoy, the velocity of the surrounding fluid and the so-called drag coefficient, C_d . In literature, a large number of studies about the determination of drag coefficients for static or floating structures in waves can be found. Physical experiments or numerical wave tank tests employing CFD codes are usually used. In both cases, the method involves the oscillation of the structure in still water and measurements of the force exerted on the structure (Bhinder et al., 2011) (Thilleul, 2013) (Cozijn, 2005). Another common element found in studies about the determination of the drag coefficient is the dependency of the derived coefficients on the dimensionless parameters of the *Keulegan-Carpenter* and the *Reynolds* number (Chakrabarti, 2005). In this report, CFD code ComFLOW3 is employed for producing *Forced Oscillation Tests* (FOT) of the studied designs in a numerical wave tank. A new approach for the calculation of the drag coefficient is proposed. Next, the Time Domain Model (see § 2.6) will be employed for deriving *Efficiency* estimations, including a drag force assessment. A Runge-Kutta, fourth order accurate time discretization is employed and a method for calculating and comparing the *Efficiency* of the Bullet, the Cone and the Cylinder is proposed.

Drag Coefficient Determination

Forced Oscillation Tests (FOT) are setup in a numerical tank in ComFLOW3 (Figure 3.5). For FOT, there is no presence of waves and the water mass is calm at the beginning of the simulation. The body is forced to oscillate vertically, through the free surface of water and the position of its center in time is given by:

$$z_b(t) = a_{osc} \cdot \cos(\omega_{osc}t) \quad (3.3)$$

Where:

$$\begin{aligned} a_{osc} &= \text{the amplitude of the oscillation [m]} \\ \omega_{osc} &= \text{the frequency of the oscillation [rad/s]} \end{aligned}$$

Detailed description of the setup of FOT in ComFLOW3 can be found in Appendix B.

Once the simulation has finished, ComFLOW3 returns the time-dependent estimation of the force exerted on the oscillating body by integrating the calculated pressures across the area of its surface boundary (Figure 3.6). It is

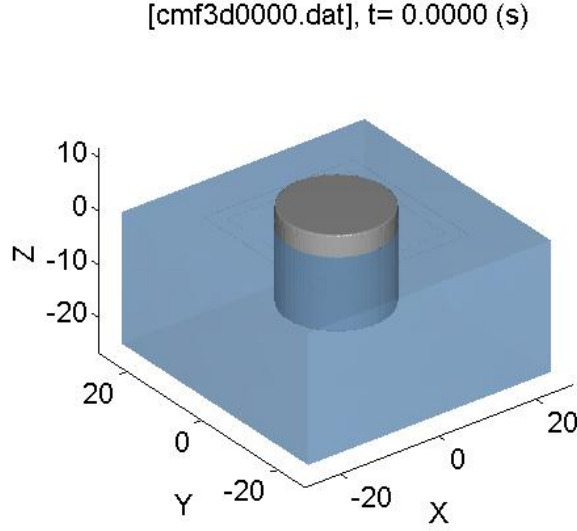


Figure 3.5: 3D depiction of the numerical tank in ComFLOW3 for the *Forced Oscillation Test of a Cylinder*.

important now, to analyze this derived force as it was done for the case of the Mass-Spring-Damper System (MSDS) model in § 2.4. Four different forces are recognized. An added mass force, F_{add} similar to the one calculated for the MSDS model and proportional to the acceleration of the body. A time dependent hydrostatic force, F_{hyd} exerted by the varying buoyancy as a result of the varying position of the body in water. It is different than the restoring force, F_{res} of the MSDS model as in this case the gravity force is not relevant as a result of the forced oscillation. A radiation force, F_{rad} exerted on the body by the radiating waves as a result of its oscillation, proportional to the body's velocity, similarly to the MSDS model. Finally and additionally to the forces recognized in § 2.4, there is a drag force, F_{drag} as the one calculated by Eq. (2.44), exerted on the body by the shear interaction of the body's surface with water particles. This drag force has to be discretized from the total force in Figure 3.6 so as an estimation of the drag coefficient, C_d to be made. For the discretization of the drag force, initially, the periodic total force signal will be expanded in Fourier series. Only the first order terms will be kept as the force signal is produced by a sinusoidal motion of the body and the first order approximation is considered accurate. The Fourier series of the force signal reads:

$$F(t) = F_0 + F_{cos} \cos(\omega_{osc}t) + F_{sin} \sin(\omega_{osc}t) \quad (3.4)$$

Where:

- F_0 = the static part of the force [N]
- F_{cos} = the amplitude of the dynamic part of the force in-phase with the body's position and acceleration [N]
- F_{sin} = the amplitude of the dynamic part of the force in-phase with the body's velocity [N]

By Eq. (2.20), (2.44) of the radiation and drag force respectively, it is clear that

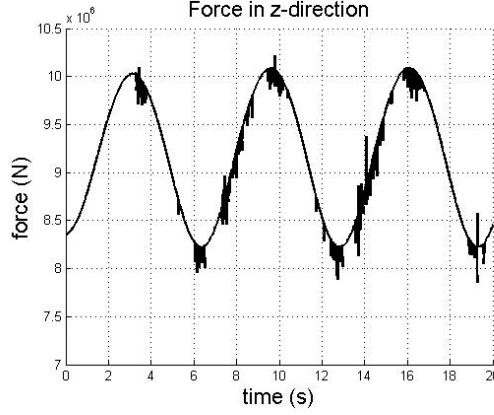


Figure 3.6: Force in the z -direction as calculated by ComFLOW3 for a *Forced Oscillation Test*.

these forces are in-phase with the body's velocity (damping forces). So these forces at any moment should constitute the second term in the right hand side of Eq. (3.4) resulting to:

$$F_{sin} \sin(\omega_{osc}t) = F_{rad}(t) + F_{drag}(t) \quad (3.5)$$

With known F_{sin} and ω_{osc} by Fourier series expansion, the determination of F_{rad} will lead to the determination of F_{drag} and consequently to the determination of the drag coefficient, C_d by fitting of Eq. (2.44) to the derived drag force. Although this approach has a reasonable physical background, it also has a specific problem in its implementation. The problem is that the radiation force cannot be calculated directly but only in terms of measuring the radiated waves at a certain position away from the structure position. Consequently, a phase shift between the force measured and the exerted radiation force on the body has to be applied. This phase shift has to do with the propagation speed of the radiated waves. In this report an alternative approach is proposed which simplifies the process without the need of phase shift calculation. The approach takes advantage of the relations between force and power.

On the contrary to the sinusoidal signal of force, power can be averaged over one or multiple wave cycles without providing zero outcome. From physics we get that:

$$Power = Force \times Velocity$$

The body's sinusoidal velocity is known and given by:

$$\dot{z}_b(t) = -\omega_{osc}a_{osc} \sin(\omega_{osc}t) \quad (3.6)$$

Following these, the instantaneous power produced by the radiation and the drag forces can be calculated by:

$$P_{rad}(t) = F_{rad}(t) \cdot \dot{z}_b(t) \quad (3.7)$$

$$P_{drag}(t) = F_{drag}(t) \cdot \dot{z}_b(t) \quad (3.8)$$

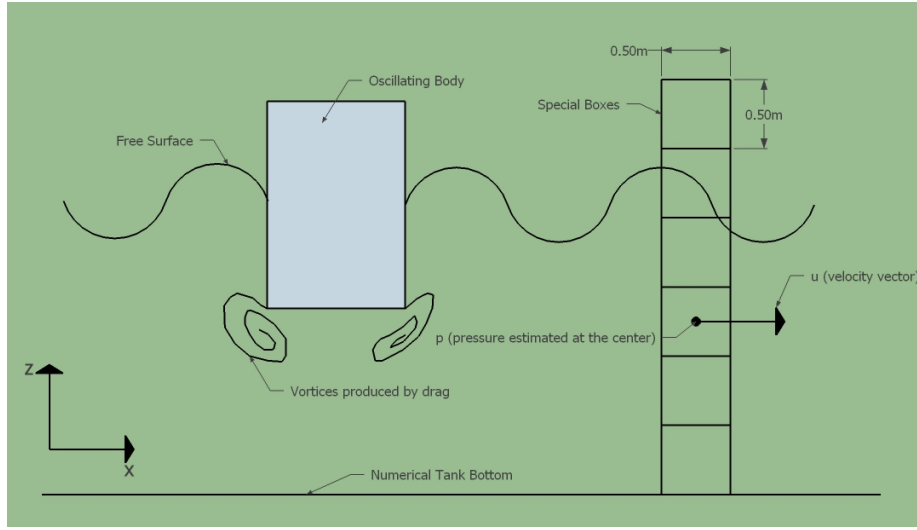


Figure 3.7: Structure of the computational domain with the use of *special boxes* in the xz -plane during a *Forced Oscillation Test*.

Analogously, the power produced by the part of the force in-phase with the velocity reads:

$$P_{sin}(t) = F_{sin} \sin(\omega_{osct}) \cdot \dot{z}_b(t) \quad (3.9)$$

Then, at any moment the following relation should stand:

$$P_{sin}(t) = P_{rad}(t) + P_{drag}(t) \quad (3.10)$$

Averaging over one or multiple wave cycles leads to the averaged form of Eq. (3.10) as:

$$\bar{P}_{sin} = \bar{P}_{rad} + \bar{P}_{drag} \quad (3.11)$$

Of course, \bar{P}_{sin} is already known. It is needed then, to calculate \bar{P}_{rad} and this is implemented via an option available in ComFLOW3 called *Special Box* (SB).

With SB in ComFLOW3, it is possible to derive estimation of pressure, p and velocity components u , v and w at the center of every cell at a specific horizontal location of the domain for the total length of the water column. In Figure 3.7 a 2D depiction of the structure of the SB utility is presented. Furthermore, it should be noted that the radiation waves have circular crests. Care should be taken for the calculated velocities to be projected on the parallel to the propagation direction at the selected location. For simplifying calculation, SB can be located either where $x = 0$ or $y = 0$. The size of the boxes coincides with the size of the computational grid at the selected location. Then, with the information from the SB gathered, it is possible to calculate the average power, \bar{P}_{rad} over one wave cycle, which is produced by the radiation force, F_{rad} . This average power will be equal to the average energy transfer through the SB over the same amount of time. According to physics:

$$Power = Pressure \times Area \times Velocity$$

Pressure and velocity are calculated at every time step by ComFLOW3 and the area, A is equal to the area of the lateral face of the SB. For every SB then, the

instantaneous power is given by:

$$P_{SB}(t) = p \cdot A \cdot u \quad (3.12)$$

Integrating for the whole water column results to the instantaneous radiation power. Averaging then over one wave cycle returns finally the average radiated power, \bar{P}_{rad} .

With \bar{P}_{rad} and \bar{P}_{sin} estimated, Eq. (3.11) is rearranged for \bar{P}_{drag} to be estimated as:

$$\bar{P}_{drag} = \bar{P}_{sin} - \bar{P}_{rad} \quad (3.13)$$

Now that an estimation for the average power subtracted by the system because of drag force exists, focus turns back to the relation of the drag force F_{drag} which produces this power. Eq. (2.44) estimates the drag force for the case of an oscillating structure in the presence of waves. In the FOT employed in this research, imposed waves do not exist and so it is assumed that there is no relative velocity between the body and the water particles. This assumption allows for using the form of Morison drag force for structures oscillating in still water (Journée and Massie, 2001) which reads:

$$F_{drag}(t) = -\frac{1}{2}\rho C_d A_{wl} |\dot{z}_b(t)| \dot{z}_b(t) \quad (3.14)$$

Substituting Eq. (3.14) and (3.6) in Eq. (3.8) results to the following relation for the instantaneous drag power:

$$P_{drag}(t) = \frac{1}{2}\rho C_d A_{wl} \omega_{osc}^3 a_{osc}^3 |\sin(\omega_{osc}t)| \sin^2(\omega_{osc}t) \quad (3.15)$$

Averaging Eq. (3.15) over one period gives:

$$\bar{P}_{drag} = \frac{1}{T} \int_0^T P_{drag}(t) dt \quad (3.16)$$

The only unknown is the drag coefficient, C_d . It can be derived by fitting the right hand side of Eq. (3.16) so as the derived \bar{P}_{drag} to match the estimation of \bar{P}_{drag} from Eq. (3.13).

Drag Coefficient Parametrization

Forced Oscillation Tests and the methodology presented in the previous section can be used so as to derive drag coefficients, C_d for the three studied designs. Then, the Time Domain Model, including estimation of the nonlinear drag force, F_{drag} can be employed for *Efficiency* estimations. The main problem to tackle now is that the drag coefficients calculated depend on the flow conditions and the body's velocity. It is expected that for different frequencies and amplitudes of oscillation, the *Forced Oscillation Tests* will provide different drag coefficients. Parameterization of the drag coefficient derived by FOT is needed.

In § 2.10, the KC and Re numbers were introduced. These numbers have to be determined for the case of FOT. In FOT the body is oscillated through still water. As waves are absent, oscillation of water particles due to waves is also absent. This way the the maximum velocity, V_m appearing in Eq. (2.47) and (2.48) is replaced by the oscillated body's maximum velocity as:

$$V_m = \omega_{osc} \cdot a_{osc} \quad (3.17)$$

Substituting Eq. (3.17) in Eq. (2.47) results to:

$$KC = \frac{\omega_{osc} a_{osc} T}{D} \quad (3.18)$$

As the motion of the body in FOT is sinusoidal, then the frequency of oscillation is given by: $\omega_{osc} = 2\pi/T$. Substituting in Eq. (3.18) leads to the KC number for FOT as:

$$KC = \frac{2\pi a_{osc}}{D} \quad (3.19)$$

Substituting Eq. (3.17) in Eq. (2.48) leads to the expression for the Re number for FOT as:

$$Re = \frac{\omega_{osc} a_{osc} D}{\nu} \quad (3.20)$$

Accordingly, for every FOT, a KC and a Re number can be assigned. So as to derive the drag coefficient for various conditions, a number of predetermined FOT can be conducted. Then drag coefficient adjustment can be made by interpolation.

Drag Force, F_{drag} Determination

The drag force, F_{drag} in literature is usually calculated according to the strip method presented in § 2.6.3. An alternative approach is presented here.

The relative velocity, V_{rel} at the center of the bottom of the buoy is known at every time step and given by:

$$V_{rel}(t) = \dot{z}_b(t) - w(t) \quad (3.21)$$

The stagnation pressure at the center of the bottom, as presented in chapter 3 of Journée and Massie (2001), is given by:

$$p_{st} = \frac{1}{2} \rho V_{rel}^2 \quad (3.22)$$

The shape of the bottom of the buoy influences the pressure distribution at all the other points of the bottom. This influence is quantified by the dimensionless drag coefficient, C_d . Finally, multiplying Eq. (3.22) with the water-line area, A_{wl} and the drag coefficient, C_d results to the common form of the drag part of the Morison force for the case of an oscillating vertical cylinder in waves:

$$F_{drag}(t) = -\frac{1}{2} \rho C_d A_{wl} |V_{rel}| V_{rel} \quad (3.23)$$

The difference now is that this force includes also the vertical water particles' velocity, w and the relative velocity approach is satisfied also for oscillating bodies in waves. Moreover, this approach is much faster than the approach of dividing the buoy to horizontal strips. At every time step the water particles' velocity, w is needed to be calculated only at the bottom of the buoy. A test case for comparing the two approaches is set up.

For the test case, a time series of free surface elevation is produced. The length of the time series is set to 100s. A Bullet shape buoy is assumed. A random drag coefficient, $C_d = 1$ is chosen for both the approaches. The diameter, D is set to 20m and the under water length of the cylindrical part, CL is set

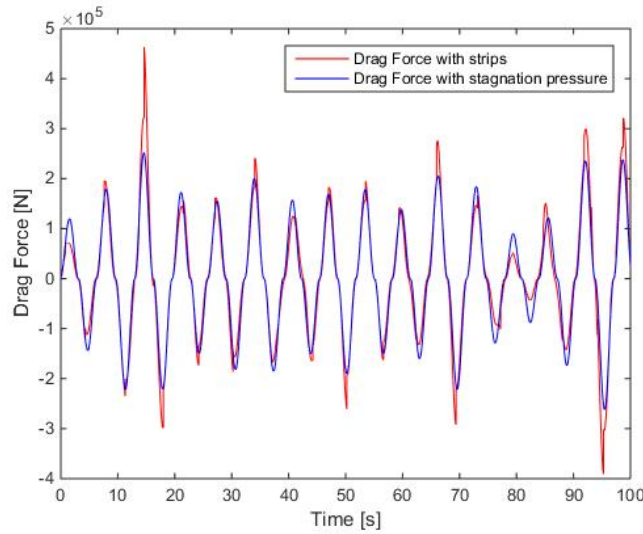


Figure 3.8: Test case for comparing the two different methods for calculating the drag force, F_{drag} .

to $5m$ (see also Fig.1.2). The Bullet is subjected to a forced oscillation of $1m$ with oscillation frequency of $0.97rad/s$. Results for the test case are shown in Figure 3.8. It can be noticed that the two approaches provide a quite similar drag force. The strip method seems to give some high peaks which are not found by the method using the stagnation pressure. This probably has to do with the fact that the motion of the body is forced and irrelevant to the incoming waves which is not physical. The average power produced by the two drag force signals was calculated. The difference was found to be less than 1%. Nevertheless, the method with the calculation of the stagnation pressure is much faster and according to the author's opinion more physically correct, at least for vertically oscillating bodies in waves. Hence, in this report, the drag force, F_{drag} is calculated using the stagnation pressure method.

Efficiency Comparison

The methodology for adjusting the drag coefficient, presented in the previous chapter, has a specific drawback. A large number of CFD simulations is needed so as to provide a representative grid of KC and Re numbers for drag coefficient determination. It should be noted that for a 12 core Intel Xeon server with 50 GB of RAM, ComFLOW3 needed seven days for completing nine FOT with the simulation time being of the order of twenty seconds. In this design phase of comparing the three most efficient designs, providing a representative set of FOT for every one of the three tested designs with the available resources would take more than a month. Model accuracy in this phase is considered of secondary importance. What is more important is to derive a fair *Efficiency* comparison between the three designs. Another approach is proposed.

The Bullet, the Cone and the Cylinder will be tested under the same conditions. The frequency of oscillation is set to $\omega_{osc} = 0.97rad/s$. This frequency

corresponds to the zero-crossing period $T_z = 6.5s$ of the sea states with the highest average available power in combination with the occurrence rates as these are described by the scatter diagram. The calculations of the average available power per sea state have been made with Eq. (2.15). Three different oscillation amplitudes, a_{osc} are tested for every shape: $a_{osc} = 0.5m$, $a_{osc} = 1m$ and $a_{osc} = 2m$. The drag force, F_{drag} depends on the square of the relative velocity between the buoy and water particles and of course on the drag coefficient, C_d . For applying the values derived by FOT for the *Shape Evaluation* in Time Domain model, information about the predicted relative velocity, V_{rel} is needed. This information will be different for every design and for every sea state. Information on the relative velocity can be derived by Frequency Domain statistics. The significant relative velocity amplitude between the sea surface and the body, $V_{rel,sign}$ per sea state can be derived as:

$$V_{sign,rel} = 2\sqrt{\int_0^\infty S_{V_{rel}}(\omega_n)d\omega} \quad (3.24)$$

$$\int_0^\infty S_{V_{rel}}(\omega_n)d\omega = \sum_{n=1}^N \frac{1}{2} V_{rel,a_n}^2 \quad (3.25)$$

$$V_{rel,a_n} = \omega_n \sqrt{(\zeta_a - z_a \cos(\epsilon_{z\zeta}))^2 + (z_a \sin(\epsilon_{z\zeta}))^2} \quad (3.26)$$

Where:

- $V_{sign,rel}$ = The significant amplitude of the relative velocity, V_{rel} between the sea surface and the buoy [m/s]
- V_{rel,a_n} = The relative velocity amplitude of the frequency component, ω_n [m/s]
- $S_{V_{rel}}$ = The spectrum of the relative velocities, V_{rel} [m²]

For sea states with larger $V_{sign,rel}$, the drag coefficient derived by FOT with $a_{osc} = 2m$ will be applied and so on. Detailed setup of the Time Domain Model is provided in Appendix C.

3.2.2 Results

The three final designs, i.e Cyl8, Bul6 and Con6, were compared so as the most efficient to be derived. Hence, in this chapter, the three final designs will be referred to as *Cylinder*, *Bullet* and *Cone*. The results of the drag coefficient, C_d determination and the Time Domain model are presented.

Drag Coefficients, C_d [-]

<i>Cylinder</i>				
a_{osc} [m]	ω_{osc} [rad/s]	KC [-]	Re [-]	C_d [-]
2	0.97	0.63	$3.98 \cdot 10^7$	0.73
1	0.97	0.31	$1.99 \cdot 10^7$	2.95
0.5	0.97	0.16	$0.9 \cdot 10^7$	2.85

Table 3.28: *Forced Oscillation Tests*, KC and Re numbers and the derived drag coefficients, C_d for the *Cylinder*.

<i>Bullet</i>				
$a_{osc}[m]$	$\omega_{osc}[rad/s]$	$KC[-]$	$Re[-]$	$C_d[-]$
2	0.97	0.63	$3.98 \cdot 10^7$	0.53
1	0.97	0.31	$1.99 \cdot 10^7$	1.06
0.5	0.97	0.16	$0.9 \cdot 10^7$	2.71

Table 3.29: *Forced Oscillation Tests*, KC and Re numbers and the derived drag coefficients, C_d for the *Bullet*.

<i>Cone</i>				
$a_{osc}[m]$	$\omega_{osc}[rad/s]$	$KC[-]$	$Re[-]$	$C_d[-]$
2	0.97	0.63	$3.98 \cdot 10^7$	0.63
1	0.97	0.31	$1.99 \cdot 10^7$	1.06
0.5	0.97	0.16	$0.9 \cdot 10^7$	2.19

Table 3.30: *Forced Oscillation Tests*, KC and Re numbers and the derived drag coefficients, C_d for the *Cone*.

Next, the application of the derived drag coefficients in the Time Domain Model is discussed. In § 3.2.1, the derivation of the significant relative velocity amplitude, $V_{sign,rel}$ was presented. Based on the derived values by the Frequency Domain model, one of the derived drag coefficients, C_d is assigned to every sea state. The exact way the coefficients were assigned is shown in Table 3.31.

Range[m/s]	<i>Cylinder</i>	<i>Bullet</i>	<i>Cone</i>
$V_{sign,rel} \leq 1$	2.85	2.71	2.19
$1 \leq V_{sign,rel} \leq 1.5$	2.95	1.06	1.06
$1.5 \leq V_{sign,rel}$	0.73	0.53	0.63

Table 3.31: Drag coefficient, C_d assignment to sea states based on significant relative velocity values derived by Frequency Domain model.

Comments

- The *Cylinder* provides the largest drag coefficients, C_d for all the three different oscillations comparing to the *Bullet* and the *Cone*. This translates to larger drag forces, F_{drag} acting on the *Cylinder*. This finding could also be expected by the larger added mass coefficients, $a(\omega)$ of the *Cylinder* (Figure 3.3). It is reminded that added mass is connected to the acceleration of water particles around the surface of the design. Larger acceleration of water particles is reasonable to produce larger viscous effects.
- The *Cone* has smaller drag coefficient, C_d than the *Bullet* for the low velocity forced oscillation ($\omega_{osc} = 0.97rad/s$, $a_{osc} = 0.5m$) than the *Bullet*. This could be expected by the larger added mass coefficients, $a(\omega)$ of the *Bullet* comparing to the *Cone* (Figure 3.3).
- When the forced oscillations become faster, viscous effects become more significant. These effects cannot be captured by Frequency Domain models. For the high velocity forced oscillation ($\omega_{osc} = 0.97rad/s$, $a_{osc} = 2m$),

the drag coefficient, C_d of the *Cone* is 20% larger than the one of the *Bullet*. This translates to 20% larger drag forces, F_{drag} .

- The method for applying the derived drag coefficients, C_d and keep them steady for a whole sea state is an approximation aiming to denote the difference between the oscillation of different designs at different predicted velocities. It is obvious from results that the drag coefficient, C_d becomes smaller for higher oscillation velocities and reversely. Comparison and not accuracy is the aim.

Time Domain Model

The Time Domain Model as presented in § 2.6, including the drag force, F_{drag} as this was estimated in § 3.2.1, was employed for providing *Efficiency* estimations for the three final designs. The *Efficiency* estimations derived by the Frequency Domain model did not include any viscous effects and so a more physically accurate evaluation is needed. Detailed setup of the Time Domain model can be found in Appendix C. A time step of $0.1s$ was employed for assessing all the sea states for the three final designs and deriving a total average *Efficiency*. This time step was derived as sufficient by the Time Domain model validation (see chapter 5). With this time step, the simulation time for every design lasted $1h30min$. The values of the spring stiffness coefficient, k_{sp} and the PTO damping coefficient, β were kept the same as for the Frequency Domain simulations. Results and comments are presented.

Average Power Extraction, \bar{P} per Sea State [kW]

<i>Cylinder</i>								
4.5	3.0	59.7	238.2	533.2	616.9	617.9	582.3	581.2
3.5	2.0	39.0	155.2	335.6	376.5	353.8	358.1	355.6
2.5	1.1	21.6	84.6	178.0	194.9	184.2	185.6	183.5
1.5	0.3	6.1	24.5	55.7	67.1	68.1	67.8	66.8
0.5	0.0	0.9	3.6	7.4	7.8	7.8	7.6	7.5
$H_s[m]$ / $T_z[s]$	3.5	4.5	5.5	6.5	7.5	8.5	9.5	10.5

Table 3.32: Average extracted power, \bar{P} per sea state for the *Cylinder* from Time Domain simulation [kW].

<i>Bullet</i>								
4.5	5.5	80.0	275.0	558.3	613.5	612.9	599.5	591.4
3.5	3.5	51.1	175.6	346.7	362.5	366.9	364.9	351.3
2.5	1.9	27.5	93.9	170.3	188.4	182.5	183.3	181.1
1.5	0.7	9.6	33.1	57.2	66.3	67.2	66.9	65.9
0.5	0.1	1.1	3.8	7.3	7.7	7.6	7.5	7.4
$H_s[m]$ / $T_z[s]$	3.5	4.5	5.5	6.5	7.5	8.5	9.5	10.5

Table 3.33: Average extracted power, \bar{P} per sea state for the *Bullet* from Time Domain simulation [kW].

<i>Cone</i>								
4.5	26.0	163.3	394.1	527.3	568.3	580.9	587.6	584.8
3.5	16.5	102.9	247.5	322.0	340.8	353.4	351.9	350.5
2.5	8.9	54.8	130.7	163.3	171.7	178.5	181.0	180.1
1.5	3.2	19.7	43.0	58.2	62.9	65.0	65.7	65.3
0.5	0.4	2.3	5.4	6.7	7.1	7.3	7.4	7.3
$H_s[m]$ / $T_z[s]$	3.5	4.5	5.5	6.5	7.5	8.5	9.5	10.5

Table 3.34: Average extracted power, \bar{P} per sea state for the *Cone* from Time Domain simulation [kW].

Efficiency per Sea State [-]

<i>Cylinder</i>								
4.5	0.004	0.06	0.17	0.31	0.31	0.27	0.23	0.22
3.5	0.004	0.06	0.19	0.33	0.31	0.26	0.23	0.22
2.5	0.004	0.07	0.20	0.34	0.31	0.26	0.24	0.22
1.5	0.005	0.05	0.16	0.29	0.30	0.27	0.25	0.22
0.5	0.005	0.07	0.21	0.35	0.32	0.27	0.25	0.22
$H_s[m]$ / $T_z[s]$	3.5	4.5	5.5	6.5	7.5	8.5	9.5	10.5

Table 3.35: *Efficiency* per sea state for the *Cylinder* by Time Domain model.

<i>Bullet</i>								
4.5	0.007	0.07	0.20	0.33	0.30	0.27	0.24	0.22
3.5	0.007	0.08	0.21	0.34	0.30	0.27	0.24	0.21
2.5	0.008	0.08	0.22	0.32	0.30	0.26	0.24	0.22
1.5	0.007	0.08	0.22	0.30	0.30	0.26	0.24	0.22
0.5	0.007	0.08	0.22	0.35	0.31	0.27	0.24	0.22
$H_s[m]$ / $T_z[s]$	3.5	4.5	5.5	6.5	7.5	8.5	9.5	10.5

Table 3.36: *Efficiency* per sea state for the *Bullet* by Time Domain model.

<i>Cone</i>								
4.5	0.03	0.15	0.29	0.31	0.28	0.25	0.23	0.22
3.5	0.03	0.16	0.30	0.31	0.28	0.26	0.23	0.21
2.5	0.04	0.17	0.31	0.31	0.28	0.26	0.24	0.22
1.5	0.04	0.17	0.28	0.31	0.28	0.26	0.23	0.22
0.5	0.04	0.17	0.32	0.32	0.29	0.26	0.24	0.22
$H_s[m]$ / $T_z[s]$	3.5	4.5	5.5	6.5	7.5	8.5	9.5	10.5

Table 3.37: *Efficiency* per sea state for the *Cone* by Time Domain simulation.

Efficiency Losses per Sea State [-]

<i>Cylinder</i>									
4.5		-0.005	-0.03	-0.08	-0.09	-0.02	-0.01	-0.02	-0.01
3.5		-0.005	-0.03	-0.07	-0.08	-0.02	-0.03	-0.01	-0.01
2.5		-0.004	-0.02	-0.06	-0.06	-0.02	-0.02	-0.01	-0.01
1.5		-0.005	-0.04	-0.10	-0.11	-0.03	-0.01	-0.01	-0.01
0.5		-0.004	-0.02	-0.05	-0.05	-0.01	-0.01	-0.004	-0.003
$H_s [m]$	$T_z [s]$	3.5	4.5	5.5	6.5	7.5	8.5	9.5	10.5

Table 3.38: *Efficiency* loss per sea state for the *Cylinder* comparing to Frequency Domain model. The red area represents the sea states for which *resonance* was achieved. The green area represents the sea states with the highest *Efficiency*.

<i>Bullet</i>									
4.5		-0.005	-0.03	-0.06	-0.06	-0.01	-0.01	-0.01	-0.01
3.5		-0.005	-0.03	-0.05	-0.05	-0.02	-0.01	-0.01	-0.01
2.5		-0.004	-0.02	-0.04	-0.06	-0.02	-0.02	-0.01	-0.01
1.5		-0.005	-0.02	-0.05	-0.09	-0.03	-0.01	-0.01	-0.01
0.5		-0.004	-0.02	-0.04	-0.04	-0.01	-0.01	-0.004	-0.003
$H_s [m]$	$T_z [s]$	3.5	4.5	5.5	6.5	7.5	8.5	9.5	10.5

Table 3.39: *Efficiency* loss per sea state for the *Bullet* comparing to Frequency Domain model. The red area represents the sea states for which *resonance* was achieved. The green area represents the sea states with the highest *Efficiency*.

<i>Cone</i>									
4.5		-0.01	-0.04	-0.07	-0.02	-0.01	-0.01	-0.01	-0.004
3.5		-0.01	-0.03	-0.06	-0.02	-0.01	-0.01	-0.01	-0.01
2.5		-0.01	-0.03	-0.04	-0.02	-0.02	-0.01	-0.01	-0.004
1.5		-0.01	-0.03	-0.07	-0.02	-0.01	-0.01	-0.004	-0.003
0.5		-0.01	-0.02	-0.03	-0.01	-0.01	-0.003	-0.003	-0.002
$H_s [m]$	$T_z [s]$	3.5	4.5	5.5	6.5	7.5	8.5	9.5	10.5

Table 3.40: *Efficiency* loss per sea state for the *Cone* comparing to Frequency Domain model. The red area represents the sea states for which *resonance* was achieved. The green area represents the sea states with the highest *Efficiency*.

Comments

- For all the three final designs, the *Efficiency* losses are larger for the sea states where the buoy is at *resonance* and for the sea states with the highest *Efficiency*.

- The predicted buoy velocities become larger for sea states where the buoy is at *resonance* and consequently the drag forces, F_{drag} also become larger, lowering significantly the *Efficiency* of wave energy extraction.
- The *Cone* resonates at less sea states than the *Cylinder* and the *Bullet*. As a result, the *Efficiency* losses predicted for the *Cone* appear to be smaller in total.

Total Average Power Extraction, \bar{P} [kW]

Design	$P[kW]$
<i>Cylinder</i>	107.0
<i>Bullet</i>	109.9
<i>Cone</i>	114.1

Table 3.41: Total average power extraction, \bar{P} of the three final designs derived by the Time Domain model simulation [–].

Total Average Efficiency, Eff [–]

Design	$Eff[-]$
<i>Cylinder</i>	0.26
<i>Bullet</i>	0.27
<i>Cone</i>	0.28

Table 3.42: Total average *Efficiency*, Eff of the three final designs derived by the Time Domain model simulation [–].

Comments

- As it would have been expected by the larger drag coefficient, C_d derived, the total *Efficiency* loss for the *Cylinder* is the largest and equal to -0.06 comparing to the prediction made by the Frequency Domain model.
- The *Cone* now produces the largest total *Efficiency* within the three final designs and equal to 0.28 . The *Bullet* produces a total *Efficiency* equal to 0.27 .
- The optimum damping coefficient, β is still calculated by Eq. (2.28). Only the radiation damping, as this is expressed by the radiation damping coefficient, $b(\omega)$, is assessed for defining the optimum PTO damping coefficient, β . The inclusion of the drag force, F_{drag} has induced extra damping for the motion of the buoy. The position of the optimum PTO damping coefficient, β has also shifted as a result of the extra damping introduced. The configuration is not optimum anymore.

Final Design Selection

The *Cylinder* has the lowest *Efficiency* within the three final designs. Additionally, it produces the largest drag forces, F_{drag} as derived by the *Forced*

Oscillation Tests conducted, comparing to the other two designs. It is safe to argue that the *Cylinder* is the least efficient design. Choice has to be made between the *Bullet* and the *Cone*. The *Cone's Efficiency* is 0.01 larger than the *Cone's*. On the other hand, the *Bullet* resonates for more sea states and produces larger *Efficiency* losses than the *Cone*. This fact can be tackled to some extent by adjusting the PTO damping coefficient, β especially for the sea states which have large wave energy contribution and large losses ($T_z = 5.5 - 6.5s$). It appears that the *Bullet* has larger margins for PTO optimization than the *Cone*. This hypothesis is tested and validated in § 4.1.2. Furthermore, the fact that the *Bullet* achieves its highest *Efficiency* for the sea states with the highest energy contribution ($T_z = 6.5s$) is still an advantage. So the *Bullet* will be the final design for deriving a more physically accurate modeling of the *Point Absorber*.

3.3 Summary

The methodology and results for *Design Optimization* were presented. Three different sets of designs with varying dimensions were formatted one for each of the three shapes tested. Frequency Domain model was employed for assessing the power extraction *Efficiency* of the tested designs and the most efficient was selected within each set, namely Cyl8, Bul6 and Con6. Next, a CFD model was developed for assessing the capacity of each of the three final designs for producing viscous effects and forces. This capacity was quantified by the derivation of the so-called drag coefficient, C_d . The three final designs were forced to oscillate in a numerical wave tank under the same conditions. The *Cylinder* was found to produce the largest viscous forces for all the different *Forced Oscillation Tests*. The *Cone* produced smaller viscous forces for low velocity oscillations than the *Bullet* but higher for high velocity oscillations. For including the drag force, F_{drag} in the Time Domain model, an alternative approach of estimation was proposed based on the definition of the stagnation pressure. A test case was setup for comparing the alternative approach to the one usually used in literature by dividing the cross-section of the buoy to strips. Good agreement was found. Next, for deriving the *Efficiency* of power extraction for the three final designs the derived drag coefficients, C_d were assigned to every sea state in the Time Domain model based on the significant relative velocity, $V_{sign,rel}$ derived by the Frequency Domain model. The *Cylinder* was found to have the largest losses due to viscous damping within the three final designs. The losses for the *Bullet* and the *Cone* were more comparable. The *Bullet* was selected as the most efficient design as it resonated closer to the most energetic region of the scatter diagram. Furthermore, with PTO optimization for taking into account the viscous damping, it was expected that the *Bullet* could increase its *Efficiency* more than the *Cone*.

Chapter 4

Modeling Improvement

4.1 Inclusion of Viscous Forces - Final Model 1

Final Model 1 will be developed so as to include viscous (drag) force more accurately in the Time Domain model. Methodology and results are presented.

4.1.1 Methodology

The determination of the *Keulegan-Carpenter* (KC) and the *Reynolds* (Re) numbers for the *Forced Oscillation Tests* was presented in § 3.2.1. Next, the same dimensionless quantities have to be specified for the case of a Time Domain Model simulation, under a specific sea state. In this case, additionally to the buoy's motion, water particles oscillate as well as a result of the induced waves. The maximum velocity, V_m used in Eq. (3.17), will now be replaced by the instantaneous relative velocity, V_{rel} between the buoy's velocity, \dot{z}_b and the undisturbed water particles' velocity, w .

$$V_{rel}(t) = \dot{z}_b(t) - w(t) \quad (4.1)$$

This way for every time step of the Time Domain simulation, the KC and the Re numbers can be determined and matched to the FOT results according to:

$$KC = \frac{V_{rel}T}{D} \quad (4.2)$$

$$Re = \frac{V_{rel}D}{\nu} \quad (4.3)$$

There is some difficulty in determining the period, T for the KC number as the waves are irregular. For a fast estimation, the zero-crossing period, T_z can be used. Otherwise, the wave time series, have to be divided to individual waves and estimate a different period for every one of these waves. The water particles' vertical velocity, $w(t)$ is estimated at the center of the bottom of the buoy, in accordance with the method for calculating the drag force, F_{drag} . A definition matter should be discussed here.

With Final Model 1, the drag coefficient, C_d is adjusted at every time step. This is possible by producing drag coefficients, C_d for various *Reynolds* (Re) and *Keulegan-Carpenter* (KC) numbers. For the *Forced Oscillation Tests* (FOT)

conducted in ComFLOW3, Re and KC numbers were determined for the maximum velocity, V_m of the buoy during the oscillation. In Final Model 1 the determination of Re and KC numbers is based on the actual velocity, \dot{z}_b of the buoy and not the maximum of every oscillation. It is not possible to know the velocity of a dynamic system beforehand. Nevertheless, the application of Final Model 1 for predicting the force for a *Forced Oscillation Test* in chapter 5 proved that this approach is a good approximation (Figure 5.3).

Once the real-time determination of KC and Re have been made, a series of FOT for the final design has to be decided. It is crucial to replicate with FOT the real-time conditions produced during the Time Domain simulations. For that reason, the standard deviation of KC and Re will be estimated with Time Domain simulations, under the assumption that KC and Re follow a normal distribution. The drag coefficient, C_d is kept equal to the value determined at the design phase of shape evaluation (see § 3.2). The range for KC and Re is found by the standard deviations calculation.

4.1.2 Results

A number of *Forced Oscillation Tests* had to be conducted for the *Bullet*, so as the drag coefficient, C_d adjustment to be possible. Using the drag coefficients derived for *Shape Evaluation* a Time Domain model simulation was run for the sea state with $H_s = 3.5m$ and $T_z = 6.5s$. *Reynolds* (Re) and *Keulegan-Carpenter* (KC) numbers were calculated for every time step of the calculation. The mean value and the standard deviation (std) of KC and Re were derived and presented in Table 4.1.

Number	Mean	std
<i>KC</i>	0.26	0.19
<i>Re</i>	$1.62 \cdot 10^7$	$1.18 \cdot 10^7$

Table 4.1: Mean and standard deviation of KC and Re numbers derived by Time Domain simulation.

Based on these values, a set of FOT was formed and it is presented in Table 4.2, along with KC and Re numbers and the derived drag coefficients, C_d . Scatter diagrams of the derived drag coefficients, C_d against KC and Re numbers are presented in Figure 4.1 and 4.2.

$a_{osc}[m]$	$\omega_{osc}[rad/s]$	$KC[-]$	$Re[-]$	$C_d[-]$
0.59	1.14	0.19	$1.38 \cdot 10^7$	1.85
0.56	0.84	0.18	$9.60 \cdot 10^6$	2.18
0.99	0.97	0.31	$1.96 \cdot 10^7$	1.07
1.24	1.14	0.39	$2.91 \cdot 10^7$	0.75
1.21	0.84	0.38	$2.07 \cdot 10^7$	1.07
1.13	0.74	0.35	$1.71 \cdot 10^7$	1.20
1.64	0.97	0.51	$3.24 \cdot 10^7$	0.67
1.41	0.74	0.44	$2.14 \cdot 10^7$	0.92
3.02	0.97	0.95	$5.98 \cdot 10^7$	0.46
2.35	0.97	0.74	$4.65 \cdot 10^7$	0.59
1.68	0.97	0.53	$3.32 \cdot 10^7$	0.72
0.51	0.97	0.16	$9.94 \cdot 10^6$	2.71

Table 4.2: *Forced Oscillation Tests* conducted in ComFLOW3 for deriving drag coefficients, C_d for the *Bullet*.

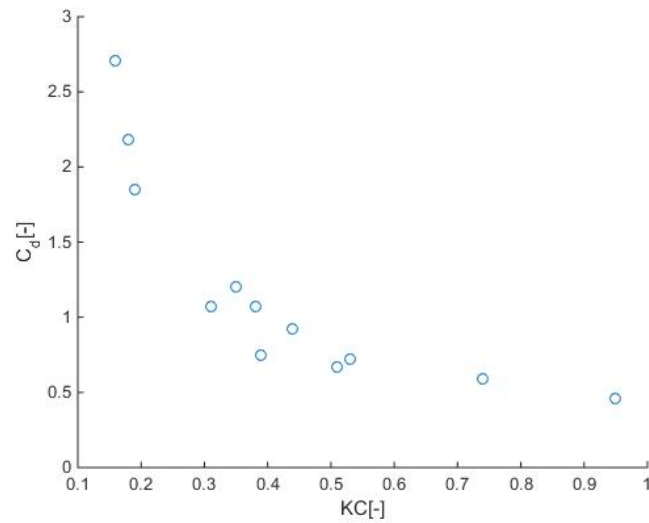


Figure 4.1: Scatter diagram of the derived drag coefficients, C_d against KC number for the conducted *Forced Oscillation Tests*.

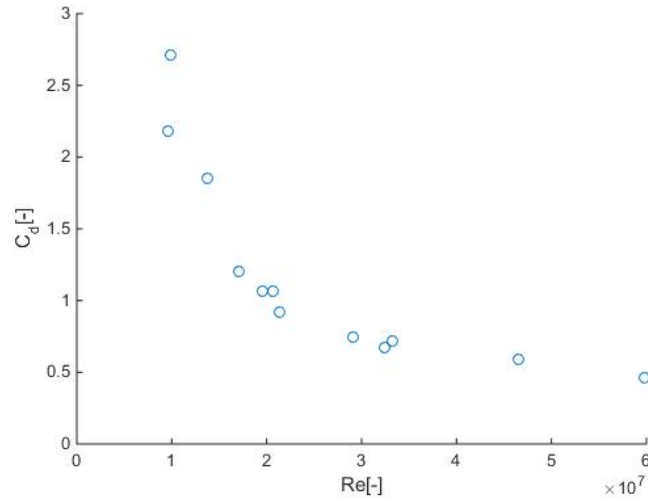


Figure 4.2: Scatter diagram of the derived drag coefficients, C_d against Re number for the conducted *Forced Oscillation Tests*.

Comments

- The drag coefficients, C_d show the same dependency both on KC and Re. For increasing KC and Re, the drag coefficients decrease exponentially.
- As *Reynolds* number is easier to be defined for every time step, without calculating the actual period, T of the wave, it is decided to interpolate the drag coefficients, C_d with this dimensionless quantity for Final Model 1.

Average Power Extraction, \bar{P} per Sea State [kW]

4.5	3.3	67.2	252.7	523.0	582.3	589.7	589.4	582.9
3.5	2.3	40.7	156.3	318.6	352.7	358.5	358.7	354.6
2.5	1.3	21.2	79.6	163.7	182.0	185.2	184.9	182.2
1.5	0.6	8.4	29.7	60.5	67.5	67.8	67.3	66.2
0.5	0.1	1.1	3.9	7.5	7.7	7.7	7.6	7.4
$H_s [m]$ / $T_z [s]$	3.5	4.5	5.5	6.5	7.5	8.5	9.5	10.5

Table 4.3: Average extracted power, \bar{P} per sea state for the *Bullet* as derived by Final Model 1 [kW].

Efficiency per Sea State [-]

4.5	0.004	0.06	0.18	0.31	0.29	0.26	0.24	0.21
3.5	0.005	0.06	0.19	0.31	0.29	0.26	0.24	0.22
2.5	0.005	0.06	0.19	0.31	0.29	0.26	0.24	0.22
1.5	0.006	0.07	0.19	0.32	0.30	0.27	0.24	0.22
0.5	0.008	0.09	0.23	0.35	0.31	0.27	0.24	0.22
$H_s [m]$ / $T_z [s]$	3.5	4.5	5.5	6.5	7.5	8.5	9.5	10.5

Table 4.4: *Efficiency* per sea state for the *Bullet* as derived by Final Model 1.

Comments

- *Efficiency* results, as derived by Final Model 1, are more uniform for sea states with the same T_z comparing to the results derived by the Time Domain model with steady drag coefficients, C_d .
- As a result of the nonlinear drag force, F_{drag} , the *Efficiency* decreases with increasing significant wave height, H_s .

Total Average Power Extraction, \bar{P} [kW] and *Efficiency*, $Eff[-]$

Design	\bar{P} [kW]	$Eff[-]$
<i>Bullet</i>	104.3	0.26

Table 4.5: Total average power extraction, \bar{P} and *Efficiency*, Eff for the *Bullet* as derived by Final Model 1.

Comments

- Final Model 1 provided comparable total average *Efficiency* to the estimation of the Time Domain model with steady drag coefficients, C_d . The difference was only 0.01 with Final Model 1 predicting smaller *Efficiency*.

PTO Damping Coefficient Optimization

Finally, with the damping produced by drag forces estimated with higher accuracy, attention is drawn to the PTO damping coefficient, β . It is expected that by increasing PTO damping coefficient calculated for the Frequency Domain model, the *Efficiency* will also increase as the extra damping will be taken into consideration. For the *Bullet*, the largest *Efficiency* losses are found for sea states with T_z equal to 4.5, 5.5s and 6.5s. After running the Final Model 1 some times and by trial and error new values are derived for the optimum PTO damping coefficient of these sea states. Comparative results are provided in Table 4.6.

Model	$\beta[\text{tonnes/s}]$ $T_z = 4.5s$	$\beta[\text{tonnes/s}]$ $T_z = 5.5s$	$\beta[\text{tonnes/s}]$ $T_z = 6.5s$	$\bar{P}[kW]$	$Eff[-]$
Frequency Domain	156	292	672	125.9	0.31
Final Model 1 (Old β)	156	292	672	104.3	0.26
Final Model 1 (New β)	624	730	874	109.8	0.27

Table 4.6: Total average power extraction, \bar{P} and *Efficiency*, Eff estimations for different values of the PTO damping coefficient using the Frequency Domain model and Final Model 1.

Comments

- For sea states with $T_z = 4.5s$ and $T_z = 5.5s$ the *Bullet* is at *resonance*. The significance of the damping induced by drag force, F_{drag} can be seen in the large increase of the PTO damping coefficient, β for these sea states.
- For sea states with $T_z = 6.5s$, by increasing the PTO damping coefficient, β it was possible to derive an increase of *Efficiency* equal only to 0.02 although the largest losses were derived for these sea states. It can be argued that PTO optimization is more important for sea states where *resonance* is achieved.
- The same optimized PTO damping coefficient, β was applied equally to sea states with the same T_z but different H_s . This is not accurate, as the drag force, F_{drag} induced damping has already been found to increase with the significant wave height, H_s .
- A more thorough investigation for the optimization of the PTO damping coefficient is needed in the presence of drag force induced damping. Nevertheless, by selectively optimizing the PTO damping coefficient by trial and error, it was possible to increase the total average *Efficiency* for more than 0.01 and the total average power extraction for $6kW$. A more extensive and detailed research can increase the *Efficiency* even more.
- The drag force, F_{drag} induced damping reduced *Efficiency* around 0.04 and the total average power extraction, \bar{P} around $16kW$ with the partial PTO damping coefficient optimization implemented, comparing to the prediction of the Frequency Domain model. The differences by retaining the PTO damping coefficient, β the same as calculated for the Frequency Domain model are even larger. This fact signifies the inclusion of drag force, F_{drag} induced damping in the assessment of the various control strategies applied for *Point Absorber* operation.

4.2 Inclusion of varying position of the buoy for wave force estimation - Final Model 2

Final Model 2 is developed so as to assess the influence of the varying position of the buoy to the excitation force determination. Methodology and results are presented.

4.2.1 Methodology

In literature, the excitation force, F_{exc} included in the Frequency Domain and the Time Domain models is usually calculated using a BEM code such as NEMOH. NEMOH, for every discrete frequency of the frequency grid, returns an amplitude and a phase shift between the surface elevation and the excitation force. For a single frequency, the time dependent excitation force can be written as:

$$F_{exc}(t) = F_{exc,a}(\omega) \cos(-\omega t + \epsilon_F \zeta) \quad (4.4)$$

No space dependency exists in Eq. (4.4) although the buoy has finite 3D dimensions. This happens because the excitation force amplitude, $F_{exc,a}(\omega)$, derived by NEMOH, is integrated for all the panels, to which the buoy has been divided (see Figure 2.9). This approach can be valid only if the oscillation of the buoy is assumed small and so the influence of the dynamic response of the buoy is neglected. The model now is improved by including this influence in the calculation of the excitation force. As a first step, the excitation force, F_{exc} is analyzed to its components.

According to *3D Diffraction Theory* (chapter 7 of Journée and Massie (2001)), F_{exc} results from the superposition of two components. The so-called *Froude-Krylov Force* and the so-called *Diffraction Force*. The *Froude-Krylov Force* results from the pressure field of the undisturbed wave as this is calculated by Eq. (2.7). From NEMOH the coordinates of the center of every panel are known and so is the area of the panels. In a Time Domain simulation, at every time step the coordinates of the centers of the panels have to be updated and a new pressure, p is calculated for every panel. Integration results to the total *Froude-Krylov Force* at every time step. Next, attention is drawn to the estimation of the *Diffraction Force*.

Time step calculation of the *Diffraction Force* is quite cumbersome. The reason is that the complexity of the mathematical relations, estimating the *Diffraction Force* with *3D Diffraction Theory*, it makes it impossible to include these relations in a Time Domain simulation. The simulation time needed would be enormous. For that reason another approach is adopted in this report. A NEMOH simulation is run for the studied buoy at eleven different positions, with the body deviating from equilibrium position. The time needed for these simulations is no more than two hours. Then, the same way the time-dependent excitation force, $F_{exc}(t)$ was calculated in Eq. (4.4), the *Diffraction Force* is calculated. NEMOH provides both the amplitudes and the phase shifts for every frequency component of the *Diffraction force*. Finally, for every different position of the buoy, the time-dependent *Diffraction Force* is found by interpolation between the simulated positions.

4.2.2 Results

Final Model 2 is built as described in § 4.2.1. Now, Final Model 1 is expanded so as to take into account the actual position of the buoy for the calculation of the excitation force, F_{exc} . The setup of Final Model 2 is kept the same as Final Model 1 without changing the PTO damping coefficient. The simulation time for only a sea state with a time step of $0.1s$ lasted almost seven hours. For this reason only one sea state was simulated so as to derive the differences to Final

Model 1. The sea state with $H_s = 3.5m$ and $T_z = 6.5s$ was used. Comparative results are presented below.

Model	$\bar{P}[kW]$	$Eff[-]$
Final Model 1	318.6	0.31
Final Model 2	327.2	0.31

Table 4.7: Comparison of the average power extraction, \bar{P} and *Efficiency*, Eff for sea state with $H_s = 3.5m$ and $T_z = 6.5s$ as derived by Final Model 1 and Final Model 2.

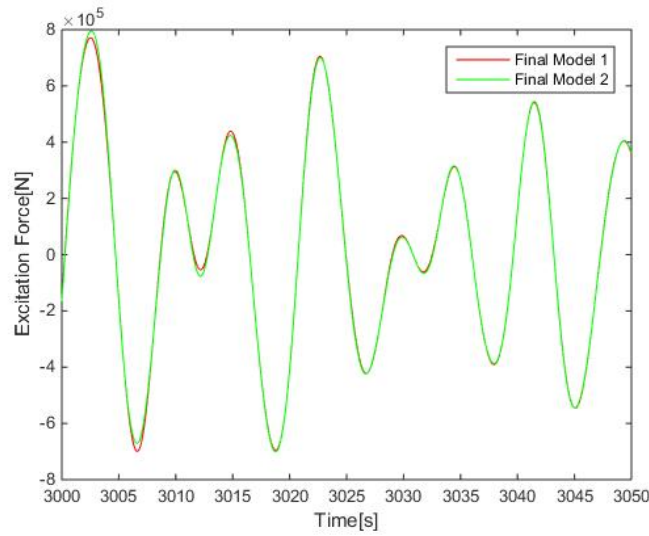


Figure 4.3: Excitation force, F_{exc} comparison between Final Model 1 and Final Model 2.

Comments

- Final Model 1 underestimated the average power extraction \bar{P} by $9kW$ comparing to Final Model 2. Considering that the average available power, \bar{P}_{avail} for the simulated sea state is equal to $1032kW$ the estimated difference in *Efficiency* is less than 0.01.
- Final Model 2 proved to be computationally expensive without deriving significant differences in *Efficiency* of power extraction comparing to Final Model 1.
- The force estimation was found to be almost identical between Final Model 1 and Final Model 2. It appears that the estimation of the excitation force, F_{exc} at equilibrium position is a rather accurate and computationally cheap method, at least for large buoys as the *Bullet*. For smaller buoys where the inertia forces are not so large and the amplitudes of oscillation are larger, more significant differences might be derived.

4.3 Summary

The methodology and results for *Modeling Improvement* were presented. At first the inclusion of viscous forces in the model with a time-step adjustment of the drag coefficient, C_d was implemented. A set of *Forced Oscillation Tests* were conducted for deriving drag coefficients, C_d for the *Bullet*. Dimensionless quantities, *Reynolds* and *Keulegan-Carpenter* numbers were employed for parameterizing the drag coefficient under various flow conditions around the buoy. The assumption to adjust the drag coefficient in Final Model 1 based on the actual and not the maximum velocity of the oscillation in irregular waves was made. The *Bullet* was found to produce an average *Efficiency* of 0.26 reduced by 0.05 comparing to the prediction of the non-viscous Frequency Domain model. After selective PTO damping coefficient optimization, it was managed to increase the predicted *Efficiency* by more than 0.01 and the predicted average power extraction by more than $6kW$. Next, Final Model 2 was built for assessing the influence of the varying position of the buoy to the excitation force estimation. The model was adjusted so as to calculate the separately the *Froude-Krylov* and the *Diffraction* force in a time step manner. Final Model 2 proved to be very expensive in computational effort without providing significant additional information to the final power prediction.

Chapter 5

Model Validation

It is important to provide validation of the models used for deriving the results presented in the previous chapters. Validation will be implemented in two steps. First, the Time Domain model without including drag force, F_{drag} will be compared to the Frequency Domain model. These are supposed to be identical in the absence of F_{drag} . Next, Final Model 1 will be validated. Two test cases will be built in ComFLOW3 and the model's force prediction will be compared to the force outcome of ComFLOW3.

5.1 Time Domain Model vs Frequency Domain Model

The two models will be compared by their prediction of the buoy's position. For the Time Domain model the buoy's position is part of the numerical solution. For the Frequency Domain model, the buoy's position for a specific time period has to be calculated based on the frequency characteristics derived in § 2.5.2. The *Response Amplitude Operator* (RAO) (Eq.2.29) and the phase shift between the incoming wave and the buoy's response (Eq.2.32) are used. The time-dependent buoy's vertical position, as calculated by the Frequency Domain model is given by:

$$z_b(t) = \sum_{n=1}^N RAO(\omega_n) \cdot \zeta_a(\omega_n) \cdot \cos(\omega_n t + \epsilon_n + \epsilon_{z\zeta}) \quad (5.1)$$

Three choices had to be made. The frequency range was decided to be equal to $0.1 - 4rad/s$ so as to be as large as possible. The frequency interval, $\Delta\omega$ was set to an initial value of $0.01rad/s$. Finally, the time step for the numerical solution of the Time Domain model which was set to an initial value of $0.1s$. In Figure 5.1, the comparison of the predicted buoy's position by the two models is presented.

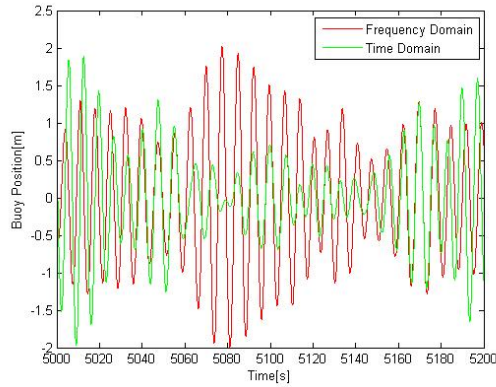


Figure 5.1: Comparison between the buoy's position calculated by the Frequency Domain model and the Time Domain model with a frequency interval of 0.01rad/s and a time step of 0.1s .

As it can be noticed the agreement between these two calculations is quite bad although both the models predicted almost the same power extraction. The first idea to tackle this problem was the decrease of the time step to 0.01s . No improvement was derived. Next, attention was drawn to the frequency interval, $\Delta\omega$. It was expected that especially for the *Impulse Response Function* (IRF) the decrease of the frequency interval would produce higher accuracy. A frequency interval of 0.001rad/s was chosen. The comparative results are shown in Figure 5.2. A perfect match between the two solutions is achieved. The important conclusion is that for shifting from the Frequency Domain to the Time Domain a high frequency resolution is needed, especially for the estimation of the IRF. Furthermore, it is found that a time step of 0.1s provides sufficient accuracy. The fourth order accurate scheme of Runge-Kutta allows for larger time step. This is quite important because the frequency interval dictates also the duration of the simulation time. As the irregular sea surface is constructed by the superposition of harmonic waves, the produced wave signal is supposed to repeat itself every $\frac{2\pi}{\Delta\omega}$ seconds. For a frequency interval of 0.001rad/s the minimum simulation time is equal to 6283s .

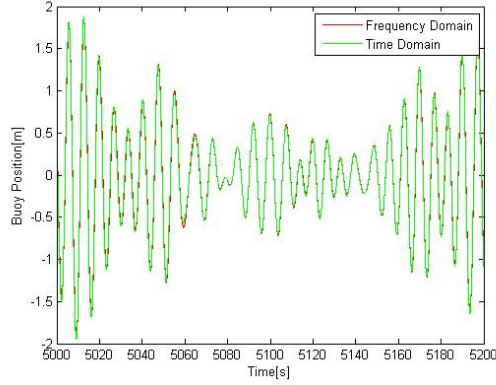


Figure 5.2: Comparison between the buoy’s position calculated by the Frequency Domain model and the Time Domain model with a frequency interval of $0.001rad/s$ and a time step of $0.1s$.

5.2 Final Model 1

Final Model 1, as presented in chapter 4, is now validated. It has already been shown that the assumption of calculating the excitation force, F_{exc} at equilibrium position is valid. Final Model 1 and Final Model 2 produce highly comparable results. For that reason Final Model 1 will be used for validation. It is reminded that in Final Model 1 a step-by-step drag coefficient, C_d adjustment was implemented. For this validation, comparison will be made between the total force calculated by the model and ComFLOW3. For the first case the buoy oscillates in otherwise still water, as in the case of the *Forced Oscillation Tests* presented in § 3.2.1. The amplitude of oscillation, a_{osc} is set to $0.59m$. The frequency of oscillation, ω_{osc} is set to $1.14rad/s$. The forces acting on the buoy are repeated here:

- Radiation force, F_{rad}
- Added mass force, F_{add}
- Drag force, F_{drag}
- Hydrostatic force, F_{hyd}

The sum of the forces reads:

$$F_{net} = F_{hyd} + F_{rad} + F_{drag} + F_{add} \quad (5.2)$$

Comparative results are presented in Figure 5.3. A rather good agreement is found between the two force calculations. It can be deduced that the calculation of the linear added mass force, F_{add} and linear radiation force, F_{rad} with values calculated by NEMOH is a good approximation at least for oscillations of this magnitude.

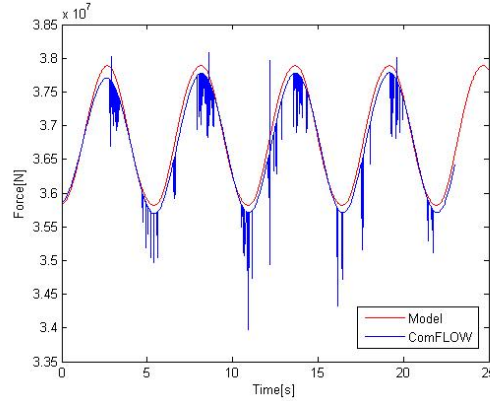


Figure 5.3: Comparison between the total force calculated by the Final Model 1 and ComFLOW3 for the case of a *Forced Oscillation Test*.

Next, another test case is considered. A forced oscillation of the buoy is again imposed. The amplitude of oscillation, a_{osc} is set to $1m$ and the frequency of oscillation, ω_{osc} is set to $0.97rad/s$. Additionally, a regular wave is imposed. The wave height, H of the wave is set to $1m$ and the frequency of the wave, ω is set to $0.97rad/s$. Complementary to the sum of forces assessed for the previous test case, an excitation force, F_{exc} is also present. The new sum of the forces reads:

$$\Sigma F = F_{hyd} + F_{exc} + F_{rad} + F_{drag} + F_{add} \quad (5.3)$$

Comparative results are presented in Figure 5.4. A relatively good agreement has been found between the two models, although not as good as in the previous case. This can be attributed mainly to two reasons. The *Linear Wave Theory* used for the calculation of the excitation force, F_{exc} in Final Model 1 is probably the main source of inaccuracy. The second can be the superposition principle used for the forces summation in the presence of waves. Nevertheless, the difference in the peak force as this is estimated by the two models is only 3%. Considering that the ComFLOW3 simulation for producing this force signal lasted six days, it can be argued that Final Model 1 has a high practical value with a quite acceptable accuracy. Finally, the analysis made is based on the assumption that the CFD code ComFLOW3 returns by definition a more physically realistic solution. It should be noted here that CFD codes are also subjected to a large variety of inaccuracies. Reflection on the numerical boundaries and numerical instabilities are the most common.

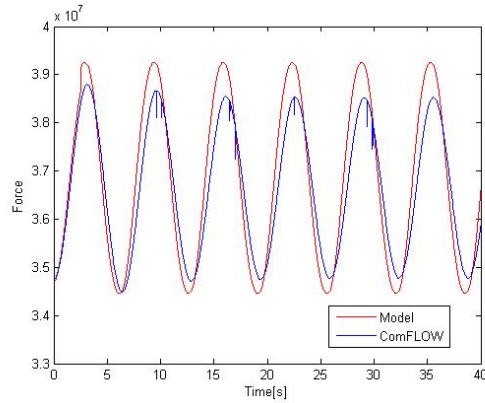


Figure 5.4: Comparison between the total force calculated by the Final Model 1 and ComFLOW3 for the case of a *Forced Oscillation Test* under wave forcing.

5.3 Summary

The solution for the position of the buoy was derived both by Frequency and Time Domain model without drag force. It was found that a rather fine frequency resolution of 0.001rad/s was needed for deriving good agreement between the two solutions. Next, Final Model 1 was used so as to estimate the total force exerted on the buoy during a *Forced Oscillation Test*. The estimation of Final Model 1 was compared to the one derived by ComFLOW3. Rather good agreement was derived. Finally, Final Model 1 was used so as to estimate the total force of an oscillating buoy in the presence of a regular wave. The estimation of Final Model 1 was again compared to the one derived by ComFLOW3. Good agreement was derived but not as good as the one derived for the case without waves. In any case the difference in the peak force was found to be less than 3% which can be considered satisfactory.

Chapter 6

Discussion

In this chapter, aspects of the adopted methodology and results are further discussed.

6.1 Methodology

An important part of this study is the determination of drag coefficients, C_d by *Forced Oscillation Tests* (FOT). The method used and presented in § 3.2.1, measured the energy transfer of waves generated by the oscillation of the buoy. Journée and Massie (2001) propose a method for deriving the radiation damping coefficient, $b(\omega)$ by similar tests. This is implemented by measuring the wave height of the radiated waves and by applying the energy relations of *Linear Wave Theory* (LWT). With radiation damping coefficient, $b(\omega)$ defined, the radiation force, F_{rad} can be calculated by Eq. (2.20). This method has a number of drawbacks. It assumes that the radiated wave is purely sinusoidal so as to make use of the energy relations of LWT. It was found that especially for the faster FOT conducted, the shape of the radiated waves deviated from sinusoidal shape. The radiated waves due to non-linearities assessed in wave propagation by ComFLOW3, had smaller troughs and higher crests. Moreover, the final radiation force is estimated by Eq. (2.20), which is also a linear approximation of the radiation force. Applying LWT for the determination of the drag coefficient, C_d discards valuable information which can be derived by ComFLOW3. The method proposed in this report used raw data derived by ComFLOW3 without applying LWT assumptions. Still, the method's accuracy is limited by two factors. The first factor is the assumption that no wave attenuation took place between the point the radiated wave was generated and the point the wave energy transfer was measured. The second factor is the fitting method used so as to derive the final drag coefficient, C_d (see § 3.2.1). In any case the method proved to be consistent through the various FOT conducted using as much as possible data of the fully viscous solution provided by ComFLOW3.

Another important implementation had to do with the estimation of the drag force, F_{drag} . The strip method, which divides the buoy in strips and then integrates over the whole length of the buoy is usually proposed in literature (Journée and Massie, 2001), (Chakrabarti, 2005). This method is mainly proposed for calculating the in-line drag force, F_{drag} , i.e. the force in the direction

of wave propagation. For the case of the *Point Absorber*, the vertical force is needed. In that case, it cannot be argued that every horizontal strip is independent on the other. The velocity field of one strip is influenced by the velocity field of neighboring strips. The method proposed in this report provides a more physical meaningful approach for calculating the drag force, F_{drag} based on the relation for the stagnation pressure (Eq. 3.22). This way, the drag coefficients, C_d calculated by FOT without water particles' motion due to waves can be used so as to satisfy the relative velocity, V_{rel} approach also for an oscillating buoy in waves without dividing the buoy in strips. Furthermore, this method is cheaper in computation time.

Finally, before continuing with the discussion about the derived results, it is important to remark a number of limitations to which all the models used in this report are subjected . These limitations can be summarized as:

- In all models, the calculation of the excitation force, F_{exc} is based on *Linear Wave Theory* (LWT). For high and/or steep waves the calculation can be rather inaccurate.
- LWT and *Diffraction Theory* is also employed for calculating the radiation coefficient, $b(\omega)$, the added mass, $a(\omega)$ and the *Impulse Response Function*, (IRF).
- The PTO device was assumed to deliver damping force to the system in a completely linear manner. In reality, this will never be the case and losses due to the PTO device will always be present. The same stands also for the spring stiffness coefficient, k_{sp} .
- The waves considered via the JONSWAP spectrum are unidirectional without spreading.

6.2 Design Optimization

Three different shapes with predetermined dimensions for the buoy of the *Point Absorber* were evaluated. For every shape the most efficient dimensions were derived (Cyl8, Bul6, Con6). There is no guarantee that the derived most efficient designs have the optimum dimensions in terms of wave power extraction. Nevertheless, valuable experience was gained by studying the results of the various designs tested.

A general goal for optimizing the dimensions of a certain shape is to derive the dimensions which maximize the average power extraction for sea states with the highest available energy through the year. Cyl9 was found to have a total average *Efficiency* equal to 0.30. Its highest *Efficiency* was derived for sea states with $T_z = 7.5s$. These sea states have less available energy than sea states with $T_z = 6.5s$. Cyl8, which proved to be the most efficient design ($Eff = 0.32$) within the Cylinder set, had its highest *Efficiency* for these sea states. With the general goal of dimensioning defined it is interesting to discuss how optimum dimensions for a certain shape can be derived.

First, the properties of wave energy extraction are discussed. An optimum configuration of a specific design for the spring stiffness coefficient, k_{sp} and the PTO damping coefficient, β is given by Eq. (2.27) (2.28). Optimum configuration of the device for a specific sea state does not mean that the design is the

optimum for wave energy extraction by this sea state. This is highlighted by the fact that the highest *Efficiency* of every design is achieved for sea states where the *resonance* condition (Eq.2.27) is not satisfied. So as to interpret this finding, the equation of instantaneous power extraction is repeated here.

$$P(t) = F_{pto}\dot{z}_b = \beta\dot{z}_b^2$$

The wave power extraction depends on the PTO damping coefficient and buoy's velocity, \dot{z}_b . The optimum PTO damping coefficient, β is calculated by Eq. (2.28). It depends partially on the radiation damping coefficient, $b(\omega)$ and partially on the achievement of *resonance*. On the other hand, the buoy's velocity, \dot{z}_b interacts with all the features of the system. It increases with *resonance*, it decreases with increasing PTO damping coefficient, β and it decreases with increasing radiation damping coefficients, $b(\omega)$. The system is highly complex, especially when the response to irregular waves is assessed. It is better to derive a more physical, rather than mathematical, explanation to the fact that for every design the highest *Efficiency* is achieved for sea states for which the optimum configuration is not satisfied at least for Eq. (2.27). Falnes (1997) described the process of optimum wave energy extraction as a phenomenon of optimum wave destructive interference between incoming and radiated waves. It is not possible to predict this optimum wave destructive interference for the case of irregular sea states and even more to calculate which design can create it. Nevertheless, this perspective gives a reasonable explanation to why for every design the highest *Efficiency* is achieved for sea states where the velocities are not enhanced by *resonance*. For the given wave energy spectrum used (JONSWAP) and its energy distribution, *resonance* and higher buoy velocities cannot coincide with optimum radiation damping.

Now that the mechanism of wave energy conversion has been interpreted, the next step of the analysis is to examine how the dimensions of the buoy can influence power extraction. For the reasons of this examination the Cylinder set of designs will be used. The two examined dimensions are the total length (draft) of the Cylinder, TD and its radius, R . Cyl2, Cyl5 and Cyl8 will be used as they have the same length ($TD = 10m$) and different radii, $R = 5m$, $R = 7.5m$ and $R = 10m$ respectively, for examining the influence of the radius, R . For examining the influence of the draft, TD of the Cylinder, Cyl4, Cyl5 and Cyl6 will be used. Comparative figures are presented.

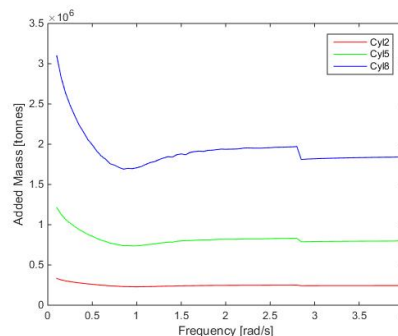


Figure 6.1: Added mass, $a(\omega)$ for Cyl2, Cyl5 and Cyl8 with their radius equal to $5m$, $7.5m$ and $10m$ respectively.

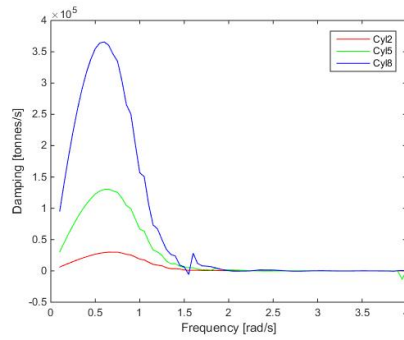


Figure 6.2: Damping, $b(\omega)$ for Cyl2, Cyl5 and Cyl8 with their radius equal to $5m$, $7.5m$ and $10m$ respectively.

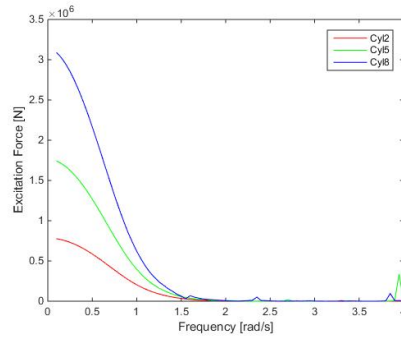


Figure 6.3: Excitation force, $F_{exc}(\omega)$ for Cyl2, Cyl5 and Cyl8 with their radius equal to $5m$, $7.5m$ and $10m$ respectively.

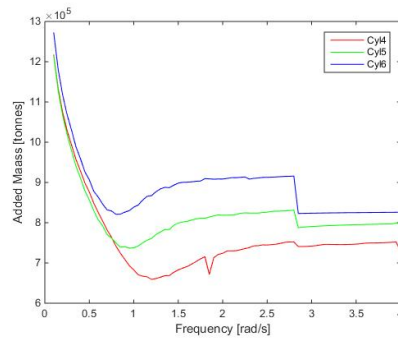


Figure 6.4: Added mass, $a(\omega)$ for Cyl4, Cyl5 and Cyl6 with their draft equal to $5m$, $10m$ and $15m$ respectively.

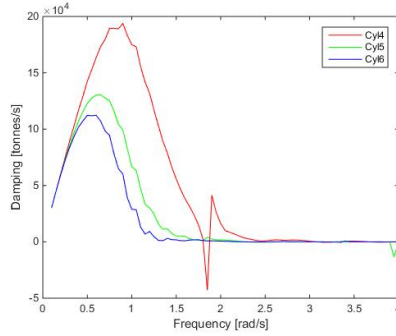


Figure 6.5: Damping, $b(\omega)$ for Cyl4, Cyl5 and Cyl6 with their radius equal to $5m$, $10m$ and $15m$ respectively.

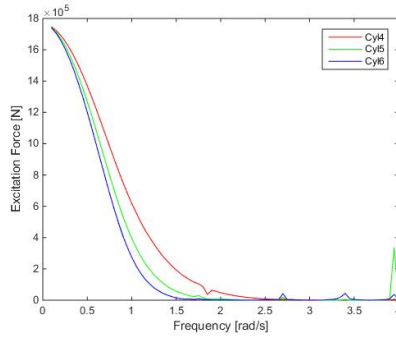


Figure 6.6: Excitation force, $F_{exc}(\omega)$ for Cyl4, Cyl5 and Cyl6 with their radius equal to $5m$, $10m$ and $15m$ respectively.

The following conclusions can be drawn:

- Added mass, $a(\omega)$ increases with radius, R . For increasing draft, TD the added mass is increased only for frequencies larger than $0.5rad/s$.
- Damping, $b(\omega)$ increases with radius, R and decreases as the buoy's draft, TD increases.
- The excitation force, $F_{exc}(\omega)$ increases with radius, R and decreases with draft, TD .

A general goal for the dimensioning of the buoy has been discussed. Locating the highest *Efficiency* at the sea states with the highest energy contribution is the most obvious and reasonable choice regardless of achieving *resonance* or not. Then the influence of radius, R and draft, TD of the buoy was analyzed in terms of the hydrodynamic coefficients, $a(\omega)$ and $b(\omega)$ and the excitation force, F_{exc} . Next step would be to derive an optimization process for the dimensions of a certain shape, different to the evaluation of a predetermined set of designs used in this study. As already shown, wave energy extraction is a complicated procedure and every change in dimensions has a multiple impact on the system's components. Based on this, it is advised to handle the dimensioning process

by optimizing one dimension at the time. As already shown, the significance of the radius, R of the buoy is high, as it determines the average available energy, \bar{P}_{avail} to the buoy. Radius, R influences both the parts which determine *Efficiency*. A steady average draft, TD can be considered and various radii can be tested. Once the most efficient radius, R is derived then several different drafts, TD of the buoy can also be tested. Mass or equivalently volume can be a guide for further optimization. Keeping the mass/volume close to the value of the most efficient design derived by radius, R and draft, TD optimization, can help deriving an even more efficient design by alternating both these dimensions. The process can be indefinite without providing any definitive design. As shown by (Wellens, 2004), a maximum *Efficiency* of 40% is difficult to be exceeded for a specific sea state. Deriving an *Efficiency* of this magnitude for the target sea states can be a stopping criterion for optimizing dimensions. Cyl8 and Bul6 achieved this *Efficiency* for the most energetic sea states ($T_z = 6.5s$).

6.3 Modeling Improvement

Final Model 1 signified the importance of the drag force, F_{drag} inclusion in the model. The most interesting finding is the large increase of the optimum PTO damping coefficient, comparing to the one calculated for Frequency Domain model, especially for sea states where the *Point Absorber* is at *resonance* with the peak frequency, ω_p . This is clearly seen in Table 4.6. It is certain that the position of the optimum PTO damping coefficient, β has shifted as a result of the extra damping induced by drag force, F_{drag} . With selective PTO optimization implemented, the loss of average power extraction comparing to the Frequency Domain model was $16kW$ and the *Efficiency* loss was equal to 0.04. A loss of power extraction of more than 10% cannot be ignored and it is reasonable to argue that drag force should be included also in the design phase of the buoy. The main problem to tackle is the parameterization of the drag coefficient, C_d applying for different designs.

Regarding the dimensions of the buoy, it is not expected that the drag coefficients are much influenced by the draft, TD of the buoy. The radius, R influences both the Re and KC numbers as these are dependent on the buoy's diameter. An analysis on how different radii influence the drag coefficients, C_d and the drag force, F_{drag} is made. Three *Forced Oscillation Tests* are set for three different Bullet designs. Three different radii are considered, i.e. $R = 5m$, $R = 7.5m$ and $R = 10m$. The length of the cylindrical part of these designs is set to $CL = 10m$, $CL = 7.5m$ and $CL = 5m$ respectively, so as all the designs to have the same draft, TD . The oscillation amplitude is set to $a_{osc} = 1.30m$ and the oscillation frequency is set to $\omega_{osc} = 0.97rad/s$. Drag coefficient results are presented in Table 6.1. The drag force produced for every design during oscillation is given in Figure 6.7.

$R[m]$	$KC[-]$	$Re[-]$	$C_d[-]$
5	0.82	$1.3 \cdot 10^{-7}$	0.61
7.5	0.54	$1.9 \cdot 10^{-7}$	0.77
10	0.41	$2.6 \cdot 10^{-7}$	0.81

Table 6.1: Drag coefficient results for Bullet designs of $R = 5m$, $R = 7.5m$ and $R = 10m$.

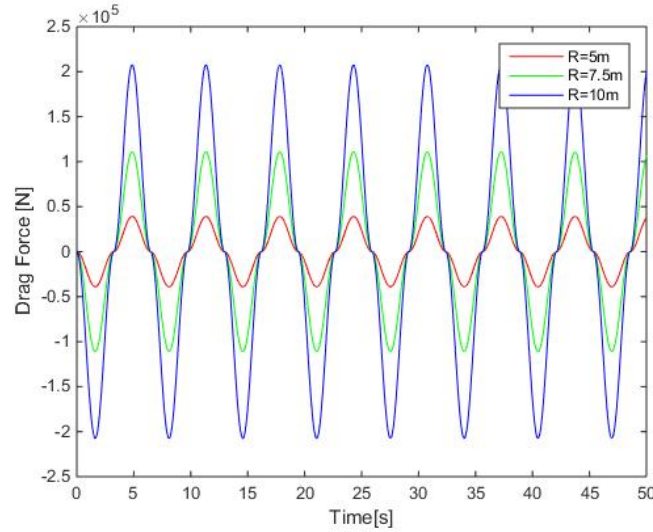


Figure 6.7: Drag force, F_{drag} produced during oscillation for Bullet designs of radius, $R = 5m$, $R = 7.5m$ and $R = 10m$.

It is noticed in Table 6.1 that the for increasing *Reynolds* numbers the drag coefficients, C_d also increase which is the opposite pattern comparing to when the FOT were conducted for the same design (Figure 4.2). On the other hand, the derived drag coefficients decrease with increasing *Keulegan-Carpenter* numbers as it also happened for the FOT presented in chapter 4. The newly derived drag coefficients are fitted into Figure 4.1. In Figure 6.8, it is observed that although two of the new derived drag coefficients, correspond to Bullet designs of different diameter, the fitting is quite good. More tests should be made for a safe conclusion but it seems that the *Keulegan-Carpenter* number can be used for the parameterization of the drag coefficients of designs with the same shape but different diameters. Assuming that a way to parameterize the drag coefficient, C_d for different designs has been derived, the dimensioning process can be supplemented with the Time Domain estimation of damping induced by drag forces at least for the target sea states.

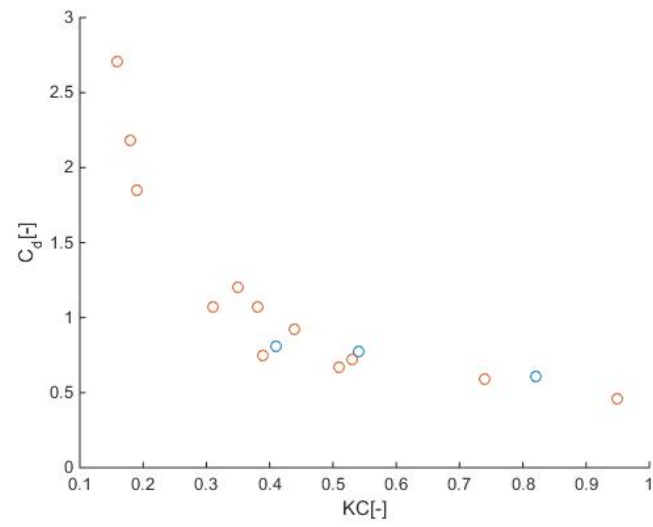


Figure 6.8: Drag coefficients plotted against *Keulegan-Carpenter* numbers. The red circles correspond to the results of the FOT conducted for the *Bullet* as presented in chapter 4. The blue circles correspond to the FOT presented in this chapter.

Chapter 7

Conclusions and Recommendations

7.1 Conclusions

The objectives of this study were presented in § 1.3. They were summarized as:

1. Derivation of an efficient design for the hull of the *Point Absorber's* buoy in terms of shape and dimensions and with respect to the studied wave climate.
2. Derivation of a simplified model for the *Point Absorber* including viscous forces and the influence of the dynamic response of the buoy to the wave force estimation.

Relative to these objectives, research questions and sub-questions were formatted and they were presented in 1.3. Answers on these questions based on the conducted study are presented.

What is the most efficient design?

Within the twenty-one different designs evaluated, Bul6 was chosen as the most efficient design. The reasons for this choice can be summarized as:

- Bul6 achieved its highest *Efficiency* for sea states with the highest energy contribution.
- Bul6 produced less drag forces, F_{drag} for fast oscillations through the water surface, comparing to Cyl8 and Con6.

It is not possible to argue that Bul6 is the most efficient design in general. As it is already discussed, the derivation of the most efficient design is a rather tedious task. Nevertheless, Bul6 achieved a total average *Efficiency* of 0.31 for the Frequency Domain model and an *Efficiency* of 0.27 after the drag force, F_{drag} was included and modeled in detail by Final Model 1. It can be argued that the predicted overall performance of Bul6 is satisfactory.

How does the shape of the buoy influence power production Efficiency?

The shape of the buoy determines its added mass, $a(\omega)$, its radiation damping coefficient, $b(\omega)$ and the excitation force, $F_{exc}(\omega)$. It is important for the dynamic response of the buoy as it influences the *resonance* properties of the buoy and its wave making capacity. The most significant influence of the shape can be argued that it is its potential in producing viscous effects. It was found that the Cylinder designs tend to produce larger drag forces, F_{drag} and reasonably should be avoided.

How do the dimensions of the buoy influence power production Efficiency?

The dimensions of the buoy influence its *resonance* properties (Eq.2.27). The radius, R and the draft, TD determine the mass of the buoy. It has been observed that there is connection between the mass or equivalently the underwater volume of the buoy and the region of the scatter diagram for which the *Point Absorber* achieves its highest *Efficiency*. Furthermore, the dimensions of the buoy also influence its radiation damping coefficient, $b(\omega)$ and the excitation force, $F_{exc}(\omega)$. Additionally, it has been shown that the drag force, F_{drag} increases with increasing radius, R . It is not possible to decouple the influence of dimensions from the influence of the shape of the buoy. For different shapes different optimum dimensions are derived.

In what way should different designs be evaluated so as the most efficient to be chosen?

Power extraction *Efficiency* is a coupled optimization problem both for the shape and the dimensions of the buoy. Moreover, the presence of size, physical or operational restrictions is a third factor to be accounted in the optimization problem. At first, the various shapes to be evaluated are chosen. Then for every different shape, the dimensions which maximize its *Efficiency* have to be derived. A procedure, as described in § 6.2 can be followed. It is important to include in the optimization process the influence of the drag force, F_{drag} by Time Domain simulations. The method for deriving drag coefficient, C_d , presented in § 3.2.1, can be used for deriving drag coefficients for the design. Furthermore, dimensionless numbers such the *Keulegan-Carpenter* and the *Reynolds* numbers can be used for applying drag coefficients to designs with different dimensions as shown in § 6.3. Finally, once the evaluated shapes are optimized in dimensions, their *Efficiency* can be compared by simulations with a model such Final Model 1.

How to improve the Point Absorber's modeling?

In order to improve modeling for *Point Absorbers*, the main goal is to describe the physical processes of the wave/buoy interaction in a physically accurate manner. An important aspect of the modeling process is the time needed by model so as to return *Efficiency* estimations. Final Model 1 was derived in order to assess the influence of the drag force, F_{drag} which is neglected by the Frequency Domain model. The simulation of a full sea state lasted less than two minutes. It can be argued that Final Model 1 increased the physical accuracy of the *Point Absorber's* modeling in a quite affordable, in computational effort, manner. On the other hand, Final Model 2 was derived so as to assess the influence of changing position of the buoy for the calculation of the excitation force,

F_{exc} . It was found that for the studied case the predicted *Efficiency* difference was less than 0.01. Final Model 2 needed around six hours so as to simulate a full sea state. It can be argued then that Final Model 2 produced small additional physical information comparing to the huge increase of the computation effort.

How viscous damping can be estimated and included in the model?

Viscous damping is produced by the influence of viscous effects to the pressure field around the buoy. It is quantified by a drag force, F_{drag} acting opposite to the buoy's velocity, \dot{z}_b . A method for calculating this drag force was presented in § 3.2.1. The method is based on the definition of stagnation pressure, p_{st} . Drag coefficients, C_d for a range of different flow and oscillation regimes can be estimated via *Forced Oscillation Tests* conducted in a numerical computation basin with the aid of a CFD code such ComFLOW3. The drag force, F_{drag} calculation was included in Final Model 1 by adjusting the drag coefficient, C_d for every time step. The validation of the model presented in chapter 5 provided satisfactory agreement between the force prediction of the model and ComFLOW3.

How wave force can be estimated more accurately and included in the model?

With Final Model 2 the influence of changing position of the buoy to the calculation of the excitation force, F_{exc} was assessed. The force was split in two parts. The *Froude-Krylov* force and the *Diffraction* force as explained in 4.2.1. *Linear Wave Theory* and *3D-Diffraction Theory* were used again but in a time step assessment. It was found that the difference to the excitation force, F_{exc} assessment between Final Model 1 and Final Model 2 was not significant while the time needed for simulations with Final Model 2 was rather large. It can be concluded that the assumption of calculating the excitation force, F_{exc} at equilibrium position is a rather accurate assumption at least for large buoys as the ones studied in this report. Finally, it should be noted that with also the position influence of the buoy assessed, *Linear Wave Theory* cannot provide any more physical accuracy in the calculation of the excitation force, F_{exc} . It might be important to assess the behavior of the excitation force, F_{exc} via fully viscous and nonlinear simulations as the ones produced by ConFLOW3.

What is the significance of the additions implemented to the linear model and how do they influence power production?

As already discussed, the two additions implemented in this study were the inclusion of drag force, F_{drag} and the time step evaluation of the excitation force, F_{exc} . The latter proved to have minor influence in the *Efficiency* prediction for the *Point Absorber*. On the other hand, the influence of the drag force, F_{drag} was found to be quite important. The viscous damping produced by F_{drag} reduced the power extraction more than 10% compared to the prediction by Frequency Domain model. Additionally it was shown in chapter 4, the position of the optimum configuration of the PTO damping coefficient, β (Eq.2.28) shifts to larger values as a result of the extra damping induced to the buoy's motion. This shift was larger for sea states where the natural frequency of the buoy coincided with the peak frequency, ω_p of the sea state. It can be concluded that viscous damping is important to be assessed both for *Efficiency* predictions and

in any control strategy applied for maximizing the power extraction of the *Point Absorber*.

7.2 Recommendations

Based on the knowledge acquired during this study, a number of recommendations regarding further research for *Point Absorbers* is discussed.

Excitation Force Estimation

With Final Model 2 the varying position of the buoy was included in the estimation of the excitation force, F_{exc} . *Linear Wave Theory* and *3D-Diffraction Theory* cannot provide any more accuracy. It would be important to make a nonlinear assessment of the excitation force without the inherent assumptions of *Linear Wave Theory*. Especially for the case of irregular waves of variable steepness, the linear approximation of the excitation force may be quite inaccurate. *Computational Fluid Dynamics* codes provide the potential for conducting such experiments with low cost and in relatively short time.

Radiation and Restoring Forces

In this study, a linear approximation of the radiation force, F_{rad} and the restoring force, F_{res} was made. For large amplitude oscillations, especially during *resonance*, linear approximation can be a source of significant inaccuracy in the prediction of the dynamic response of the buoy. *System Identification Theory* and numerical experiments with a *Computational Fluid Dynamics* code can be used for developing a dynamic model mimicking the nonlinear behavior of the radiation and restoring forces. Such studies have been presented by Perez and Fossen (2009) and Taghipour et al. (2008).

PTO Device

In this study the PTO device was modeled as a linear damper. In reality, this cannot be valid and the inclusion of power losses due to the PTO device will always be present. The PTO device has to be modeled more accurately. Cargo (2012) made an extensive study for the modeling of the PTO device and his results can be used for further improvement of the *Point Absorber's* modeling. Furthermore, in this study, no restrictions regarding the size and subsequently the delivered force by the PTO device were applied. This approach can lead to an uneconomic design for the *Point Absorber*. Dimensioning of the buoy should be made in combination to a PTO device size which can maximize the economic benefit of power extraction.

Multiple Point Absorbers

A way to sustain *Point Absorber*-wave energy conversion more profitable is to create at selected locations farms of closely spaced *Point Absorbers*. In this case, modeling should be extended so as to include the hydrodynamic interaction of the *Point Absorbers* operating closely. Furthermore, it would be important to include the directional spreading of waves which was neglected in this study.

Chapter 8

Bibliography

- J.D. Anderson. Computational Fluid Dynamics: The Basics with Applications, 1995.
- Gd. Backer. Hydrodynamic design optimization of wave energy converters consisting of heaving point absorbers. *Ghent University, Belgium*, 2009. URL <http://www.vliz.be/imisdocs/publications/220173.pdf>.
- M. Bhinder, A. Babarit, L. Gentaz, and P. Ferrant. Assessment of Viscous Damping via 3D-CFD Modelling of a Floating Wave Energy Device. *European Wave and Tidal Energy Conference, EWTEC*, pages 1–6, 2011.
- M. Blanco, M. Lafoz, and G. Navarro. Wave energy converter dimensioning constrained by location, power take-off and control strategy. *IEEE International Symposium on Industrial Electronics*, pages 1462–1467, 2012. ISSN 2163-5137. doi: 10.1109/ISIE.2012.6237307.
- C. Cargo. Design and Control of Hydraulic Power Take-Offs for Wave Energy Converters. 2012.
- S Chakrabarti. *Handbook of Offshore Engineering*. Elsevier Ocean Engineering Series. Elsevier, 2005. ISBN 9780080443812. URL <https://books.google.nl/books?id=Snbuzun9LUQC>.
- Z. Cheng, J. Yang, Z. Hu, and L. Xiao. Frequency/time domain modeling of a direct drive point absorber wave energy converter. *Science China: Physics, Mechanics and Astronomy*, 57(2):311–320, 2014. ISSN 16747348. doi: 10.1007/s11433-013-5200-8.
- H. Cozijn. Heave, Roll and Pitch Damping of a Deepwater CALM Buoy with a Skirt. *15th International Offshore and Polar Engineering Conference*, 8: 388–395, 2005. ISSN 10986189.
- W. E. Cummins. The impulse response function and ship motions, 1962.
- B. Drew, A.R. Plummer, and M.N. Sahinkaya. A review of wave energy converter technology. 223:887–902, 2009. ISSN 0957-6509. doi: 10.1243/09576509JPE782. URL <http://dx.doi.org/10.1243/09576509JPE782>.

- Ecole Centrale du Nantes. NEMOH Web Page, 2016. URL <http://lheea.ec-nantes.fr/doku.php/emo/nemoh/start>.
- EMEC Website. Wave devices : EMEC: European Marine Energy Centre. URL <http://www.emec.org.uk/marine-energy/wave-devices/>.
- J. Falnes. Principles for Capture of Energy From Ocean Waves. Phase Control and Optimum Oscillation. *Internet Web page h httpwww phys ntnu noinstdefprosjekterbolgeenergiphcontrl pdf i*, (curve c):1–8, 1997. URL http://www.waveenergy.civil.aau.dk/we_phd_course/2006/pdf/phcontrl.pdf.
- K. Hasselmann, T P Barnett, E. Bouws, H. Carlson, D. E. Cartwright, K. Enke, J A Ewing, H. Gienapp, D E Hasselmann, P. Kruseman, A Meerburg, P Muller, D. J. Olbers, K. Richter, W Sell, and H. Walden. Measurements of Wind-Wave Growth and Swell Decay during the Joint North Sea Wave Project (JONSWAP). *Ergnzungsheft zur Deutschen Hydrographischen Zeitschrift Reihe*, A(8)(8 0):p.95, 1973. doi: citeulike-article-id:2710264.
- C.W. Hirt and B.D. Nichols. Volume of fluid (VOF) method for the dynamics of free boundaries. *Journal of Computational Physics*, 39(1): 201–225, 1981. ISSN 00219991. doi: 10.1016/0021-9991(81)90145-5. URL <http://www.sciencedirect.com/science/article/pii/0021999181901455>.
- J.M.J. Journée and W .W. Massie. *Offshore hydromechanics*. Number January. 2001. doi: 10.1016/S0013-4686(01)00879-9.
- Z. Kao. A Control System for a Wave Energy Converter for Optimum Power Production. *University of Twente*, (MSc Thesis), 2014.
- P. K. Kundu, I.M. Cohen, and D. R. Dowling. *Fluid Mechanics*, volume 40. 2012. ISBN 9780123821003. doi: 10.1002/1521-3773(20010316)40:6;9823::AID-ANIE9823;3.3.CO;2-C.
- R.H. Nichols. *Turbulence models and their application to complex flows*. 2001.
- F.T. Ogilvie. *Recent Progress Towards the Understanding and Prediction of Ship*, 1964.
- Tristan Perez and Thor I Fossen. A Matlab Toolbox for Parametric Identification of Radiation-Force Models of Ships and Offshore Structures. 30(1):1–15, 2009. doi: 10.4173/mic.2009.1.1.
- SALOME. SALOME Webpage, 2016. URL <http://www.salome-platform.org/>.
- Reza Taghipour, Tristan Perez, and Torgeir Moan. Hybrid frequency – time domain models for dynamic response analysis of marine structures. 35:685–705, 2008. doi: 10.1016/j.oceaneng.2007.11.002.
- O. Thilleul. Omae2013-10818 Validation of Cfd for the Determination of Damping Coefficients. *Omae*, (2003):1–10, 2013.
- R.P. Wellens. *Wave energy: Study to determine the optimal performance of a floating wave energy converter*. PhD thesis, 2004.

R.P. Wellens. *Wave Simulation in Truncated Domains for Offshore Applications*. 2012. ISBN 9789461691965.

Wikipedia. Renewable_energy @ en.wikipedia.org, 2016a. URL https://en.wikipedia.org/wiki/Renewable_energy.

Wikipedia. Wave_power @ en.wikipedia.org, 2016b. URL https://en.wikipedia.org/wiki/Wave_power#History.

Appendix A

The term, WEC, applies to a large variety of structures of different designs, whose aim is to turn the wave energy into electrical power. In general, the function of a WEC relies on taking advantage of the pressure variations, horizontal or vertical, produced by the varying sea surface of waves. A generator connected to the WEC device turns the produced motion into electrical power. According to Drew et al. (2009), despite of the large variation of designs, WECs are usually categorized by location and type.

In terms of location, WECs are characterized as *onshore* or *offshore* devices. Onshore devices exist close or attached to shoreline and they are assumed to function under shallow water conditions while offshore devices are positioned further away from the shore and they are assumed to function under deep water conditions. The advantages of onshore type of WECs are the cheaper construction and maintenance costs, the smaller danger of damage as a result of extreme wave conditions and the proximity to the electrical network comparing to the offshore WEC. The significant disadvantage is the lower energy that waves carry close to the shore as a result of wave attenuation in the surf zone. Also the tidal range is important for onshore WECs. On the other hand, offshore devices are capable of harnessing larger amounts of wave energy but installation and maintenance are difficult and costly.

The type classification is presented according to The European Marine Energy Centre Ltd. (EMEC)(EMEC Website). Eight general types of WEC devices are identified:

1) Attenuator:

An attenuator is a floating device which operates parallel to the direction of wave propagation and effectively rides the waves. These devices capture energy from the relative motion of their arms as the wave passes by them (Fig.8.1). An example of an installed attenuator is the Pelamis Wave Energy Converter, first time connected to the UK grid in 2004.

2) Point absorber:

A point absorber is a floating structure which absorbs energy from all directions through its movements at/near the water surface. It converts the motion of the buoyant top relative to the base into electrical power. The power take-off system may take a number of forms, depending on the configuration of displacers/reactors (Fig.8.2). Examples of installed point absorber are the PowerBuoys manufactured by Ocean Power Technology in Pennington, New Jersey.

3) Oscillating wave surge converter (OWSC):

Oscillating wave surge converters extract energy from wave surges and the movement of water particles within them. The arm oscillates as a pendulum mounted on a pivoted joint in response to the movement of water in the waves (Fig.8.3). The first OWSC prototype, Oyster1 was installed by Aquamarine Power in 2009 at EMEC in Orkney, UK and delivered electric power to the grid.

4) Oscillating water column (OWC):

An oscillating water column is a partially submerged, hollow structure. It is open to the sea below the water line, enclosing a column of air on top of a column of water. Waves cause the water column to rise and fall, which in turn compresses and decompresses the air column. This trapped air is allowed to flow to and from the atmosphere via a turbine, which usually has the ability to rotate regardless of the direction of the airflow. The rotation of the turbine is used to generate electricity (Fig.8.4). LIMPET at the Isle of Islay in Scotland is an example of installed OWC device. It was installed in 2001.

5) Overtopping/terminator device:

Overtopping devices capture water as waves break into a storage reservoir. The water is then returned to the sea by passing through a conventional low-head turbine which generates power. An overtopping device may use "collectors" to concentrate the wave energy (Fig.8.5). The Wave Dragon device is an example of overtopping devices firstly installed in 2003 in Denmark.

6) Submerged pressure differential (SPD):

Submerged pressure differential devices are typically located near shore and attached to the seabed. The motion of the waves causes the sea level to rise and fall above the device, inducing a pressure differential in the device. The alternating pressure pumps fluid through a system to generate electricity (Fig.8.6). Archimedes Wave Swing is an example of an SPD device successfully tested for the first time in 2004 off the coast of Portugal.

7) Bulge wave:

Bulge wave technology consists of a rubber tube filled with water, moored to the seabed heading into the waves. The water enters through the stern and the passing wave causes pressure variations along the length of the tube, creating a 'bulge'. As the bulge travels through the tube it grows, gathering energy which can be used to drive a standard low-head turbine located at the bow, where the water then returns to the sea (Fig.8.7). The Anaconda Wave Energy device is an example of a Bulge Wave which is still in development phase.

8) Rotating mass:

Two forms of rotation are used to capture energy by the movement of the device heaving and swaying in the waves. This motion drives either an eccentric weight or a gyroscope causes precession. In both cases the movement is attached to an electric generator inside the device (Fig.8.8). An example of a rotating mass device is the Penguin by Wello tested between 2011 and 2014 at EMEC, Orkney,UK.

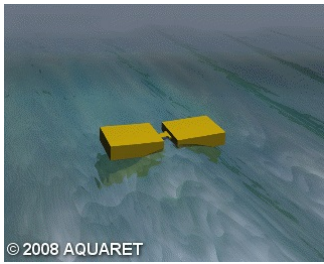


Figure 8.1: Attenuator device



Figure 8.2: Point absorber device



Figure 8.3: Oscillating wave surge device

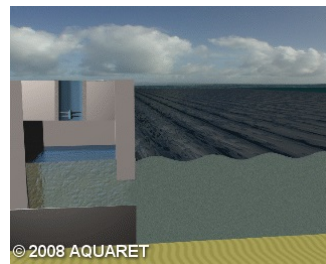


Figure 8.4: Oscillating water column device



Figure 8.5: Overtopping terminator device

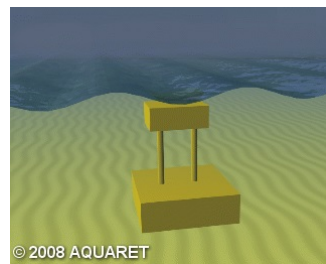


Figure 8.6: Submerged pressure differential device



Figure 8.7: Bulge wave device

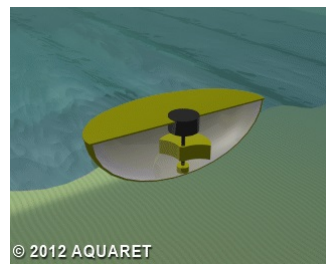


Figure 8.8: Rotating mass device

Appendix B

The setup of the *Forced Oscillation Tests* (FOT) in ComFLOW3 is presented. Specifically, the structure of the computational domain and boundary conditions are discussed.

All the buoys simulated by ComFLOW3 were axisymmetric. This fact allowed for the implementation of two symmetry planes as boundary conditions for decreasing the size of the computational domain and subsequently decreasing the total time of simulation. Specifically, an xz -symmetry plane was implemented at $y = 0$ and a yz -symmetry plane was implemented at $x = 0$. Furthermore, three different grid size layers were implemented. Close to the structure, a fine grid size was implemented for achieving increased accuracy in the interaction between water and the surface of the buoy. The size of the computational cells close to the buoy was set to $dx = dy = dz = 12.5cm$. A $\times 2$ coarsening of the grid size was implemented for the other two grid size layers leading to $dx = dy = dz = 25cm$ and $dx = dy = dz = 50cm$ respectively. An overview of the computational domain is presented in Figure 8.9.

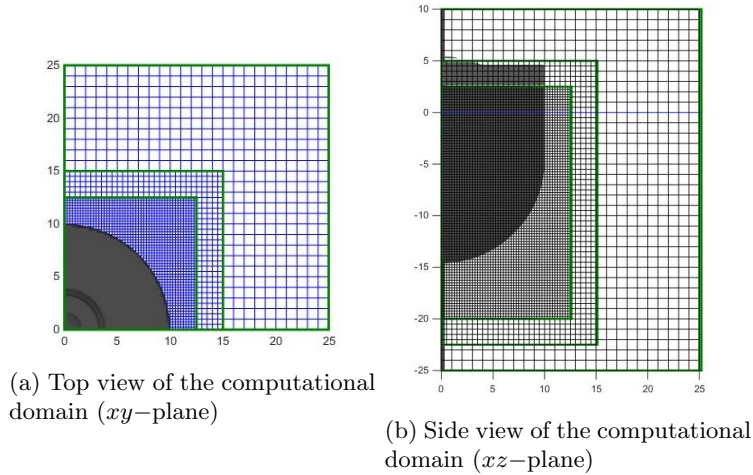


Figure 8.9: Overview of the computational domain implemented in ComFLOW3 for the *Forced oscillation Tests* conducted.

Next, the rest of the boundary conditions implemented are discussed. Two *Generating Absorbing Boundary Conditions* (GABC) had to be implemented. Dissipation of the energy of the radiated waves had to be achieved so as to

avoid reflections by the boundaries. The frequency of the radiated waves coincides with the frequency of the forced oscillation of the buoy, ω_{osc} . Optimum dissipation had to be achieved for this wave frequency. *Sommerfeld* boundary conditions were implemented for the boundaries at $x = 25m$ and $y = 25m$ according to Eq. (2.46). The wave number, k was calculated according to the dispersion relationship of *Linear Wave Theory* (Eq. 2.8). The boundary condition for the free surface was implemented so as pressure, p to equal the atmospheric pressure, p_0 . Finally, a no leak condition ($\vec{u} \cdot \vec{n} = 0$) was implemented for the bottom of the computational domain.

Appendix C

The setup of the Time Domain model is discussed. Specifically, the fourth order accurate, Runge-Kutta time discretization which is used to derive the solution to the Cummins equation is explained. The Cummins equation in the absence of drag force is repeated here.

$$(M + A)\ddot{z}_b(t) + B_{PTO}\dot{z}_b(t) + \int_0^\infty B(\tau)\dot{z}_b(t - \tau)d\tau + (C + K)z_b(t) = F_{exc}(t)$$

For notation convenience, the integro-differential term of the *Impulse Response Function* is denoted as *IRF*. For every step of the solution this term is recalculated based on the last estimation of the buoy's velocity, \dot{z}_b and the vector of buoy's velocities at previous time steps. Then, the solution vector and its first time derivative read:

$$q = \begin{bmatrix} q_1 \\ q_2 \end{bmatrix} = \begin{bmatrix} \dot{z}_b \\ z_b \end{bmatrix}, \quad q_t = \begin{bmatrix} \dot{z}_b \\ z_b \end{bmatrix}_t = \begin{bmatrix} \ddot{z}_b \\ \dot{z}_b \end{bmatrix} \quad (8.1)$$

Solving Eq. (2.37) for the matrix components of q_t leads to:

$$\ddot{z}_b = \frac{1}{M + A}F_{exc} - \frac{1}{M + A}B_{PTO}q_1 - \frac{1}{M + A}IRF - \frac{1}{M + A}(C + K)q_2 \quad (8.2)$$

$$\dot{z}_b = q_1 \quad (8.3)$$

In operator notation the above equations read:

$$q_t = \begin{bmatrix} \ddot{z}_b \\ \dot{z}_b \end{bmatrix} = -\mathcal{L}(q, t) \quad (8.4)$$

$$\mathcal{L}(q, t) = \begin{bmatrix} -\frac{1}{M+A}F_{exc}(t) + \frac{1}{M+A}B_{PTO}q_1 + \frac{1}{M+A}IRF(t) + \frac{1}{M+A}(C + K)q_2 \\ q_1 \end{bmatrix} \quad (8.5)$$

The final time discretization Runge-Kutta scheme reads:

$$k_1 = \Delta t \mathcal{L}(q_n, t_n) \quad (8.6)$$

$$k_2 = \Delta t \mathcal{L}\left(q_n - \frac{1}{2}k_1, t_n + \frac{1}{2}\Delta t\right) \quad (8.7)$$

$$k_3 = \Delta t \mathcal{L}\left(q_n - \frac{1}{2}k_2, t_n + \frac{1}{2}\Delta t\right) \quad (8.8)$$

$$k_4 = \Delta t \mathcal{L}(q_n - k_3, t_n + \Delta t) \quad (8.9)$$

$$q_{n+1} = q_n - \frac{1}{6}(k_1 + 2k_2 + 2k_3 + k_4) \quad (8.10)$$

For the solution to be derived, the excitation force, $F_{exc}(t)$ should also be estimated at half time step locations. The same principle applies also for the drag force $F_{drag}(t)$ and of course, for the *Impulse Response Function* (IRF).

Acknowledgments

Graduation from the Water Engineering & Management department of UTwente with a MSc title is the end of a journey. A journey which started with almost no clue of what will follow but now I can say that I am grateful for every moment of it. For this journey I would like to thank my family for all the kinds of support they provided for me. My beloved friends, Nikos, Giorgos, Kostas, Themis and Lefteris for being close to me even if they are so far away. All the good friends I made here in the Netherlands, for their company and help whenever this was needed. They are too many to mention but they know who they are. All the staff of the Water Engineering department and especially the teaching staff for all the good quality of studies they provided. I would like to thank Deltares for letting me do my research with all the resources I needed. Finally, special thanks belong to my supervisor, Peter Wellens for all the support, the knowledge, the motivation and creativity he passed to me during my graduation research. I consider the cooperation with him a second degree I acquired and I will always be grateful for it.